Phase Behaviour and Crystal Nucleation in Complex Multicomponent System.

Olayinka H. Olalere

A thesis submitted for the degree of Doctor of Philosophy

Supervisors: Prof. Joop H Ter Horst and Prof. Jan Sefcik

December 2019

This thesis is the result of the author's original research. It has been composed by the author and has not been previously submitted for examination which has led to the award of a degree.

Signed:

Date:

Abstract

The continuing research and use of co-crystallisation for separation, purification and modification of pharmaceutical materials in multiple industrial sectors can be attributed to the potential for high control of product quality attributes. Nucleation is a key phenomenon in crystallisation that can control product purity, morphology and crystal size distribution. Despite the use of co-crystallisation in manner mentioned above, not a lot is known about nucleation kinetics in multicomponent systems.

This thesis aims to identify gaps in knowledge and presents useful tools and methods pertinent to co-crystallisation in three themes. The first part deals with co-crystallisation within the scope of identifying factors that influence co-crystal solubility phase diagram (Chapter 3) in a workflow. Co-crystal screening methods is considered with the objective to compare and contrast approaches to increase chances of forming a co-crystal and extend an already established co-crystal screening workflow (Chapter 4). The third part addresses nucleation kinetics in multicomponent systems. Once the phase diagram is elucidated the effect of solution stoichiometry on nucleation kinetics in ternary systems is then investigated (Chapter 5). In a move to increase our knowledge of heterogeneous nucleation, a new approach to determine induction time through thermal changes when transmission of light is not reliable was developed and used to measure nucleation rates of small organic molecules (Chapter 6). Therefore, scaling previous experimental limitations and opening up new opportunities for co-crystal studies.

The author is confident that the workflow developed for co-crystal phase diagram and heterogeneous nucleation method presented in this thesis would benefit future research in co-crystal nucleation from solution by informing experimental design and experimental configuration.

Chapter 1

Introduction

1.1 Introduction

Crystallisation is a vital purification technology with application in multiple industries as part of a manufacturing process. Nucleation is the first step of a crystallisation process followed by crystal growth. The former has strong link to product quality attributes such as particles size distribution and purity. In order to control the quality of crystallisation outcome, there is a drive to better understand nucleation kinetics in both single component and multicomponent systems. Multicomponent systems can be described as systems that contains several constituents that are chemically independent from each other but can interact and not a product of chemical reaction that form covalent bonds. One example of such systems is a multicomponent system capable of forming co-crystals.

The increased interest in co-crystal research is driven by the potential to enhance the physicochemical properties of an active pharmaceutical ingredient (API) that would otherwise be terminated at the early stage of a drug discovery campaign due to properties such as poor solubility or stability. The economic importance through patentability of the new solid form is also a great incentive. In addition to these reasons, the study of co-crystals is also driven by more fundamental motives that is applicable to the pharmaceutical industry such as development of fast tools for phase diagram construction that can be used for process optimisation. Development of methods with potential to study heterogeneous nucleation in solution and identification of factors that influence crystal nucleation for both single and multicomponent crystals from solution.

Understanding nucleation of single component small organic molecules from crystallising solution requires a sound experimental approach.[1][2] Gaining new insights into nucleation in a multicomponent system requires a systematic multifaceted experimental approach that is built on knowledge gained from single components systems and other preliminary works.[3] The

added complexity of a multicomponent system ensures that the influence of factors such as phase behaviour, solvent effect, stoichiometry effect, effect of templates[4] and self-association[5] must be resolved and understood to garner further insights on nucleation. In order to understand and resolve this factors, the work structure in this thesis is presented in three themes as shown in Figure 1.The first is co-crystal solubility and phase diagram construction. The second theme is co-crystal screening using different methods and the third is crystal nucleation from solution. This chapter aid the understanding of these themes by introducing the reader to basic concepts, background information, challenges fashioned in the aim and objectives and the experimental work to solve them in subsequent chapters.

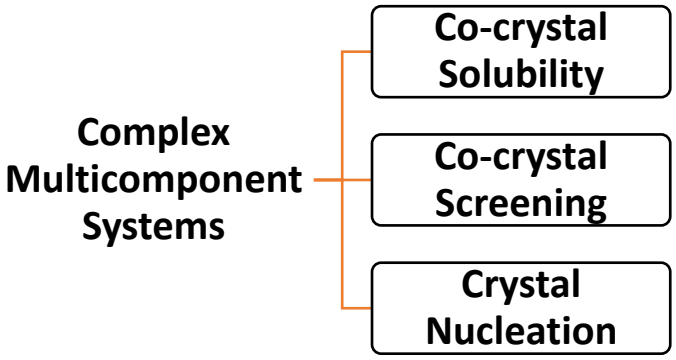

Figure 1. Overview of the three themes of interest in a multicomponent system showing co-crystal phase solubility, co-crystal screening and crystal nucleation.

1.2 Model compounds

Model compounds with pharmaceutical relevance were used for this study. A previously discovered and characterised co-crystal[6] of carbamazepine and isonicotinamide was used for co-crystal solubility and co-crystal nucleation. Two unnamed pharmaceutical API, compound A and compound B and several co-formers were used for co-crystal screening. Pilcolinamide, glycine and co-crystal of carbamazepine and isonicotinamide were used for crystal nucleation. The structure of the model compounds are shown Figure 2

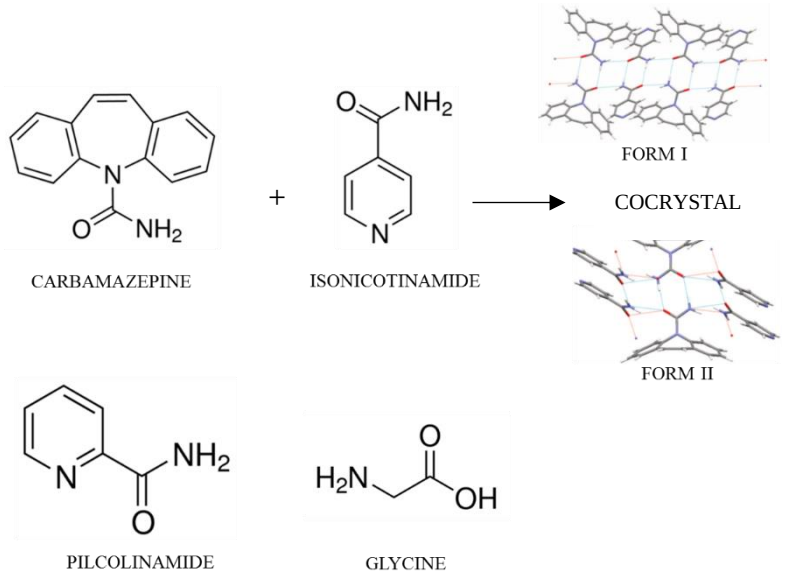

Figure 2. **Top** Structure of carbamazepine (CBZ), isonicotinamide (INA), the arrangement and interaction of both molecules forms CBZ - INA co-crystals displayed here as polymorphs (form I and form II). **Bottom** picolinamide (PIL) and glycine. All these model compounds are polymorphic in nature and are well characterised in the literature.

1.3 Co-crystallisation

The use of co-crystallisation as purification and separation technique[7][8] can be attributed to it capability to produce crystalline solid forms with enhanced physicochemical properties such as improved solubility[9] and stability.[10] There is also an economic benefit by way of patentability[11] of the new solid form. Despite these benefits, the route to co-crystal formation is not always obvious and may involve several cascades of decisions and understanding of crystal engineering. These decisions would take into account solvent selection, co-former selection and co-crystallisation techniques to use. One way to obtain a co-crystal from solution is to induce nucleation by cooling. Depending on the conditions used, the outcome may lead to control of product purity, morphology, crystal size and size distribution. The outcome of the co-crystal formation may also lead to desirable polymorphic products.[12] A polymorphic form is desirable when the polymorph improves the properties of a solid form and undesirable if the

properties of the polymorph impedes desired pharmacokinetic behaviour. One of such properties is solubility.

1.3.1 Crystalline solids

A solid is a state of matter characterised by particles arranged in a defined format such that the shape and volume are relatively stable. On a molecular level, the constituents of a solid are tightly packed and held together by intermolecular forces such as hydrogen bonds. Pharmaceutical solids can be classified into crystalline and amorphous. Amorphous solids will not be discussed because it is out of the scope of this work.

In crystalline solids, a regular structure of repeated units extends throughout the crystals. As a consequence, the solid form have a sharp melting point and thermodynamically the entropy is zero at zero kelvin. Crystalline solids can be further divided into co-crystals, salts, solvates, hydrates and polymorphs as illustrated in **Error! Reference source not found.** However the classification of these solid forms can be complicated where a co-crystal salt or co-crystal solvate can be formed as classified by Grothe et al[13] and demonstrated by Da silva et al.[14]

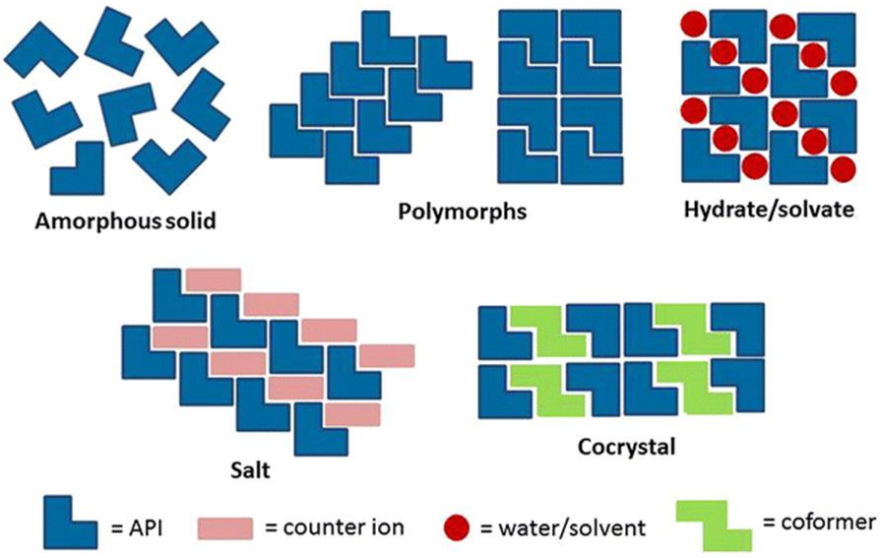

Figure 3. Common solid forms used in pharmacuetical preparations showing amorphous and different types of crystalline forms.[15] Polymorphs, solvates, hydrates , salt and co-crystals represented by 'tetris' bricks.

The definition of co-crystal is a subject of debate. [13] [16] [17] This has led to a review of seven definitions in the literature by Nate et al.[10] For the purpose of this work, co-crystal is defined as two or more neutral molecules held together by hydrogen bonds at specific stoichiometric ratio and solid at room temperature.

Co-formers are group of compounds generally regarded as safe (GRAS) and used in combination with the API to form a co-crystal at specific stoichiometric ratios. A list of pharmaceutical relevant co-crystals that comprise of active pharmaceutical ingredients (API) and co-former in a 1:1 stoichiometry ratio was published in 2010.[18] Which includes the co-crystals of carbamazepine and isonicotinamide, theophylline and methyl gallate. However co-crystal stoichiometry ratios are not restricted to 1:1 stoichiometry. For example, the co-crystal of carbamazepine and 4-aminobenzoic acid exists in: 1:1, 2:1 and 4:1 stoichiometry[19] Co-crystals formation is not restricted to API-co-former combination either. Co-crystal can be formed between two APIs. The 1:1 co-crystal of tramadol hydrochloride with celecoxib is a good example of API-API co-crystal used as an analgesic.[20]

Polymorphism is an important phenomenon that occurs in crystalline solids. The ability of a chemically identical crystalline material to exist in more than one crystalline form(s) with different arrangements or conformations of the constituents in the crystal lattice is regarded as polymorphism. Polymorphism can have a great impact on the physicochemical properties of a material particularly solubility and melting point. This can occur in single molecules like carbamazepine[21] (CBZ), Isonicotinamide[22] (INA), glycine[23] and picolinamide[24] (PIL). Polymorphism can also occur in co-crystals. For example, urea and barbituric acid.[25] More examples of compounds that exhibit polymorphism can be found in the work of Aitipamula et al.[26]

One co-crystal of interest is the co-crystal of CBZ-INA. This co-crystal is known to convert to the stable form in ethanol solvent through solvent mediated transformation.[12] The

interconversion of pharmaceutical polymorphic product is not always desirable and may cause serious delay in drug development, medicinal product scarcity. In 1998 the supply of Ritonavir was threatened as a result of product recall due to interconversion of the most soluble form to the least soluble form of the antiretroviral drug. The interconversion was induced by the presence of a degradation product which led to product recall and delay in production in order to solve the stability problems.[27]

1.3.2 Co-crystal formation rational approach

Formation of co-crystal is not always obvious and sometimes it is serendipitous.[28] In an attempt to rationalise the formation of co-crystal, supramolecular synthons concepts is used. This concept combines molecular recognition with crystal packing. Supramolecular synthons are spatial arrangements of intermolecular interactions which occur frequently in crystal structures. Homosynthon is described when the interactions between molecules in the crystal structure are the same and heterosynthon when the molecule responsible for the interactions differs. This is illustrated between the interactions of piracetam and levetiracetam in Figure 4. Where amide-amide interactions forms a homosynthon and amide-carboxylic acid forms a heterosynthon. The most useful synthons are those that forms frequently between different functional groups and some can be found in a search of the Cambridge database. The advantage here is that this approach ensures both kinetically favored co-crystal (through crystallisation) and thermodynamically favoured co-crystal to be formed thereby increasing the chances of co-crystal formation. Other rational approach such as virtual screening,[29] and isostructurality[30] are used to maximise probability of co-crystal formation.

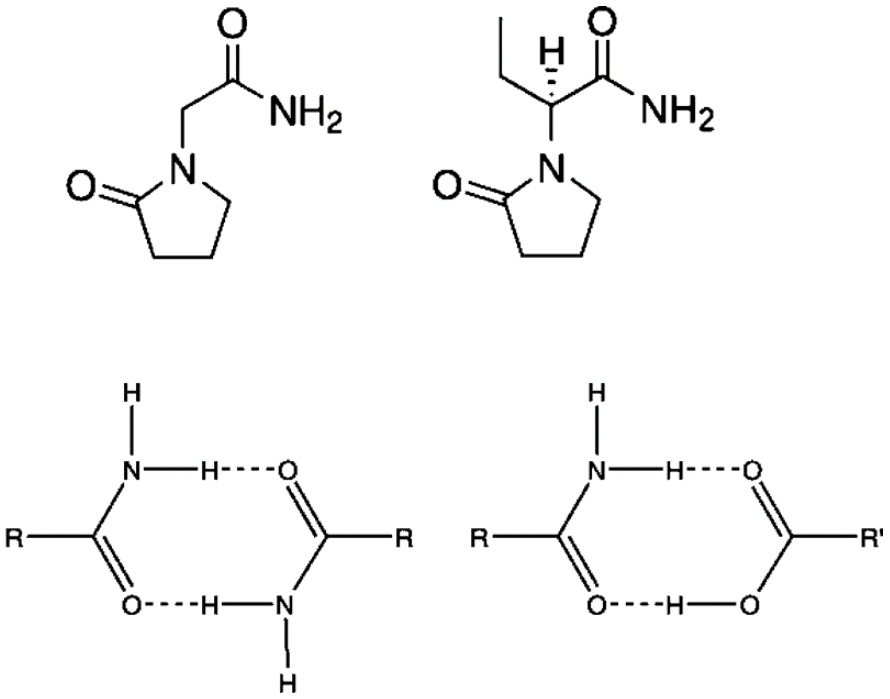

Figure 4. **Top** L-R. Structure of Piracetam and Levetiracetam. **Bottom.** L-R amide–amide homosynthon amide–carboxylic acid heterosynthon.

1.4 Methods for co-crystal screening

Any method that can be used to obtain a co-crystal has the potential to be used for co-crystal screening. However, not all methods are suitable for co-crystal screening because of factors such as amount of material required, stability of the material, desired goal of the screening and scalability of the process. For example, evaporative methods is typically used for generating single crystal for crystallography analysis and crystal structure determination while solution cooling methods may generate small crystal size that is unsuitable for determining crystal structure. In addition, not all methods are applicable to high throughput screening, scalability of a process, properties of the co-crystal formers and process conditions. Co-crystal screening can be categorised into two main areas. Solution based co-crystal screening and mechanochemical screening.

1.4.1 Mechanochemical screening method

Mechanochemical method is widely used and good for screening for different stoichiometric ratios[31] Mechanochemical approach can be divided into neat grinding and liquid assisted grinding (LAG). LAG is generally used for the following reasons: small amount of materials is needed especially solvent, it is faster and more efficient than slow evaporative methods, crystallinity is preserved better than in neat grinding and there is better control on polymorphic composition induced by the presence of solvents, large scope of co-crystal components can be used and knowledge of the relative solubility of the components is not required for screening. This method is disadvantaged in an event of a successfully co-crystal search where scalability for manufacturing process can be an issue. Alternatively twin screw extruder can be used to scale the manufacturing process. The problem with grinding is the possibility of amorphisation of the starting materials as a result of excessive grinding time, grinding energy and grinding ball size. Reduced chances of co-crystal or incomplete conversion of the components because no carrier solvents is used so the choice and volume of solvent is important.[32] The use of seed crystal is another factor[33]

1.4.2 Solution screening method

The presence of solvent can disrupt or encourage interactions between the solid and the solvent in a solution screening method such as slurrying and evaporative crystallisation so the choice of solvents used for screening should be considered carefully. Solution co-crystallisation is an established method frequently used relative to LAG. One of the advantages of evaporative co-crystal screening as part of solution screening, is that further characterisation such as single crystal x-ray analysis can be performed on the solid form outcome. This method of screening generally requires more preparation steps when compared to LAG but there are clear advantages for process design and optimisation when solubility based solution co-

crystallisation is used because of ease of scalability. It is also ideal for when small amount of material is available and materials have close relative solubilities.

1.5 Solubility measurement

Solubility is a thermodynamic parameter and can be defined as the amount of solute dissolved in a solvent volume at a given temperature.[34] The rate at which this amount of material dissolves is the dissolution rate. The thermodynamic equilibrium of a solute between the solid phase and liquid phase can traditionally be measured through equilibration where the suspension is allowed to slurry for 24hrs at isothermal condition. The amount of dissolved solute is determined through mass balance by comparing dissolved amount to the filtered residue. The amount of dissolved material can be further verified by evaporating the solvent off the filtrate. Alternatively, solubility of a pharmaceutical material can be determined from clear point measurements using crystal16. Clear point or saturation temperature measurements is based on changes in turbidity monitored by the transmission of light through the samples in response to changes in temperature. The percentage transmission of light through the sample changes as a result of dissolution of the suspended material.

Dissolution can be modulated by temperature or solvent addition.[35] In a solvent addition modulated clear point measurement, the clear point is the concentration where all the suspended materials dissolved and the transmission of light reaches 100% upon solvent addition. In a temperature variation clear point measurement, the clear point is the temperature where all the suspended samples dissolved and the transmission of light reaches 100% upon gradual temperature increase. The clear point can also be described as a saturation temperature. In an experiment conducted to compare temperature modulated clear point measurement, solvent addition clear point measurement and equilibration method of p-Hydroxybenzoic acid solubility in acetic acid found that the solubility determined through all these methods are

comparable and agrees with each other[35] suggesting that either of the two methods can be used in determining solubility but the ease of sample preparation and the scope of further experimental set up may serve as a decisive criteria to choose variable temperature measurement approach for clear point determination.

Accurate solubility measurement is the cornerstone for crystallisation design in solution. Efforts should be made to minimise possible errors during these measurements. One process that can influence the accuracy of clear point measurement is solvent evaporation. The Influence of evaporation can be mitigated by securing the vial lid. Conducting measurements at low temperature where the solubility range is at least 20°C below the boiling point of the chosen solvent.

It is generally a good practice to determine the best fit for experimental solubility data with thermodynamic models that best describes the solubility as a function of temperature.[36] This way the solubility of the material can be predicted at short temperature range. One commonly used model is van't Hoff model. This model assumes that the solution formed upon dissolution is ideal. This means that the interaction between the solute and solvent molecules is identical with that between the solute molecules and the solvent molecules themselves.

Other methods that has been used for solubility determination are high performance liquid chromatography (HPLC), Laser method,[37] and quantitative nuclear magnetic resonance(qNMR). Ultraviolet and Fourier transform infrared spectroscopy can be used to monitor solubility during crystallisation as part of process analytical tool (PAT).

1.6 Thermodynamics and Phase diagram

1.6.1 Gibbs free energy

The drive towards equilibrium in chemical thermodynamics of a system is described by two factors: the tendency to minimise enthalpy and the maximise entropy. These two factors are summarised in Gibbs free energy description. This section aims to highlight these two factors. The equilibrium state of a chemical system is defined by the amount of substance *n*, the pressure P the temperature T and the volume V. Pressure p is the summation of forces due to molecular collisions with the wall of the containers and temperature is the sum of kinetic motions of the molecules. These variables are related and for one mole of an ideal gas the relationship can be expressed as

$$pV = nRT \qquad 1$$

The heat capacity of a substance can be defined as the energy required to raise a temperature by one kelvin. Different substances has different heat capacity and the heat capacity is also dependent on the state of the substance. So the heat capacity of a substance is not constant but depends on the variables pressure, temperature and volume. Therefore the heat capacity for a gas at constant pressure and volume would differ and only varies slightly for condensed matter. This also mean for a condensed matter the heat capacity varies over a large range of temperature and can be used to estimate the enthalpies where no experimental data exists.

The enthalpy of a reaction is the heat absorbed or liberated when the reaction proceeds at constant pressure. On a molecular level it a measure of the bonding states that describes the intermolecular and intramolecular bonds in a gas, liquid or solid. For a solid, a change of a unit

volume of a solid by using temperature weakens the chemical bonds and the enthalpies increases with an increase in temperature. The relationship between temperature and the enthalpy is expressed by Kirchoffs law

$$\frac{d(\Delta \mathrm{H})}{dT} = C_p \qquad 2$$

Where H is the enthalpy T is the temperature and is the heat capacity C_p

Gibbs free energy G is commonly used in chemical thermodynamics due to a great importance of spontaneous reactions and equilibrium. Therefore a process that transition from one state to the other at an isothermal condition can be defined by

$$\Delta G = G_2 - G_1 = \Delta \mathrm{H} - \mathrm{T}\Delta \mathrm{S} \qquad 3$$

Where S is the entropy or randomness in the system. For a system at equilibrium $\Delta G = 0$ for a non equilibrium system at constant conditions of pressure and temperature, a spontaneous reaction would only occur if the reaction leads to a negative change in Gibbs free energy. In this case $\Delta G < 1$. G decreases as the temperature increases.

1.6.2 Gibbs Phase rule

Equilibrium may involve several condensed matter. In this case the degree of freedom for the heterogeneous equilibrium can be described by phase rule. Phase rule states that the degree of freedom F in a system equals the number of components C plus two, minus the number of phases P present at equilibrium.

$$F = C + 2 - P \qquad 4$$

Where 2 stands for the variables pressure and temperature. The number of component C is the minimum number of substance required to describe the elemental compositions of every phase present. So C = 3 for a system that can described using three components. *P* is the number of phases present at a given point within a domain in the phase diagram. For instance, Domain III in Figure 5 contains the co-crystal plus liquid so *P* = 2. The two in equation 4 stands for the variables pressure (p) and temperature (T). If both T and p are kept constant this number becomes zero. If one is kept constant this number becomes 1. If C is reduced to 1 at the point X_{API} = 12.5 in Figure 5 when two or three phases are at equilibrium, at a fixed T then F = 0.

In terms of phase rule a system is an isolated portion of the matter subject to limited range of specified variations. A component is the minimum number of chemical compounds needed to describe each phase in such a system. A phase is an internally homogenous part of the system which is physically separated from other parts of the system by the phase boundary which makes it mechanically separated from other phases. A composition is the amount of each component in a phase.

1.7 Phase diagram

A phase diagram is a graphical representation of the values of the thermodynamic variables when equilibrium is established among the phases of a system. Phase diagrams can be described by the number of components present in a system for example, Unary phase diagram for one - component system. Two component or Binary system and three components (ternary) system. Although phase diagrams may have different geometries. They all obey the same geometric rules.

The concise graphical representation of this behaviour is shown as the phase diagram. Phase diagram can be used to disseminate large information such as understanding co-crystallisation screening methods,[38] Phase behaviour is the part of thermodynamics that provides tools for the complete understanding of how a multicomponent system interact with each other at different conditions. Which can inform relative stability of solid phases in solution, nucleation kinetics and kinetic pathways,[39] determination of operation regions and compositions in a crystallisation process design.[40]

Binary and ternary phase diagrams are commonly used in co-crystal representation because they are easier to visualize. Increase in number of component molecules increases the complexity of a phase diagram. Phase diagram can be constructed through experimental methods and computational methods. The latter involves density functional theory and COSMO-RS solvation thermodynamics. The former is constructed based on solubility determinations[41][6] A three component system containing API, co-former and solvent can be represented by a ternary phase diagram at isothermal and isobaric conditions represented with a triangle or through orthogonal representation divided into at least six main domains as shown in Figure 5, As a typical ternary phase diagrams **I** and **II** divided into domains. The domains in the ternary phase diagram **I** is represented by Arabic numerals and the orthogonal phase diagram (**II)** by Roman numerals.

Domain 1 and III is the co-crystal region, 2 and V is the API domain, 3 and I is the co-former domain, 4 and IV is the domain where co-crystal and API are present, 5 and II is the domain where the co-crystal and co-former are present, 6 and VI is the domain where the co-crystal components are undersaturated. Both of the phase diagram are asymmetric. In **I** the phase diagram is skewed in respect to the API while in phase diagram **II** the phase diagram is asymmetric in respect to the co-former.

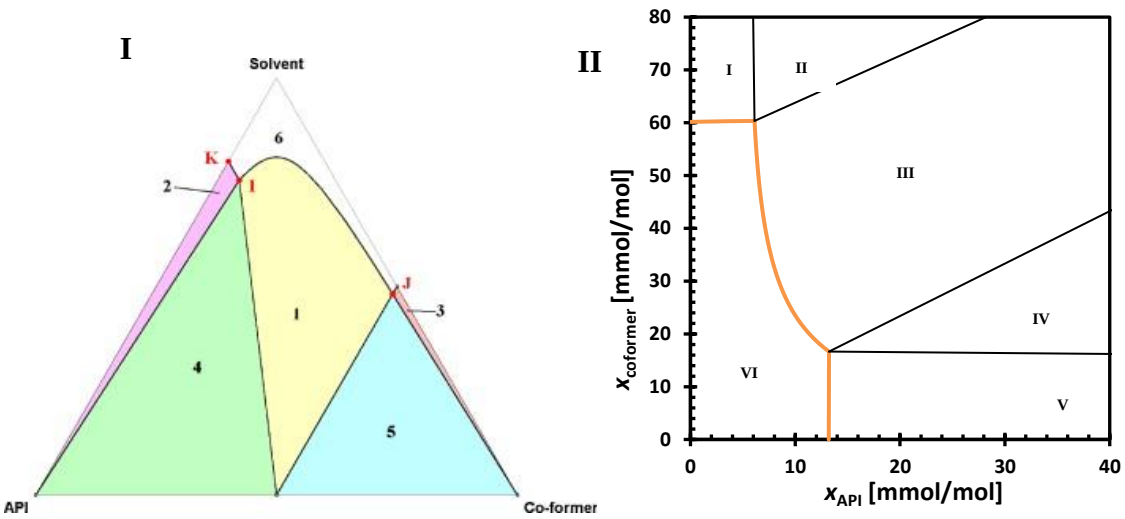

Figure 5. Shows two main representation of a phase diagram for two different co-crystal systems. The phase diagram is asymmetrical in both cases. **I** is the ternary phase diagram and **II** is the phase solubility diagram showing different phase regions. Phase diagram **I** is broken down into domain 1 pure co-crystal is present, domain 2 pure API is present, domain 3 pure coformer, domain 4 co-crystal and API mixture, domain 5 pure co-crystal and coformer and domain 6 is where the API and coformer are undersaturated. **II** is broken down into domains I pure INA is present, II mixture of pure co-former and co-crystal, III pure co-crystal , IV mixture of API and co-crystal and domain V pure API.

1.8 Challenges identified from literature review.

There is a need for developing faster methods for co-crystal phase diagram that is congruent with co-crystal screening. In most of the literature reviewed co-crystal screening is usually done using LAG method combined with other solution co-crystallisation methods such as evaporative crystallisation. Virtual screening was combined with LAG to validate virtual screening.[(42)(29)] However, no study is known that combines these methods to increase the chances of discovering a new co-crystal. These observations led to three questions.

I. Can a faster method be developed for co-crystal phase diagram construction?

II. Does combining virtual screening, LAG screening and solution method screening improve the chances of discovering a new co-crystal?

III. Can a workflow be designed that would help transition from newly discovered co-crystal and constructing the phase diagram of the co-crystal in solution.

1.9 Crystal nucleation from solution

Crystal nucleation from solution is a phase transformation in a supersaturated solution from liquid to solid. There are two types of nucleation. Primary and secondary nucleation. Secondary nucleation involves seeding a supersaturated solution with the same form of crystals expected from the solution. *Primary nucleation* is the initial formation of a crystal where there are no other crystals present. Primary nucleation can be subdivided into homogenous and heterogeneous nucleation. The spontaneous crystallisation from a supersaturated solution is described as a homogenous nucleation. Heterogeneous nucleation occurs when the presence of foreign particles in solution induces the nucleation process. These particles reduces the interfacial energy that serves as a template or attachment site for pre-nuclei clusters. For this reason, a lower supersaturation is needed for heterogeneous nucleation to occur than a homogeneous nucleation because barrier against nucleation is lowered.

1.9.1 Supersaturation

Supersaturation is the driving force of nucleation. The mode of generating supersaturation can depend on the solubility of the material. For example, the supersaturation of a material with good temperature dependent solubility can be controlled by cooling. In other instances evaporation of the solvent can be used to control the supersaturation or addition of miscible solvent where the compound is less soluble or showed no temperature dependence.

Supersaturation can also be viewed as chemical potential:

$$\Delta\mu = \mu_s - \mu_B \qquad 5$$

Where μ_s and μ_B are chemical potential of a molecule in solution and the bulk of the crystal phase respectively. A solution is supersaturated when $\Delta\mu > 0$, $\Delta\mu = 0$ saturated and $\Delta\mu < 0$ undersaturated. μ_s and μ_B can be represented by thermodynamic expression *KT ln S* so equation 5 can be rewritten

$$\Delta\mu = KTlnS \qquad 6$$

Where *K* is the Boltzmann constant, T is the absolute temperature and supersaturation ratio *S*. By simplifying equations 6 based on ionic molecules, an expression for *S* can be obtained[43] and can be further simplified for a non-ionic solution. In which supersaturation for a non-ionic solution can be rewritten as

$$S = \frac{C}{C^*} \qquad 7$$

Where *C* and C^* are actual and equilibrium concentrations. So supersaturation ratio calculations with S < 1, S = 1 and S > 1 is undersaturated, saturated and supersaturated respectively. This expression can be further developed for determination of supersaturation ratio in co-crystals based on the solubility product of the co-crystals.

1.9.2 Crystal Nucleation mechanism

The dynamics of cluster formation and cluster growth to critical size during nucleation in a supersaturation solution can be described by two mechanistic pathways.[44] One is the classical nucleation theory (CNT) and the second is the two step nucleation pathway. CNT reflects that

there is no structural difference between the crystal nuclei and mature crystal. Molecular packing of the clusters reflects all possible polymorph of the solute as a result of fluctuation in order and density.[45] In the two step nucleation mechanism the formed clusters are fluid and the crystals appear over time[46] as illustrated in Figure 6.

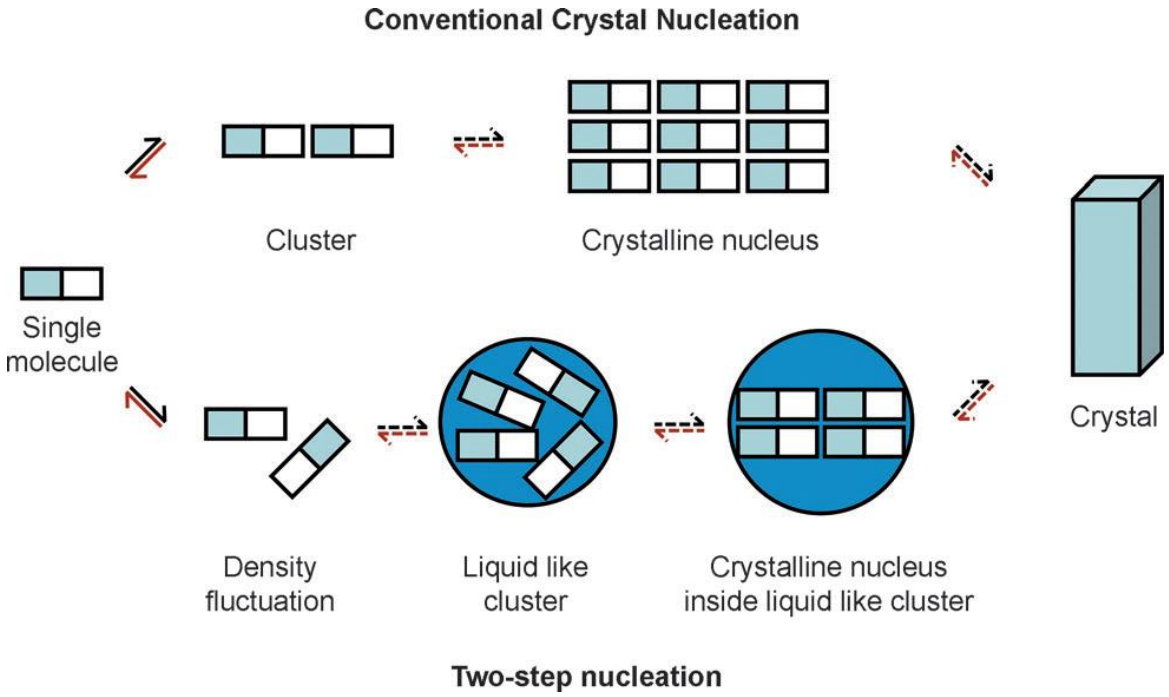

Figure 6. Crystal nucleation pathways from a supersaturated solution. **Top pathway:** Classical nucleation theory, shows how the crystalline nucleus reflects the molecular packing of the final crystal. **Bottom pathway**: represents the two-step nucleation where there is an intermediate stage with fluid like cluster before the final crystal is formed.

1.9.3 Crystal nucleation rate

According to CNT, the crystal nucleation rate *J* is the number of crystalline particles that form from a supersaturated solution per unit volume and time. Nucleation rate *J* can be expressed by equation 8. Where *J* can respond exponentially to small change in solution supersaturation *S*

$$J(S) = AS \exp\left(-\frac{B}{\ln^2 S}\right) \quad 8$$

A and *B* are pre-exponential factor and the thermodynamic factor respectively. *A* describes the molecular kinetics of the nucleation process. *B* reflects the structure of the nucleus at a molecular level. The thermodynamic parameter *B* describes the free energy barrier for the formation of a nucleus. Cluster formation via CNT pathway shown in Figure 6 is a reversible process that forms by attachment and detachment of the building units *n* to form a nucleus. The size of a nucleus in a supersaturated solution grows to reach a critical size *n** (if the nucleus formation does not fall apart) and to form crystals of detectable sizes. Equation 8 can be rewritten in full for heterogeneous nucleation to get equation 9. Where γ is the Interfacial energy between crystal and solution, the shape factor *c* relating surface area and volume, molecular volume *v* of the solid, and supersaturation ratio *S*. Z is the zeldovich factor which account for the crystal that grows or dissolve in solution and f^* is the attachment frequency of crystals to the nuclei.

$$J_{HEN} = Zf^* C_o \exp\left(-\frac{16\pi v^2 \varepsilon^3 \gamma^3}{3k^2 T^2 ln^2 S}\right) \quad 9$$

1.9.4 Thermodynamics of crystal nucleation and growth

The growth of these nucleus size can be described by Gibbs free energy. Gibbs free energy (ΔG) is a function of two opposing processes. Where ΔG_s is the surface free energy and ΔG_v is the volume free energy.

$$\Delta G = \Delta G_v + \Delta G_s \qquad 10$$

Addition of the building units to the surface of the nucleus reduces the Gibbs free energy –ve. The surface increase that results gives a + ve Gibbs free energy. Positive ΔG_s dominates at small radii which increase ΔG initially as clusters size increases ΔG goes through maximum at critical nucleus size n^* above which the total free energy decreases continuously and growth becomes favourable.

So as cluster size increases, a critical cluster size can be reached at which the gain in bulk free energy is balanced by the loss in total free interfacial energy as shown in Figure. 7. A critical nucleus in a sufficiently supersaturated solution at the nucleus-solution interface containing n^* building units would form a detectable crystal when the nucleation barrier is overcome. The presence of foreign particles influence the free energy so that nucleus are readily formed in contrast to when no foreign particles is present. So the work required for nucleation is lowered

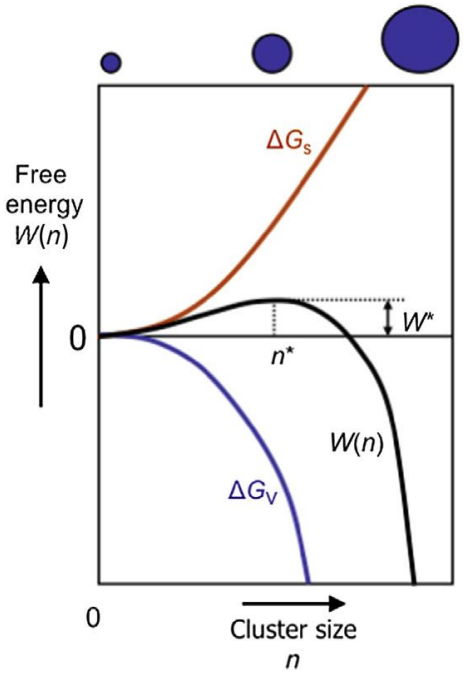

Figure. 7. Thermodynamics of CNT showing the interrelations between the cluster size and Gibbs free energy.

One of the limitations of CNT is that the predictive ability of the theory is not always accurate. Second is the assumption that nuclei clusters are made by the aggregation of monomers so there is no account for building units that exists as dimer, catermers. In a concomitant polymorphic nucleation CNT may not be adequate because it may not account for the competitive growth of polymorphic forms present. Based on these limitations, other mechanism was proposed (i) Two-step mechanism was proposed which explain that a dense liquid like clusters of solute molecules is first formed and this clusters come together to form a nuclei and then the long order structure is obtained out of solution.

1.9.5 Metastable zone

The experimental determination of a metastable zone is a measure of the kinetic stability of a supersaturated solution at which no nucleation is expected if the solution is held long enough below a critical supersaturation. When a solution containing both crystalline and solution at phase equilibrium is heated until all the crystals totally dissolves, the temperature at which this occurs is the saturation temperature T_s. If this solution is cooled to a temperature or supersaturation that is below the critical supersaturation, nucleation is not expected to occur but once cooled past the critical supersaturation, crystals are formed and detected once grown to detectable size. The difference between the saturation temperature and the temperature which crystals are detected is the metastable zone width ΔT.

$$\Delta T = T_s - T_c \qquad 11$$

The metastable zone width is an important criteria used for crystallisation design for a well-mixed systems. The metastable zone of a system is influenced by cooling rate, agitation rate, antisolvent addition rate, solution thermal history. Solution terminal history depends on the

duration and the temperature the solution is held for at temperature higher than the saturation temperature. Solution history is known to change the solution structure and effect the assembly.

1.9.6 Measurement of nucleation rate from solution

The direct determination of nucleation rate is limited by available devices or analytical instruments. Nucleation rates have been determined indirectly by monitoring changes in properties of the solutions such as turbidity and visual observations.[47].

A recent review identified 5 main methods researchers normally use for measuring the nucleation rate in solution.[49] Deterministic method, double pulse, microfluidic, droplet based[50][51][52] and stirred small volume.[53]

Table 1 highlights the pros and cons of each methods.

Table 1. Nucleation rate determination methods in the literature with the pros and cons of each methods.

Method	Advantages	Disadvantages
Deterministic	Mimics industrial set-up Time-saving Easy to scale up	Hard to operate at the desired temperature or supersaturation - Large dimensions of the setup and transport phenomenon Requires assumptions or simplification of crystallizer mixing capability Crystal agglomeration and breakage phenomenon.
Double pulse	Separates nucleation from growth	Counting crystals is labour and time-consuming Only applicable with crystals with slow growth rate[54] Prelimary work is required to determine experimental growth conditions Supersaturation range for study is limited.
Microfluidic		

	Better conformity of droplet size in contrast to droplet method. Ability to store, process, and control molecules in space and time.[55] Large nucleation rates data quantity can be obtained. Material can be saved because small volume of material is required. Used to prove the classical nucleation theory expression.	Defect in device manufacture or design can be problematic - device has to be Transparent, Temperature control can be poor chemical compatibility issues Clogging of channels.
Droplet based	Diminish the effect of heterogeneous particles Small amount of material is needed so ideal for expensive materials. Ease of dispersion and operation Good for high melting point materials.[54]	Ignores the crystal growth time Large droplet size variations
Stirred small volume	Small volume required Lab scale data is relatable to the industrial scale crystallizer by introducing stirring in the measurements.	Statistically significant amount of data is required to reduce stochasticity[56] Data analysis may require different assumptions and approach[1][57]

1.9.7 Induction time measurement

Nucleation is the process of random generation of nanoscopically small formations of the new phase that have the ability for irreversible overgrowth to macroscopic sizes.[58] This nanoscopically small formation are the nucleus. Nucleation is stochastic in nature and one way to harness this stochasticity is through induction time measurements at a known supersaturation.

Induction time *t* is defined as the time period between the moments a constant supersaturation is created t_o and crystals t_x are detected. The nucleus can not be directly detected and there is a waiting period before it grows to detectable size *tg*, the probability to detect crystals with an induction *t* which were nucleated at earlier time can be determined using equation below.

$$P(t) = 1 - \exp\left(-JV\left(t - t_g\right)\right) \qquad 12$$

The probability distribution of the induction time can be determined from a large number of induction time measurements at constant supersaturation, temperature, and volume. For M isolated experiments, the probability *P(t)* to measure an induction time between zero and time *t* is defined as

$$P(t) = \frac{M^+(t)}{M} \qquad 13$$

1.9.8 Challenges identified in literature review

Heterogeneous nucleation is a surface catalysed occurrence and can be assumed to be the main mechanism of nucleation in the pharmaceutical industry. These surfaces can be dust, impurities and any other foreign matter in the mother liquor. Crystal nucleation from solution is not fully understood.[3][44][46] One way to understand Heterogeneous nucleation is to scale down to manageable volume using a stirred fixed volume method and introduce well defined templates. One of the limitations in studying heterogeneous nucleation on the platform used for stirred small volume is that only low concentration of well-defined templates can be used so there is a need to develop an alternative method to study primary nucleation.

One main area of primary nucleation that has not be studied involves phase complexity.[59] This is interpreted as understanding nucleation in multicomponent systems where factors that influence nucleation in these systems can be identified in an effort to improve our understanding of nucleation from the classical nucleation theory perspective.

Two main questions were then developed.

(i). Is there an alternative method to measure heterogeneous nucleation in stirred small volume at high templates concentration?

(ii). What other factors can affects nucleation in multicomponent systems?

1.10 Aims and Objectives

In general a multicomponent system may contain two or more components in a system. Further addition of more components increases the level of complexity and degree of freedom. In this work, a three component system is investigated where one of the components is a solvent and the remaining two are solids capable of forming co-crystal. This thesis overall aim is to investigate crystal nucleation in multicomponent systems and demonstrate useful tools for this purpose. As a consequence the aim is divided into three main themes. The first theme focuses on co-crystal phase solubility. The second focuses on optimising co-crystal screening and the third challenge focuses on crystal nucleation. Figure 8 shows the overview of the experimental chapters.

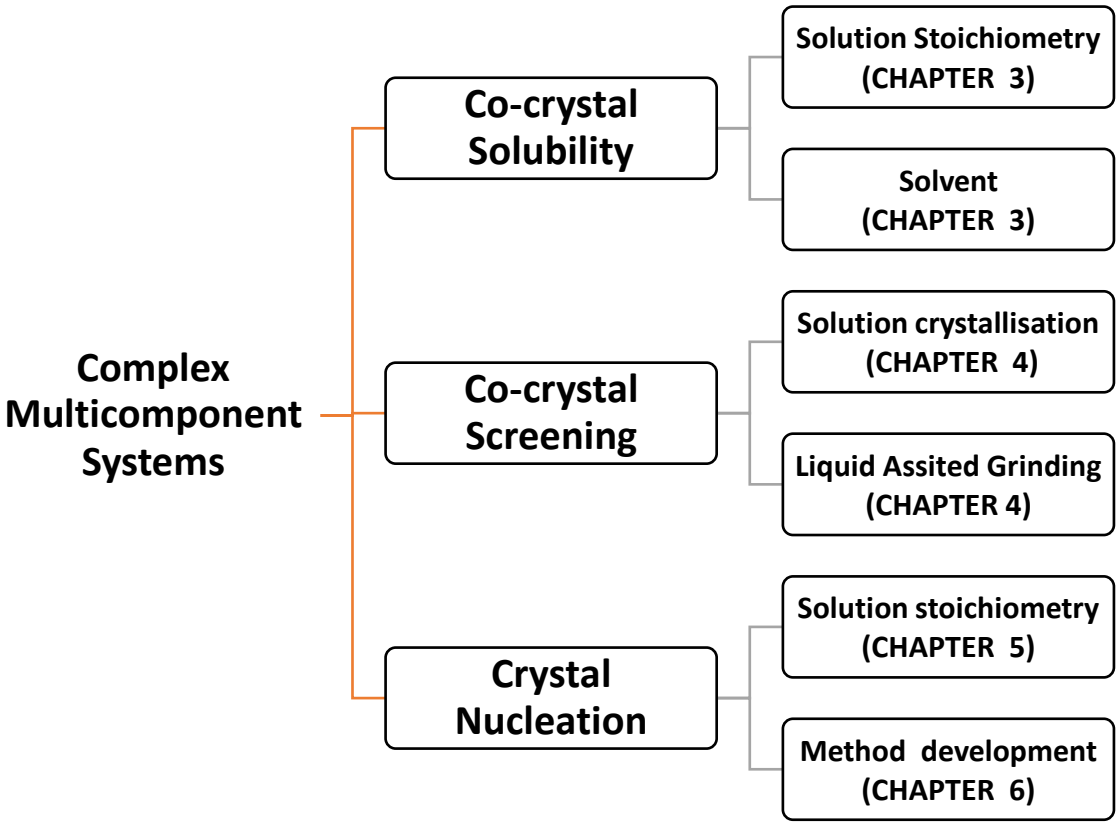

Figure 8. Overview of the experimental section of thesis showing the breakdown of the area of focus for this work. First showing the themes of this thesis and then individual aims addressed in the chapters

1.10.1 Co-crystal phase solubility

The objective of this chapter is to develop a workflow for developing a phase diagram to improve accuracy of a co-crystal phase diagram. Chapter 3 focuses on the measurement and understanding of the effect of solution stoichiometry and solvent on the co-crystal solubility. A newly developed and experimentally fast and efficient approach is described to construct the co-crystal phase diagram using the co-crystalline compound of Carbamazepine and

Isonicotinamide as an example. The schematic phase diagram allows the study of solution stoichiometry on the co-crystal solubility product. Finally, the effect of solvent on the co-crystal phase diagram is shown.

1.10.2 Co-crystal screening in practice

Chapter 4 focuses on comparing grinding and solution co-crystallisation approaches for discovering new co-crystal. The discovery of a new co-crystalline material with enhanced properties during drug development is welcomed news. There are two often used co-crystal preparation methods: Liquid Assisted Grinding (LAG) and solution crystallization. However, it is not yet known which technique is optimal for co-crystal discovery and co-crystallisation process development. The two methods for co-crystal screening and co-crystallisation process development were compared. First, the use of an in silico approach is described that uses the propensity to form hydrogen bonds as a tool to select co-formers. Then, in parallel, the co-formers are tested on their ability to form co-crystals with an API using both LAG and solution crystallisation. The two methods are compared based on the number of co-crystal hit obtained as a result of solid form characterisation.

1.10.3 Effect of stoichiometry on nucleation kinetics in multicomponent systems

Nucleation kinetics measurements using induction time in co-crystals is one of the main areas that is not investigated until now. Specifically, the effect of solution stoichiometry on the nucleation of a multicomponent system. The phase diagram from chapter 3 will be used to select the solution stoichiometry where co-crystals can be formed. Induction time measurement of the co-crystals at different solution stoichiometries and supersaturations are presented. These would be analysed using the classical nucleation theory in order to determine the

thermodynamic and kinetic parameter for the co-crystal in three different solvents in an attempt to understand co-crystal nucleation kinetics.

1.10.4 Template enhanced induction time probability distribution measurements using temperature Probes

One of the limitations for determining primary nucleation when templates are introduced into the system is the perpetual blockage of light. This chapter focusses on solving this problem and use the solution to determine template assisted nucleation. The objective is to develop a complimentary approach to turbidity for determining induction time in system with well-defined templates at higher concentrations. The possibility of using the rise in temperature upon crystallization as a detection for the occurrence of nucleation will be exploited

1.11 Reference

1. Jiang, S., Ter Horst, J.H. Crystal nucleation rates from probability distributions of induction times. Cryst Growth Des. 2011;11(1):256–61.

2. Kulkarni, S.A., Kadam, S.S., Meekes, H., Stankiewicz, A.I., Ter Horst, J.H. Crystal nucleation kinetics from induction times and metastable zone widths. Cryst Growth Des. 2013;13(6):2435–40.

3. Davey, R.J., Back, K.R., Sullivan, R.A. Crystal nucleation from solutions - Transition states, rate determining steps and complexity. Faraday Discuss. 2015;179:9–26.

4. Caridi, A., Kulkarni, S.A., Di Profio, G., Curcio, E., Ter Horst, J.H. Template-induced nucleation of isonicotinamide polymorphs. Cryst Growth Des. 2014;14(3):1135–41.

5. Kulkarni, S.A., McGarrity, E.S., Meekes, H., Ter Horst, J.H. Isonicotinamide self-association: The link between solvent and polymorph nucleation. Chem Commun. 2012;48(41):4983–5.

6. ter Horst, J.H., Deij, M.A., Cains, P.W. Discovering new co-crystals. Cryst Growth Des. 2009;9(3):1531–7.

7. Urbanus, J., Mark Roelands, C.P., Verdoes, D., Jansens, P.J., Ter Horst, J.H. Co-crystallization as a separation technology: Controlling product concentrations by co-crystals. Cryst Growth Des. 2010;10(3):1171–9.

8. Urbanus, J., Roelands, C.P.M., Mazurek, J., Verdoes, D., Ter Horst, J.H. Electrochemically induced co-crystallization for product removal. CrystEngComm. 2011;13(8):2817–9.

9. Yadav, A. V, Shete, A.S., Dabke, A.P., Kulkarni, P. V, Sakhare, S.S. Co-crystals: a novel approach to modify physicochemical properties of active pharmaceutical ingredients.

Indian J Pharm Sci. 2009;71(4):359–70.

10. Schultheiss, N., Newman, A. Pharmaceutical Cocrystals and Their Physicochemical Properties. Cryst Growth Des. 2009;9(6):2950–67.

11. Trask, A. V. An Overview of Pharmaceutical Cocrystals as Intellectual Property. Mol Pharm. 2007;4(3):301–9.

12. Ter Horst, J.H., Cains, P.W. Co-crystal polymorphs from a solvent-mediated transformation. Cryst Growth Des. 2008;8(7):2537–42.

13. Grothe, E., Meekes, H., Vlieg, E., Ter Horst, J.H., De Gelder, R. Solvates, Salts, and Cocrystals: A Proposal for a Feasible Classification System. Cryst Growth Des. 2016;16(6):3237–43.

14. Capeletti, C., Guimarães, F.F., Ribeiro, L., Martins, F.T. Spectrochimica Acta Part A : Molecular and Biomolecular Spectroscopy Salt or cocrystal of salt ? Probing the nature of multicomponent crystal forms with infrared spectroscopy. SAA. 2016;167:89–95.

15. Aitipamula, S. & Vangala, V.R. X‐Ray Crystallography and its Role in Understanding the Physicochemical Properties of Pharmaceutical Cocrystals. J Indian Inst Sci . 2017;97(2):227–43.

16. Aitipamula, S., Banerjee, R., Bansal, A.K., Biradha, K., Cheney, M.L., Choudhury, A.R., et al. Polymorphs, salts, and cocrystals: What's in a name? Vol. 12, Crystal Growth and Design. 2012. p. 2147–52.

17. Zhang, C., Xiong, Y., Jiao, F., Wang, M., Li, H. Redefining the Term of " Cocrystal " and Broadening Its Intention. Cryst Growth Des. 2019;19(3):1471–8.

18. Brittain, H.G. Cocrystal Systems of Pharmaceutical Interest : 2011. Cryst Growth Des. 2012;12:1046 − 1054.

19. Li, Z., J., M.A. Influence of Coformer Stoichiometric Ratio on Pharmaceutical Cocrystal Dissolution: Three Cocrystals of Carbamazepine/4- Aminobenzoic Acid. Mol Pharm. 2016;13(3):990–5.

20. Almansa, C., Merce, R., Tesson, N., Farran, J., Toma, J. Co-crystal of Tramadol Hydrochloride − Celecoxib (ctc): A Novel API − API Co-crystal for the Treatment of Pain. Cryst Growth Des. 2017;17:1884–92.

21. Grzesiak, A.L., Lang, M., Kim, K., Matzger, A.J. Comparison of the Four Anhydrous Polymorphs of Carbamazepine and the Crystal Structure of Form I. J Pharm Sci. 2003;92(11):2260–71.

22. Li, J., Bourne, S.A., Caira, M.R. New polymorphs of isonicotinamide and nicotinamide. Chem Commun. 2011;47(5):1530–2.

23. Ferrari, E.S., Davey, R.J., Cross, W.I., Gillon, A.L., Towler, C.S. Crystallization in Polymorphic Systems : The Solution-Mediated Transformation of to r Glycine 2003. 2003;1–8.

24. Castro, R.A.E., Maria, T.M.R. CrystEngComm Resolved structures of two picolinamide polymorphs . Investigation of the dimorphic system behaviour under conditions relevant to co-crystal synthesis. CrystEngComm. 2012;14:8649–57.

25. Powell, K.A., Bartolini, G., Wittering, K.E., Saleemi, A.N., Wilson, C.C., Rielly, C.D., et al. Toward Continuous Crystallization of Urea-Barbituric Acid : A Polymorphic Co-Crystal System. 2015;

26. Aitipamula, S., Chow, P.S., Tan, R.B.H. Polymorphism in cocrystals: a review and assessment of its significance. CrystEngComm. 2014;6:3451–65.

27. Bauer, J., Spanton, S., Henry, R., Quick, J., Dziki, W., Porter, W., et al. Ritonavir: An

extraordinary example of conformational polymorphism. Pharm Res. 2001;18(6):859–66.

28. Kavanagh, O.N., Croker, D.M., Walker, G.M., Zaworotko, M.J. Pharmaceutical cocrystals : from serendipity to design to application. Drug Discov Today. 2018;1–9.

29. Grecu, T., Adams, H., Hunter, C.A., Mccabe, J.F., Portell, A., Prohens, R. Virtual Screening Identifies New Cocrystals of Nalidixic Acid. Cryst Growth Des. 2014;14:1749−1755.

30. Springuel, G., Norberg, B., Robeyns, K., Wouters, J., Leyssens, T. Advances in Pharmaceutical Co-crystal Screening : Effective Co- crystal Screening through Structural Resemblance Ge r. Cryst Growth Des. 2012;12:475–84.

31. Friščić, T., Childs, S.L., Rizvi, S.A.A., Jones, W. The role of solvent in mechanochemical and sonochemical cocrystal formation: a solubility-based approach for predicting cocrystallisation outcome. CrystEngComm. 2009;11(3):418–26.

32. Hasa, D., Miniussi, E., Jones, W. Mechanochemical Synthesis of Multicomponent Crystals: One Liquid for One Polymorph? A Myth to Dispel. Cryst Growth Des. 2016;16(8):4582–8.

33. Yuan, Y., Wang, L., Li, D., Deng, Z., Zhang, H. How Many Parameters Can Affect the Solid Form of Cocrystallization Products in Mechanochemical Reactions? A Case Study. Cryst Growth Des. 2018;18:7244–7.

34. Mullin, J.W. Crystallization. 4th ed. Boston: Butter-Worth-Heinemann; 2001.

35. Reus, M.A., Heijden, A.E.D.M. Van Der, Horst, J.H. Solubility Determination from Clear Points upon Solvent Addition. Org Process Res Dev. 2015;19:1004–11.

36. Li, B., Wu, Y., Zhu, J., Chen, K., Wu, B., Ji, L. Determination and correlation of

solubility and mixing properties of isonicotinamide (form II) in some pure solvents. Thermochim Acta. 2016;627–629:55–60.

37. Wenju, L., Leping, D., Black, S., Hongyuan, W. Solubility of carbamazepine (form III) in different solvents from (275 to 343) K. J Chem Eng Data. 2008;53(9):2204–6.

38. Chadwick, K., Davey, R., Sadiq, G., Cross, W., Pritchard, R. The utility of a ternary phase diagram in the discovery of new co-crystal forms. CrystEngComm. 2009;11(3):412–4.

39. Gagniere, E., Mangin, D., Veesler, S., Puel, F. Co-crystallization in solution and scale-up issues. RSC Drug Discov Ser. 2012;16(Copyright (C) 2013 American Chemical Society (ACS). All Rights Reserved.):188–211.

40. Yu, Z.Q., Chow, P.S., Tan, R.B.H. Operating regions in cooling cocrystallization of caffeine and glutaric acid in acetonitrile. Cryst Growth Des. 2010;10(5):2383–7.

41. Chiarella, R.A., Davey, R.J., Peterson, M.L. Making co-crystals - The utility of ternary phase diagrams. Cryst Growth Des. 2007;7(7):1223–6.

42. Grecu, T., Hunter, C.A., Gardiner, E.J., Mccabe, J.F. Validation of a Computational Cocrystal Prediction Tool: Comparison of Virtual and Experimental Cocrystal Screening Results. Cryst Growth Des. 2014;14:161–71.

43. Kashchiev, D., van Rosmalen, G.M. Review: Nucleation in solutions revisited. Cryst Res Technol. 2003;38(78):555–74.

44. Davey, R.J., Schroeder, S.L.M., ter Horst, J.H. Nucleation of Organic Crystals-A Molecular Perspective. Angew Chemie Int Ed. 2013;52(8):2166–79.

45. Weissbuch, I., Lahav, M., Leiserowitz, L. Understanding of Crystal Nucleation. Cryst Growth Des. 2003;3(2):125–50.

46. Vekilov, P.G. Nucleation. Cryst Growth Des. 2010;10(12):5007–19.

47. Heffernan, C., Ukrainczyk, M., Zeglinski, J., Hodnett, B.K., Rasmuson, Å.C. Influence of Structurally Related Impurities on the Crystal Nucleation of Curcumin. Cryst Growth Des. 2018;18(8):4715–23.

48. Rasmussen, D. H.; Loper, C. R., J. Rasmussen, D. H.; Loper, C. R., Jr. Acta Met. 1976;24:117–23.

49. Xiao, Y., Wang, J., Huang, X., Shi, H., Zhou, Y., Zong, S., et al. Determination Methods for Crystal Nucleation Kinetics in Solutions. Cryst Growth Des. 2018;(18):540−551.

50. Melia T. P. Crystal nucleation from aqueous solution. J appl Chem. 1965;15:345–57.

51. Ildefonso, M., Candoni, N., Veesler, S. Heterogeneous nucleation in droplet-based nucleation measurements. Cryst Growth Des. 2013;13(5):2107–10.

52. Hammadi, Z., Grossier, R., Zhang, S., Ikni, A., Candoni, N., Morin, R., et al. Localizing and inducing primary nucleation. Faraday Discuss. 2015;179:489–501.

53. Brandel, C., Ter Horst, J.H. Measuring induction times and crystal nucleation rates. Faraday Discuss. 2015;44(179):199–214.

54. Galkin, O., Vekilov, P.G. Direct Determination of the Nucleation Rates of Protein Crystals. J Phys Chem B. 1999;103:10965–71.

55. Whiteside, G.M. The origins and the future of microfluidics. Nature. 2006;442:368–373.

56. Xiao, Y., Tang, S.K., Hao, H., Davey, R.J., Vetter, T. Quantifying the Inherent Uncertainty Associated with Nucleation Rates Estimated from Induction Time Data Measured in Small Volumes. Cryst Growth Des. 2017;17:2852–63.

57. Maggioni, G.M., Mazzotti, M. Stochasticity in Primary Nucleation : Measuring and

Modeling Detection Times. Cryst Growth Des. 2017;17:3625–35.

58. Kashchiev, D. Nucleation: Basic Theory with Applications. Butterworth-Heinemann. 2000. 315–329 p.

59. Davey, R.J., Schroeder, S.L.M., Ter Horst, J.H. Nucleation of organic crystals - A molecular perspective. Angew Chemie - Int Ed. 2013;52(8):2167–79.

Chapter 2

Instrumentation

2.1 Introduction

The objective of this chapter is to give background information and highlight the basic principles of the main equipment used for generating data. The specific details of the instrumental parameters used in the research experiments will be addressed in the specific chapters where it was used.

2.2 Saturation temperature – Clear point measurements

An important part of a crystallisation process and drug discovery is the solubility determination. Solubility is the amount of the compound a solvent can hold at a specific temperature. There are various methods to determine solubility. One generally used method in pharmaceutical industry is the high performance liquid chromatography (HPLC) and in some cases quantitative nuclear magnetic resonance (qNMR).[1] HPLC requires more sample preparation than NMR. However, one other method that involves minimal sample preparation that has been demonstrated useful for solubility determination is based on transmission of light. This principle was used in Crystal 16® and crystalline crystallisation platforms.[2]

2.2.1 Crystal16

Crystal 16® is a high throughput platform designed with 16 wells to hold 16 standard HPLC glass vials with a capacity of up to 1.8mL. It works by measuring turbidity changes of a dispersed suspension as a result of temperature changes in the well by heating and cooling. Turbidity is a measure of passage of light through a sample. If a suspension is present in the vial, the light is blocked and transmission of light is reduced. If a clear solution is present in the vial, the light passes through the sample undisturbed which results in maximum transmission of light. Upon increasing the temperature of a suspension in the vials, the light transmission through the samples reaches an upper limit, as the crystals dissolves in the solvent, the suspension turns into clear solution. This upper limit is the clear point temperature. When this

clear solution is cooled to an adequate supersaturation, nucleation will occur and the presence of crystals will obstruct the transmission of light. The temperature at which this happens is the cloud point temperature T_c.

2.2.2 Crystalline

Crystalline works on the same principle as crystal16 but with 8 reactors with higher volume capacity of up to 10ml. Unlike crystal16, Crystalline is better than crystal 16 in terms of crystallisation monitoring and control. It is equipped with camera to monitor particle size, crystal morphology and was recently used for measurement of secondary nucleation.[3] It is also an ideal platform for other crystallisation modalities like antisolvent crystallisation.

2.3 X-ray diffraction

Crystallisation as a purification process may result in crystals of various size or morphology depending on the conditions. The resulting crystalline materials can be described by using unit cells that are made up of atoms or molecules arranged in periodic array with a long range order with or without defects. The important thing is that the defects where present, does not have an effect on the averaged structure due to the long range of the crystal. The shape of the unit cell is described using vectors (a, b, c) and the angles (α, β, γ) between them. For example, based on convention, the angle α is between b and c, the angle β is between a and c, and the angle γ is between a and b. Using the unit cell, we can describe a set of crystallographic planes that runs through the crystal that helps the determination of the crystal structure. A set of crystallographic planes are parallel and equally spaced to each other. The d-spacing of these planes is in the order of angstroms hence we are able to use X-ray radiation to examine the crystalline form due to the wavelength of X-rays being comparable to the interplanar distances.

X-rays are generated through movement of high energy electrons either by bombardment with metal targets in case of X-ray tube or through the use of synchrotron radiation where electrons are generated using accelerators and their speed increased via booster rings before being stored in the synchrotron ring for use. Either way, the generated X-ray is between 0.5 and 2.5Å which is smaller than the gap between the nearest two atoms in an array. [4][5] The interaction of the X-ray with a point source S1 may lead to spherically elastic scattering where the resulting wave is the same frequency as the incident ray; in reality the atoms are not point sources and there is a drop in the scattered intensity as a function of diffraction angle. The same scattering patterns is obtained at another point source S2. The elastic scattering from the two source points S1 and S2 may lead to the destructive interference where the wave is completely out of phase and quench one another. Alternatively the two waves may be in phase and lead to constructive interference with an increase in wave amplitude. These two scenario's depend on the relative position of the two atoms and strength of electron density, hence provide information on the crystal structure.

However, this interference or diffraction only occurs in powder diffraction if Bragg's law is satisfied. Bragg's law established relationship between diffraction angle, *d*-spacing and wavelengths of the X-ray beam. If we assume a monochromatic wave front from a X-ray tube with wavelength (λ) is incident at angle θ with the crystallographic plane of a crystalline material, a reflected (diffracted) ray can be considered to be at the same angle with the crystallographic plane. Since X-ray can penetrate deeper into the material where additional reflections occurs at numerous consecutive parallel planes. The path difference between the incident and reflected ray for the multi-layer crystallographic plane for a constructive interference is

$$\Delta = n\lambda = dsin\theta \quad 14$$

The total path difference is then written as

$$n\lambda = 2dsin\,\theta \quad 15$$

Where *d* is the interplanar spacing of neighbouring planes and 2θ is the diffraction angle. electrons. The scattering of X-rays by atoms produces a diffraction pattern, which contain information about the atom arrangement with the crystal producing constructive interference at specific angles. Diffraction by electrons of the unit cell on the same plane with *d*- spacing is only possible at certain angles. In powder diffraction pattern, this relationship is represented by the scattered intensity (represented as the total count) as a function of a single independent variable 2θ.

2.3.1 Powder diffraction

The interaction between the X-ray beam and powder samples provide a diffraction pattern (PXRD) that gives information about the nature and arrangement of the solid form. This diffraction is a unique finger print that can be used to differentiate chemically similar compounds that may be difficult to differentiate using other technique[(6)] making PXRD a standard in characterising solid forms. It can also be used qualitatively to analyse mixtures to determine percentage compositions of one component relative to the other.

Powder diffraction can used to determine the crystallinity of pharmaceutical powder sample. A pharmaceutical powder can be described as crystalline or amorphous.[(7)] In reality these two types of powder exists in a sample at various degrees. Amorphous powder are described to have lost the long range order so do not give Braggs diffraction peaks in the X-ray beam. The

resulting pattern of an amorphous X-ray typically resembles a broad hump or multiple broad humps. These pattern is also typical of nanocrystals.

Microcrystalites in powder maintains the long range order so give rise to the Bragg's diffraction identifiable as distinct peaks as part of a unique pattern. These patterns can be compared or match to differentiate a new solid form such as polymorph or co-crystal. PXRD data collection are usually obtained at ambient conditions.

2.3.2 Sources of error in powder diffraction

Sample volume[5], sample height displacement[8], preferred orientation and particle statistics are some of common sources of errors in PXRD. These errors can originate from the sample preparations procedure so it is important to minimise these errors. Sample height displacement is described when sample height is different to the focal plane of the X-ray beam. This will result in a shift in the peak positions in the pattern. Preferred orientation is very common this is especially common in crystal particles that aligns in a manner that minimise random arrangements of crystals especially in needle or plate - like crystals. Preferred orientation is minimised by using transmission mode of data collection instead of reflection mode or rotate the sample plates in both reflection or transmission mode as the sample is collected. Ideally the only way to completely eliminate a preferred orientation is to have a spherical crystal sample. The ideal sample size for powder diffraction is < 20μm so large crystal size can be reduced by grinding preferably when there is no change in the solid form. Alternatively the sample can be sieved of the morphology of the crystals is the similar.

2.4 Nuclear magnetic resonance (^{1}H-NMR)

Nuclear magnetic resonance spectroscopy is the study of molecules based on the interactions between radiofrequency (electromagnetic radiations) of a nuclei of a molecule placed in a strong magnetic field. The radiations used are low energy, high wavelength. Nuclei such as ^{1}H

among other type of nuclei possess a spin angular momentum on its axis. The spinning of an electron in its orbitals creates a localized magnetic effect. If this electron is placed in a stronger external magnetic field.

Nuclear magnetic resonance is a phenomenon which occurs when the nuclei of ^{1}H, atoms are immersed in a static magnetic field (B) and exposed to a second oscillating magnetic field (B_o). These atoms contains protons, electrons, and neutrons capable of a fundamental property called spin. Spin comes in multiples of 1/2 and can be + or -. A proton with spin can be visualized as a small magnet. When placed in a magnetic field of strength B, the proton could aligns in low energy so that north pole is attracted to south of the external magnet and at high energy so that north is attracted to north of the external magnet. The transition between these energy levels is initiated by absorption of a photon. The energy, E, of a photon is related to its frequency, ν, by Planck's constant.

$$E = h\nu \qquad 16$$

When the energy of the photon matches the energy difference between the two spin states an absorption of energy occurs.

2.4.1 Chemical shift

The signal in NMR spectroscopy results from the difference between the energy absorbed by the spins which make a transition from the lower energy state to the higher energy state, and the energy emitted by the spins which simultaneously make a transition from the higher energy state to the lower energy state. When an atom is placed in a magnetic field, its electrons circulate about the direction of the applied magnetic field. This circulation causes a small magnetic field

at the nucleus which opposes the externally applied field. The magnetic field at the nucleus is therefore generally less than the applied field by a fraction β.

$$B = B_o (1 - \beta) \quad 17$$

The electron density around each nucleus in a molecule varies according to the types of nuclei and bonds in the molecule and shift perpendicular to it in a magnetic field. The chemical shift of a nucleus is the difference between the resonance frequency of the nucleus and a standard, relative to the standard this change is small. This quantity is reported in ppm and given the symbol delta (δ).

The chemical shift is a very precise metric of the chemical environment around a nucleus.[9]. Proton of a molecule can have different resonance frequency. The chemical shift of protons of the same molecule can be can be in different environment because of the shielding effect of the electron. The spectra obtained can give information about the neighbouring protons and the number of protons responsible for a peak. The number of the neighbouring protons can be determined through peak integrations.

2.4.2 Integration

To obtain accurate peak integration, the chemical shift must be in phase and the baseline of the spectrum must be suitable. Peak integration is the relative area a chemical shift occupies of in the spectrum. Here an absorption peak is defined as the family of peaks centered at a particular chemical shift. For example, if there is a triplet of peaks at a specific chemical shift, the integration is the sum of the area of the three. The rule is that peak area is proportional to the number of protons.

2.5 Temperature probe

The temperature probe and thermocouple data logger used was supplied by Technobis.[10] The temperature probes are made from stainless steel and are connected to 8 channel thermocouple data logger that measures from –270 to +1820 °C at a fast sampling rate up to 10 measurements per second including cold junction compensation (CJC). The thermocouple data logger is connected to the computer by using universal serial bus (USB). The thermocouple was controlled and data collected using PicoLog 6.

2.6 Reference

1. Holzgrabe, U., Deubner, R., Schollmayer, C., Waibel, B. Quantitative NMR spectroscopy - Applications in drug analysis. J Pharm Biomed Anal. 2005;38(5 SPEC. ISS.):806–12.
2. Reus, M.A., Heijden, A.E.D.M. Van Der, Horst, J.H. Solubility Determination from Clear Points upon Solvent Addition. Org Process Res Dev. 2015;19:1004–11.
3. Briuglia, M.L., Sefcik, J., Horst, J.H. Measuring Secondary Nucleation through Single Crystal Seeding. Cryst Growth Des. 2018;19:421–9.
4. Thakral, N.K., Zanon, R.L., Kelly, R.C., Thakral, S. Applications of Powder X-Ray Diffraction in Small Molecule Pharmaceuticals : Achievements and Aspirations. J Pharm Sci. 2018;107(12):2969–82.
5. Pecharsky VK, Z.P.F. Fundamentals of Powder Diffraction and Structural Characterization of Materials. 2nd ed. New York, Springer; 2009.
6. StephensonX, G.A., Stowell, O.G., Toma, P.H., Pfeiffer, R.R., Byrn, S.R. Solid-State Investigations of Erythromycin A Dihydrate: Structure, NMR Spectroscopy, and Hygroscopicity. J Pharm Sci. 1997;86(11):1239–44.
7. Karmwar, P., Graeser, K., Gordon, K.C., Strachan, C.J., Rades, T. Investigation of properties and recrystallisation behaviour of amorphous indomethacin samples prepared by different methods. Int J Pharm. 2011;417(1–2):94–100.
8. Chen, X., Bates, S., Morris, K.R. Quantifying amorphous content of lactose using parallel beam X-ray powder diffraction and whole pattern fitting. J Pharm Biomed Anal. 2001;26(1):63–72.
9. Atta-ur-Rahman, M.I.C. and A.-W. Solving Problems with NMR Spectroscopy (Second Edition) 2016, Pages 1-34. 2nd ed. academic press; 2016.
10. www.picotech.com.

Chapter 3

Effect of Solvent and Solution Stoichiometry on the Co-crystal Solubility and Phase Diagram

Abstract

A systematic approach based on a small number of clear point temperature measurements was developed and used to estimate the phase diagram of CBZ-INA in ethanol, nitromethane and 1,4 dioxane. This method allows a quick determination of the compositional range of the co-crystal region. The method assumes that the solubility of one pure component is not influenced by the presence of the other and that the ratio of solution concentration of the co-crystal components does not influence the co-crystal solubility product. However, experimental solubility data generated in ethanol and nitromethane suggest that such solution stoichiometric effects can influence the co-crystal solubility product. The skewedness of the co-crystal region in the phase diagram depends on the solubility of the pure components.

3.1 Introduction

The continuing research into co-crystal in the pharmaceutical industry is driven by the possibility to tune and enhance the physicochemical properties of active pharmaceutical ingredients in medicinal products.[1][2] Co-crystal can be defined as materials composed of two or more neutral molecular components[3] in a defined stoichiometric ratio associated with non-ionic and noncovalent bonds that are solid at room temperature.[4] Co-crystallisation can be used to enhance physicochemical properties such as solubility, bioavailability[5] and stability of a pharmaceutical product.[6] co-crystallization is used as a separation technology, for example the product removal of cinnamic acid and 3-nitrobenzoic acid co-crystal as a model for fermentation process [7]

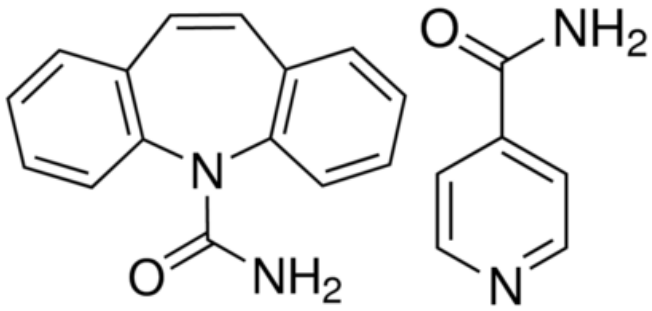

Figure 9. Molecular structure of carbamazepine CBZ (left) and isonicotinamide INA (right)

Solution co-crystallization, for instance through cooling crystallization, is an often used co-crystal preparation technique.[8][9][10][11] An important step in the design and optimisation of a solution co-crystallization is the determination of the phase diagram.[9][12][13] The knowledge on the phase diagram can inform other areas of the co-crystallization process such as the discovery of new co-crystal form,[12] the study of co-crystallization kinetics[14][15] and polymorph discovery.

In addition to temperature and pressure, solvent choice and solutes composition are factors that can affect a phase diagram, for example, the asymmetry phase diagram of ibuprofen and nicotinamide in pure ethanol was influenced by the use of ethanol/water mixture to obtain a symmetric phase diagram[16] and it has been proven that change in compositions at the triphasic region of the phase diagram produces a new condition that can significantly influence solid form outcome of crystallization.[17] The use of a new method for construction of the phase diagram requires understanding the effect of these factors on the cocrystal and pure component solubilities.

This work aims to develop an experimentally fast and efficient method to construct a phase diagram in a multicomponent system using carbamazepine and isonicotinamide in Figure 9 as a model compounds. The co-crystal CBZ –INA formed from these two compounds is carefully studied and the solid form stoichiometric ratio is 1:1. [8] [11] The stability of the co-crystal form I and II is well known. The stable form I has a plate-like morphology and the needle-like crystals of the metastable form II make them visually distinguishable. First, a series of clear points was measured. Then the effect of solvent and solution stoichiometry on the co-crystal solubility product will be investigated. Finally, the effect of the pure component relative solubility symmetry on the phase diagram will be determined.

3.2 Methods

Carbamazepine form III (≥98%), isonicotinamide form I (99%), ethanol (99.9%), nitromethane (≥95%), anhydrous dioxane (99%), methanol-*d*4 (99.8%) were used as received from Sigma Aldrich. Form III CBZ and form I INA are the bulk starting material for all the experiment.Clear point temperature measurements

The clear and cloud point temperatures of samples of known compositions were determined using the Crystal16 multiple reactors (Technobis, The Netherlands) designed with 16 wells to

hold 16 standard HPLC glass vials with a capacity up to 1.8mL. Upon heating a suspension with known overall composition, the underlying solubility of the system increases and the suspension partially dissolves. If the solubility is higher than the overall composition, the suspension turns into a clear solution since all crystals dissolve. The presence of a suspension is measured by the transmission of light through the sample. The transmission of light is (partially) blocked by a suspension while light can pass through the sample relatively unhindered in a clear solution. The transmission of light is calibrated using a clear solution so that the temperature at which the transmission of light becomes 100% can be determined. This is the clear point temperature which can be taken to estimate the saturation temperature if the heating rate is sufficiently slow.

Suspension samples were heated at 0.3°C min^{-1} to a temperature T_x that is at most 15°C below the boiling point of the solvent used. The clear point temperature was determined during the heating stage of the temperature profile. The heating rate was chosen sufficiently low to assume that the determined clear point temperature is equal to the saturation temperature of the composition. If a suspension was present at the high temperature T_x the sample was discarded. The sample was held at a high temperature T_x for 10 minutes. The solution was then cooled to 5°C or higher using a cooling rate of 0.3°C min^{-1} in order to recrystallize the sample. The procedure was repeated twice to get 3 clear point temperature measurements per sample.

In case of three-component samples of API, co-former and ethanol, triplicate clear points for a series of 4 samples was measured at the same molar stoichiometry of API and co-former with different total solid concentrations by varying coformer. For three-component samples of API, co-former and other solvents, triplicate clear points for a series of 4 samples was measured at the same molar stoichiometry of API and co-former with different total solid concentrations by varying API.Crystallisation and characterisation of crystalline samples

Samples (3 mL) of various compositions having a saturation temperature of 45°C concerning the co-crystal compound were prepared in 6mL vials. After dissolution at a high temperature the samples were quickly cooled to 35°C at 5°Cmin^{-1}. The samples were then held at 35°C until crystals were detected after which they were filtered under vacuum. The obtained crystals were dried for 2-3 hours at room temperature. Co-crystallisation experiments were performed for validation of the solid form outcome. The PXRD of co-crystallisation outcome were compared to those from literature [19][20][21][22] for the pure components and co-crystals.

X-ray powder diffraction of the solid sample was performed using a Brucker Advance II diffractometer with Debye – Scherrer transmission from a Cu source radiation (1.540596 Å) with an operating voltage of 40kV, current 50mA, Kα1 Johansson monochromator and 1mm anti-divergence slit. Samples were placed on an automated 28 well plate with an x-ray transparent 7.5µm Kapton film at ambient temperature. The powder patterns were processed using Brucker EVA software.

3.2.1 Determination of solution stoichiometry for eutectic points compositions

Solution samples were prepared with an overall composition in the predicted triphasic region. The samples were filtered with a PPE acrodisk 0.25µm filters, after crystallisation and equilibration for at least 24 hours at 35°C. The solution stoichiometry was determined using ^{1}H-NMR while XRPD was used to analyse the solid phase. Integration of the proton signals using the automatic and manual integration functions available in the Topspin 3.7 software lead to a peak surface area per proton for both CBZ (A_{CBZ}) and INA (A_{INA}). Methanol *d*4 was used as a solvent in the NMR experiment because both CBZ and INA have excellent solubility in methanol. The peak surface areas per proton of CBZ (A_{CBZ}) and INA (A_{INA}) per proton of INA were used to determine the NMR based solution stoichiometry y_{NMR} in the equilibrated samples.

NMR based solution stoichiometry y_{NMR} is represented by $y_{NMR} = A_{CBZ}/(A_{CBZ}+A_{INA})$. The equilibrated samples were made from a known composition of x_{CBZ} and x_{INA} represented by $y_{CBZ} = x_{CBZ}/(x_{CBZ}+x_{INA})$. Solution stoichiometry y_{CBZ} is the solvent free mole fraction of the co-crystal components.

Calibration was performed by mixing CBZ and INA at various stoichiometric ratios of y_{CBZ} 0.402, 0.315 (duplicated to investigate accuracy) and 0.233 as shown in Figure 10. In this range, a sufficiently good linear fit is given by $y_{NMR} = uy_{CBZ}$ with u=1.15 ± 0.026, indicating that the CBZ proton signals are slightly stronger than those for INA. Signals representing one or two associated protons were used to simplify analysis. For CBZ the olefinic protons with their chemical shift at δ 6.9 and for INA the doublet peaks at δ 8.6 and 7.8 were selected for calibration. Therefore, the multiplet signals of the aromatic ring of CBZ at δ 7.30 –7.34 and δ 7.41–7.43 were not used. The peaks that accompany the chemical shift for amide at δ 4.8 in CBZ samples were not used because they overlap with the signals for the amide protons in INA which makes signal deconvolution complicated. Details of chemical shift integration is presented in appendix A

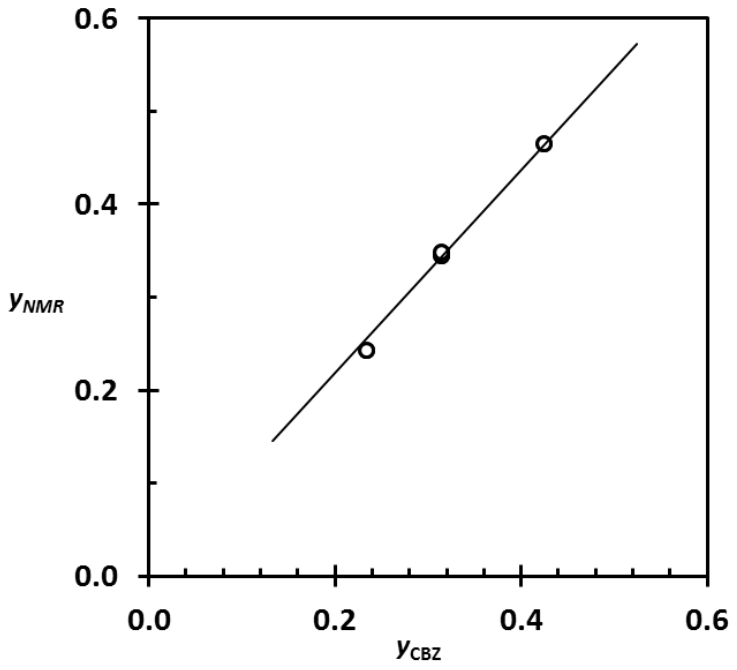

Figure 10. ^{1}H-NMR calibration for the solution stoichiometry determination. NMR based solution stoichiometry y_{NMR} is a function of the molar solution stoichiometry y_{CBZ}. An excellent linear fit is given by $y_{NMR} = uy_{CBZ}$, with $u = 1.15 \pm 0.026$ indicating that the CBZ proton shift signals are slightly stronger than those for INA.

3.3 Result

The phase diagram of CBZ, INA and solvent and its temperature dependence are presented. Extending a previously reported method,[8] the phase diagram of CBZ and INA in various solvents is systematically studied in order to understand the role of solution stoichiometry and solvent on the co-crystal solubility. This study consists of four steps: (I). Determination of the pure components solubilities in a solvent; (II). Determination of saturation temperature of the mixed compositions at various solution stoichiometries; (III). Determination of the eutectic points in solvent systems; (IV). Construction of the phase diagram. The phase diagram is validated through characterisation of the crystallized products of various compositional samples. The solvent selection was based on the work of Kulkarni et al.[18] where INA is demonstrated to interact differently in ethanol, nitromethane and dioxane through self-association.

3.3.1 Pure component solubilities

Figure 11 shows the temperature dependent mass based solubilities of Carbamazepine (CBZ) and Isonicotinamide (INA) in the solvents ethanol (EtOH), nitromethane (NM) and dioxane (DIO). At 45°C the solubilities of carbamazepine and isonicotinamide are 53.4 and 134.5 $mgmL^{-1}$ in ethanol, 103.6 and 34.9 $mgmL^{-1}$ in nitromethane, 104.3 and 48.2.$mgmL^{-1}$ in dioxane, respectively. While isonicotinamide has a higher solubility than carbamazepine in ethanol, this is reversed in the other solvents. At a temperature of 45°C the solubility of isonicotinamide in ethanol is roughly 4 and 2.7 times that in nitromethane and dioxane respectively. The solubility of carbamazepine and isonicotinamide in ethanol match well with previously measured

data.[19][20][21] As far as we know, there is no report of the solubility of carbamazepine and isonicotinamide in nitromethane and dioxane.

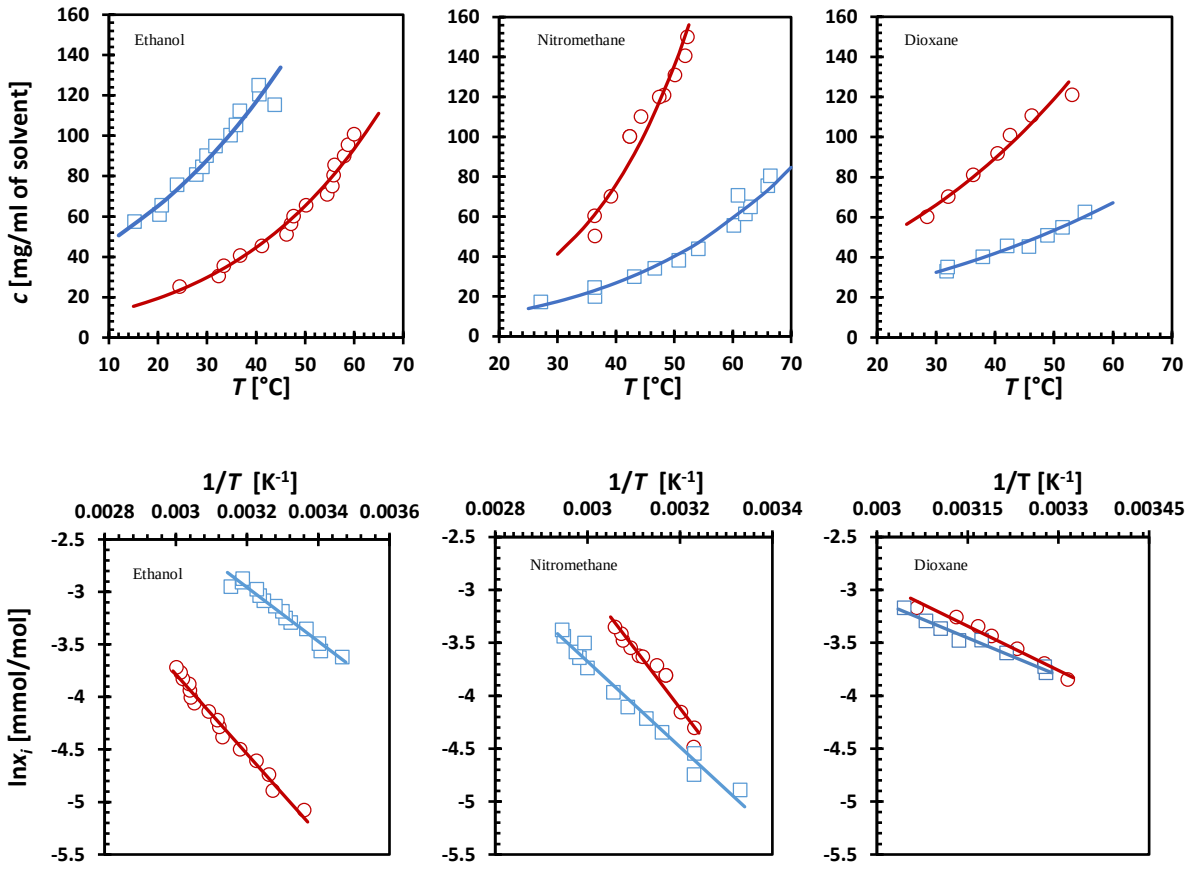

Figure 11. Top: Temperature dependent pure component solubilities of CBZ (o) and INA (□) (from left) in ethanol, nitromethane and dioxane. The data points were fitted using the van't Hoff equation. Bottom: The van't Hoff plot of CBZ (o) and INA (□) in, from left to right ethanol, nitromethane and dioxane. The lines are fits of van't Hoff in equation 18

The relation between molar solubilities (mole fractions) differs due to the difference in molecular weights of the components involved. The molar solubility of carbamazepine is almost equal to that of isonicotinamide in dioxane, about 6 times lower than isonicotinamide in ethanol and two times higher than isonicotinamide in nitromethane. Therefore, amongst the three solvents used the highest molar solubility of carbamazepine is in dioxane system and the lowest in ethanol.

In a single component system, the temperature dependent solubility can often be fitted well within a sufficiently narrow temperature region using the van't Hoff equation.

$$\ln(x_i) = -\frac{\Delta H}{R}\left(\frac{1}{T} - \frac{1}{T_0}\right) = A\left(\frac{1}{T}\right) + B \qquad 18$$

Where R is the gas constant, ΔH is the heat of fusion and T_0 is the melting temperature. The van't Hoff equation gives a relation between the molar fraction saturation concentration x_i and the saturation temperature T depending on the melting enthalpy and melting temperature. Rather than use the actual heat of fusion and melting temperature values, we used fitting parameters A and B respectively as in equation 18

3.3.2 Co-crystal solubility

The compositional region for the formation of co-crystals from a solution is not governed by the co-crystal stoichiometry (e.g., 1:1 for the CBZ: INA co-crystal solid form) but by the pure component solubilities.[9] The measured pure component solubilities indicate that in order to prepare co-crystals in ethanol, an excess of isonicotinamide is needed while in nitromethane and dioxane, an excess of CBZ is required. The molar stoichiometry of CBZ and INA in a solution can be expressed as a fraction y_{CBZ}:

$$y_{CBZ} = \frac{x_{CBZ}}{(x_{INA} + x_{CBZ})} \qquad 19$$

Thus, to determine the co-crystal solubility, specific CBZ: INA stoichiometries y^*_{CBZ} based on the pure component solubilities at a given temperature should be used. The specific

stoichiometry y^*_{CBZ} can be expressed through the pure component solubilities x^*_{CBZ} and x^*_{INA} for CBZ and INA respectively. This specific pure component solubility stoichiometry y^*_{CBZ} then can be defined as

$$y^*_{CBZ} = \frac{x^*_{CBZ}}{x^*_{CBZ} + x^*_{INA}} \qquad 20$$

Where y^*_{CBZ} is the solvent free mole fraction of CBZ in the sample mixture. This solution stoichiometry gives the highest possibility that the measurement takes place in the co-crystal region of the phase diagram.

With pure component solubilities $x^*_{CBZ} = 10.9$ and $x^*_{INA} = 52.9$ at a reference temperature $T_r = 40°C$, the solvent free mole fraction $y^*_{CBZ} = 0.171$. Using this specific stoichiometry $y^*_{CBZ} = 0.171$ at a sample composition of $x_{CBZ} = 10.9$ and $x_{INA} = 52.9$ shows a clear point temperature $T = 51.7°C$, which is higher than the reference temperature T_r. $T > T_r$ signifies co-crystal formation. Therefore the concentration product $\left(x^*_{CBZ}(T_r).x^*_{INA}(T_r)\right)$ at the referenced temperature is linked to clear point temperature T.

The solubility of a non - ionisable co-crystals with a 1:1 molar stoichiometry such as the CBZ-INA co-crystal can be expressed as the product of the component concentrations at equilibrium between co-crystal and solution. This composition can then be expressed as a solubility product $(x_{CBZ}.x_{INA})^*$ with a saturation temperature $T = 51.7°C$. The solubility product can be expressed similarly as equation 18 where A_{cc} and B_{cc} are fitting parameters.

$$\ln(x_{CBZ}.x_{INA})^* = A_{cc}\left(\frac{1}{T} + B_{cc}\right) \qquad 21$$

Figure 12 shows the van't Hoff plot of the solubility product of the co-crystal and the measured saturation temperature for a specific stoichiometry y^*_{CBZ} = 0.171 in ethanol, 0.592 in nitromethane and 0.487 in dioxane at different compositions of the CBZ and INA. According to equation 21, the fitting parameters A_{cc} and B_{cc} can then be determined so that the solubility product $(x_{CBZ}.x_{INA})^*$ of the co-crystal at a specific temperature can be estimated as shown in Table 2.

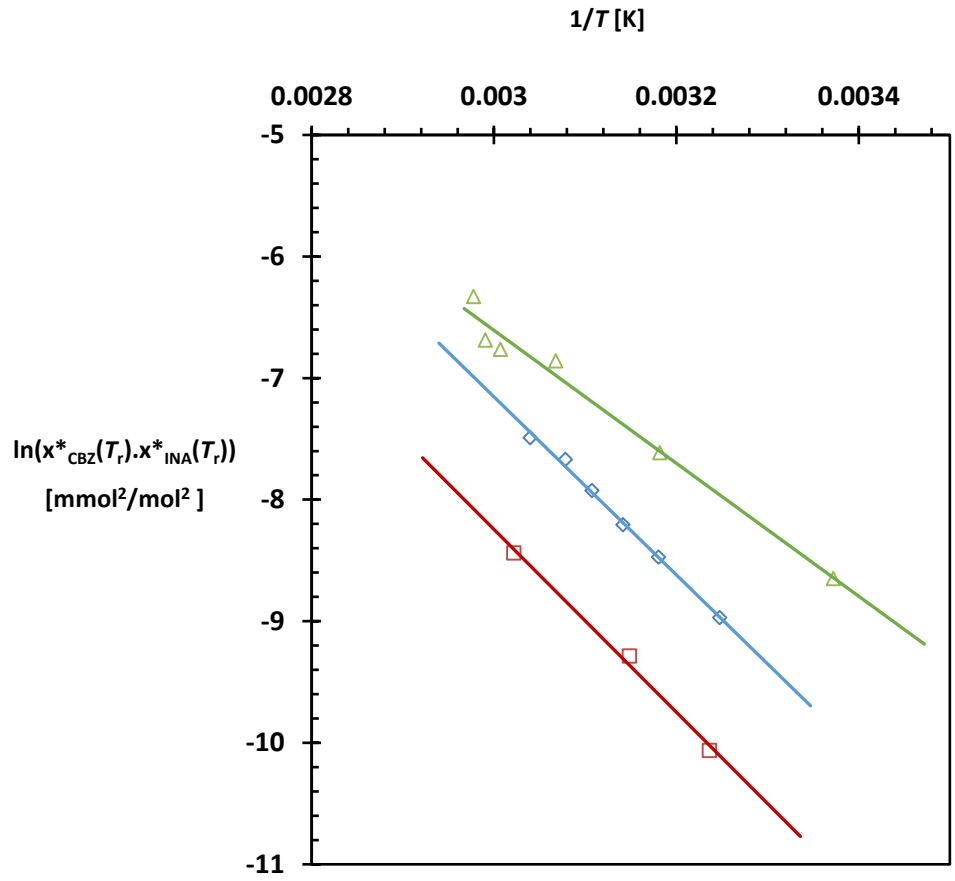

Figure 12. The van't Hoff plot of CBZ-INA co-crystal solubility in the solvents EtOH, NM and DIO for the solution stoichiometries = y^*_{CBZ} 0.171 (blue ◊), 0.592 (red □) and 0.487 (green Δ) respectively.

The parameters can then be used to estimate variables. For instances, the solubility product of the co-crystal in ethanol at a measured temperature T = 40°C is determined to be

190.3mmol^2/mol^2 with mole fractions x_{CBZ} = 10.9 and x_{INA} = 52.9. The same procedure was followed to determine the solubility product of the co-crystal at specific stoichiometry in nitromethane and dioxane at pure component solubilities stoichiometry 0.592 in nitromethane and 0.487 respectively. Table 2 shows the estimated parameters *A* and *B* for y^*_{CBZ} = 0.171 in ethanol, 0.592 in nitromethane and 0.487 in dioxane.

Table 2. Molar based solubilities x^*_{CBZ}, x^*_{INA}, their product and optimal solution stoichiometry y^*_{CBZ} at 40°C. The measured clear point temperatures at stoichiometry y^*_{CBZ} and at least three compositions for each stoichiometry result in the fitted van't Hoff parameters *A* and *B* and the molar based co-crystal solubility product$(x_{CBZ}.x_{INA})^*$ at 40°C. These lead to an estimate of the stoichiometry range y_{CBZ} (min) $<y_{CBZ}<y_{CBZ}$ (max) to use in subsequent co-crystal solubility measurements in section 3.3

Solvent	x^*_{CBZ} [mmol/mol]	x^*_{INA} [mmol/mol]	$x^*_{CBZ}.x^*_{INA}$ [mmol^2/mol^2]	y^*_{CBZ} [-]	*A* [mmol^2/mol^2]K^{-1}	*B* [mmol^2/mol^2]	$(x_{CBZ}.x_{INA})^*$ [mmol^2/mol^2]	y_{CBZ}(min) [-]	y_{CBZ}(max) [-]
EtOH	10.9	52.9	577	0.171	-7319 ± 228	14.8 ± 0.78	190.3	0.064	0.385
NM	16.9	11.6	196	0.592	-7515 ± 595	14.3 ± 1.87	61.4	0.313	0.823
DIO	31.4	28.6	898	0.487	-5311 ± 439	9.3 ± 1.36	471.3	0.377	0.677

The procedure explained above indicates a solution stoichiometry where co-crystal can be made so far $T > T_r$ and the solubility product of the co-crystal expressed as a solubility product for a solution stoichiometry. If another solution stoichiometry other than the one used as an example was selected, the solubility product could be assumed to be the same. So far the solution stoichiometry is within the co-crystal region.

Eventually, the width of the co-crystal solubility will reach a biphasic point where the solution is saturated with an excess of one pure component (CBZ) in respect to the other (INA) or where the solution is undersaturated in respect to the other pure component. A first estimate of the width of the co-crystal region in the phase diagram is given by the solvent free mole fractions y_{CBZ} (min) and y_{CBZ} (max). These are the stoichiometries at which the eutectic points are predicted, the compositional points at which the pure component solubility line of either CBZ or INA intercepts the co-crystal solubility curve.

$$y_{CBZ}(min) = \frac{\left[\frac{(x_{CBZ}.\ x_{INA})^*}{x^*_{INA}}\right]}{\left[x^*_{INA} + \frac{(x_{CBZ}.x_{INA})^*}{x^*_{INA}}\right]} \quad 22$$

$$y_{CBZ}(max) = \frac{[x^*_{CBZ}]}{\left[x^*_{INA} + \frac{(x_{CBZ}\ .x_{INA})^*}{x^*_{CBZ}}\right]} \quad 23$$

These equations are based on equation 19. The pure component solubility x_{ECBZ} of CBZ at the eutectic compositions is $x_{ECBZ} = \frac{(x_{CBZ}.x_{INA})^*}{x^*_{INA}}$ if it is assumed that isonicotinamide solubility is not influenced by the presence of carbamazepine and that the solubility product determined at stoichiometry y^*_{CBZ} is not a function of the solution stoichiometry itself. This gives us a quick and simple way to construct the phase diagram at a particular temperature neglecting the effect of solution stoichiometry on the co-crystal solubility and of the dependence of pure component solubility on the presence of the other component.

Figure 13 shows the phase diagram of carbamazepine, isonicotinamide in ethanol, nitromethane and dioxane based on the solubility measurements at only one stoichiometry y^*_{CBZ}. The straight lines from the axes that intersect the curve line are the solubility of the pure components at that temperature. It is assumed that the solubility of the pure component is unaffected by the presence of the other co-crystal former. The determined phase diagram is divided into five regions based on the expected solid form compositions. The phase diagram of the co-crystal and pure components at 45°C is divided into 5 regions. Region I is the region of the phase diagram in which the pure component solid INA is in equilibrium with the solution. Region II is the part of the phase diagram where there is equilibrium between INA, CBZ-INA and solution

of eutectic composition. Region III is where CBZ-INA is equilibrium with the solution. Region IV is where CBZ-INA and CBZ are in equilibrium with the solution while region V is where the pure CBZ is at equilibrium with solution.

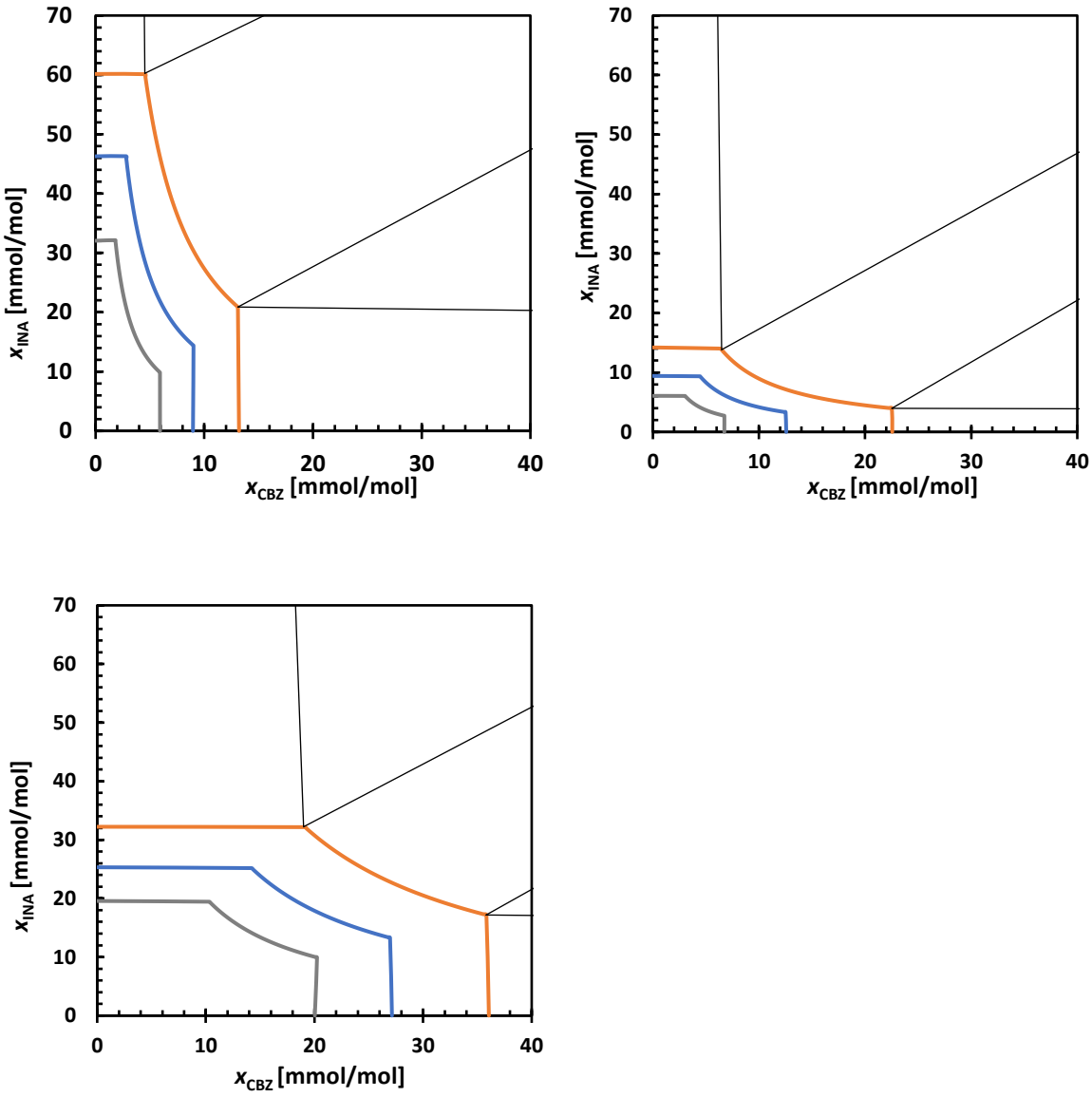

Figure 13. The phase diagram of CBZ and INA in the solvents EtOH (top left), NM (top right) and DIO at T = 45°C (yellow), 35°C (blue) and 25°C (grey) determined using the parameters in Table 2 and the pure component solubilities. The curved part of the lines is the solubility of the co-crystal. The straight lines from the axes that intersect the curve line are the solubility of the pure components at that temperature. It is assumed that the solubility of the pure component is unaffected by the presence of the other co-crystal formers.

3.3.3 The effect of solution stoichiometry on co-crystal solubility

The proposed method to construct the phase diagram in section 3.2 uses a minimal amount of measurements. As a consequence, non-ideal effects such as that of solution stoichiometry on the solubility of co-crystals are not accounted for in parameters used in the phase diagram prediction in Figure 13. The focus now shifts to determine the extent solution stoichiometry introduces deviations from the predicted co-crystal solubility product ($x_{CBZ}.x_{INA}$)* determined from solution stoichiometry y^*_{CBZ}. In order to investigate this, clear point temperatures $T(y_{CBZ})$ of samples with various solution stoichiometries y_{CBZ} (min) $<y_{CBZ} < y_{CBZ}$ (max) in all solvents involved was measured. These clear point temperatures can be compared to the $T(y^*_{CBZ})$ predicted from the parameters in table 1.

In Figure 14 the clear point temperature difference $T(y_{CBZ})$-$T(y^*_{CBZ})$ of the measured clear point temperature $T(y_{CBZ})$ and the clear point temperature $T(y^*_{CBZ})$ from the model is shown versus the actual solution stoichiometry y_{CBZ}. In ethanol, the temperature difference increases as the solution stoichiometry y_{CBZ} increases from a little less than -5°C at $y_{CBZ} = 0.1$ to around 3°C at $y_{CBZ} = 0.33$. In nitromethane, $T(y_{CBZ})$-$T(y^*_{CBZ})$ is more dispersed and the temperature difference generally increases as the solution stoichiometry y_{CBZ} increases from 0°C at $y_{CBZ} = 0.33$ to around 6°C at $y_{CBZ} = 0.75$. While noticeable temperature differences in the dioxane system are measured, there is no obvious trend with the stoichiometry.

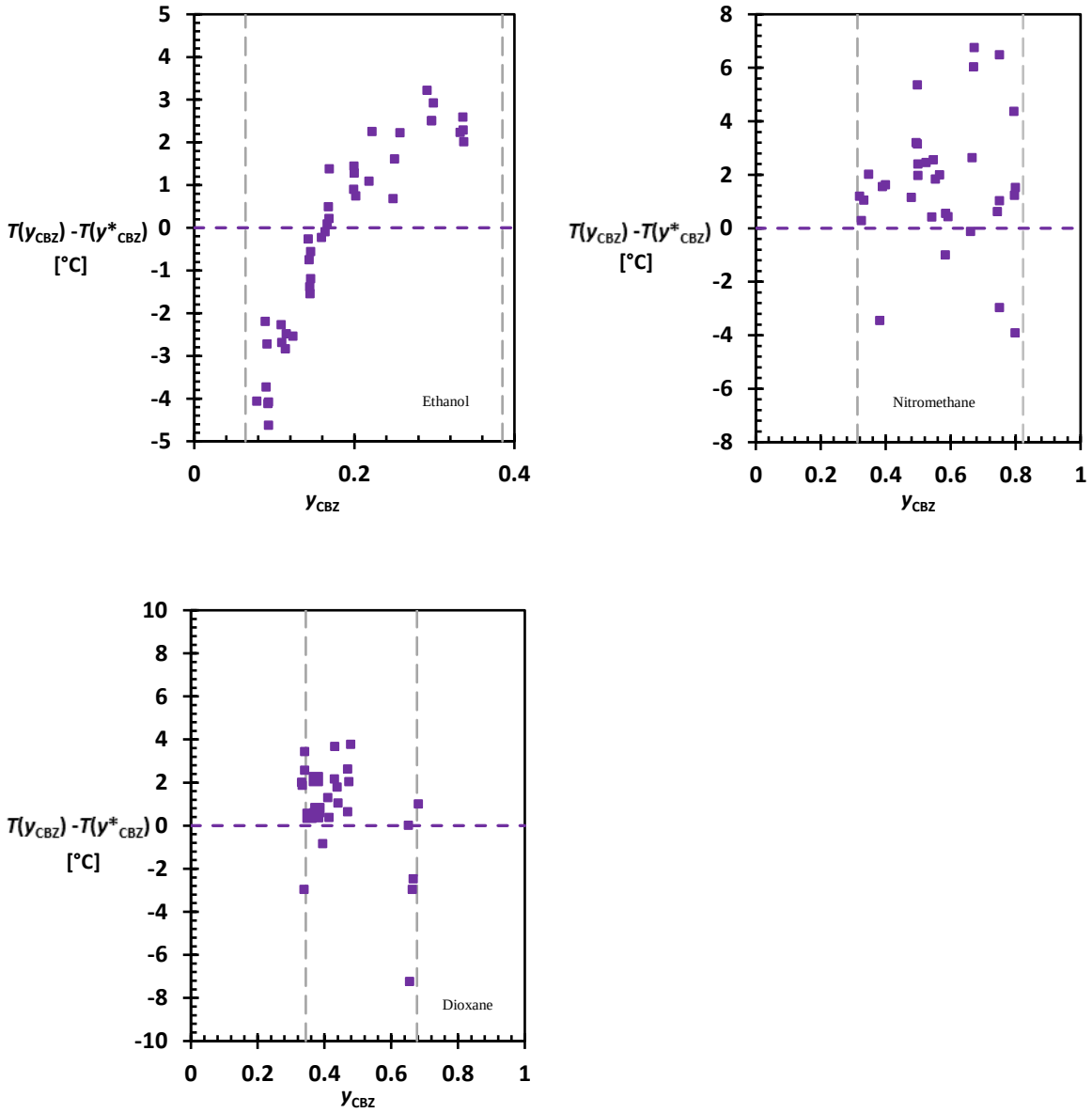

Figure 14. The clear point temperature difference $T(y_{CBZ})$-$T(y^*_{CBZ})$ purple squares versus the solution stoichiometry y_{CBZ}. The clear point temperature $T(y^*_{CBZ})$ is determined from the van't Hoff parameters (table 1) of the measured series at solution stochiometry y^*_{CBZ}. $T(y_{CBZ})$ is the measured saturation temperature for each stochiometry. The vertical grey dashed lines show y_{CBZ}(min) and y_{CBZ} (max), the estimated limits of the co-crystal region.

Van't Hoff equation similar to equation 21 shows the relationship between temperature and solubility of a component and it can be used for predicting solubility at temperature range. This equation was used in predicting the phase diagram parameters in Table 2. As demonstrated, the clear point temperature difference $T(y_{CBZ})$-$T(y^*_{CBZ})$ shows that the simple model in equation 21

does not match completely with the experimental measurements done at each solution stoichiometry. Therefore the model can be adjusted to account for the solution stoichiometry effect to give Eq. 7 by introducing an empirical solution stoichiometry dependent parameter.

$$\ln(x_{CBZ}.x_{INA})^{*} = A\left(\frac{1}{T_S}\right) + \frac{b_1}{y_{cbz}} + b_2 \qquad 24$$

Where y_{CBZ} is the solvent free mole fraction, A is the slope, T_s is the saturation temperature b_1 and b_2 are constants. Equation 24 now can be used to fit all the CBZ-INA clear point temperature data. Then, a single set of fitting parameters that describe the CBZ-INA solubility as a function of temperature and stoichiometry is obtained.

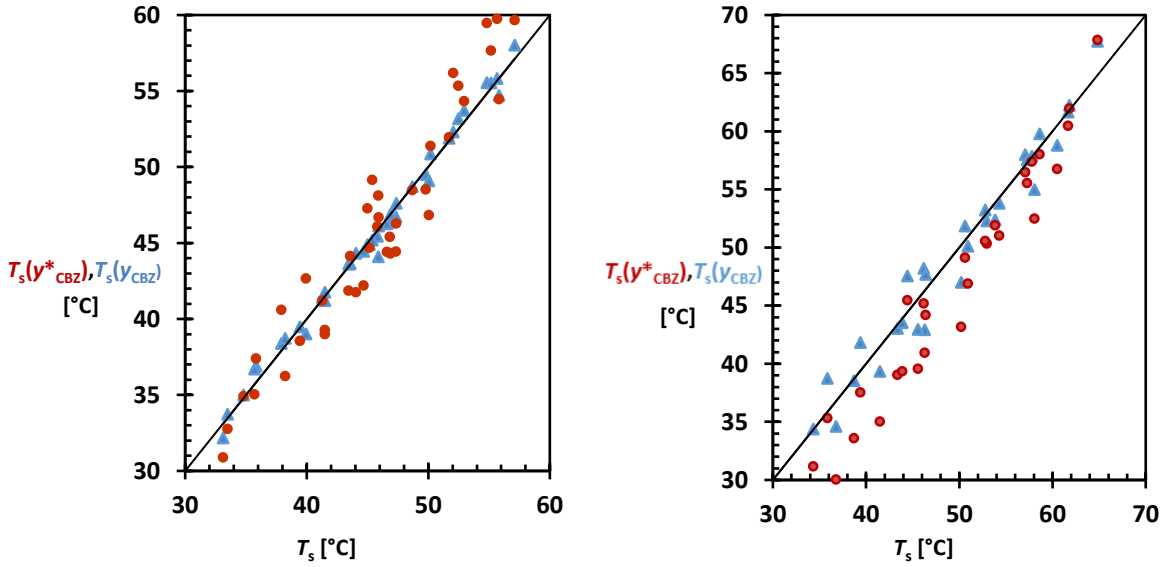

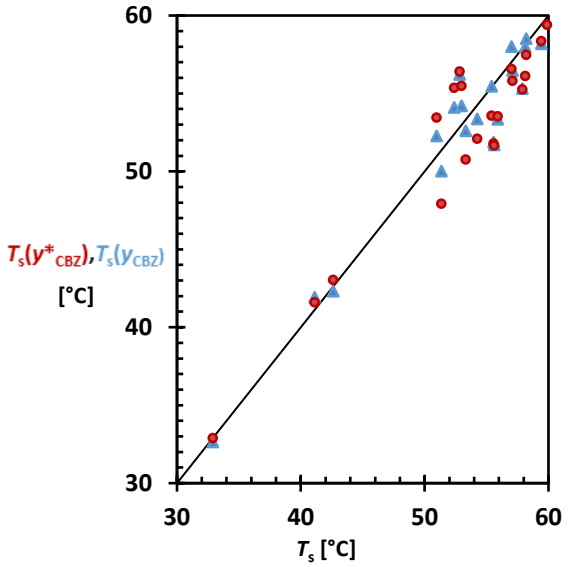

Figure 15. The fitted saturation temperatures $T_s(y^*_{CBZ})$ red ○ and $T_s(y_{CBZ})$ blue Δ as a function of the measured T_s showing the improved fit when accounting for the solution stoichiometry using equation 24.

The model fit with solution stoichiometry gives a better agreement with the experimental data than that without stoichiometry. For the ethanol system, the R^2 value increased from 0.922 to 0.991. In nitromethane and dioxane, R^2 increased from 0.959 to 0.966 and from 0.911 to 0.938, respectively.

Table 3 shows parameters determined from the collective van't Hoff plot of co-crystal solubility product at different stoichiometries and solubility of pure components in three solvents. The constant b_1 is related to the stoichiometry so not available for the pure component parameters and b_2 is related to the intercept so available for both pure components and the co-crystals. The constant b_2 is larger for the stoichiometry model in Table 3 when compared with the values without the stoichiometry in Table 2 in all solvents. However, on account of the error b_2 is similar to that obtained in Table 2 for the dioxane system. The constant b_1 is very small in the DIO system and on account of the error it is almost zero. A look at parameter A in Table 3 shows values that are higher than predicted in Table 2.

Table 3. Van't Hoff parameters for CBZ, INA and CBZ: INA co-crystal solubility with error interval for measurements in EtOH, NM and DIO. The eutectic points with stoichiometry model and non-stoichiometry model are compared.

Solvents	Solute	Parameters			Stoichiometry		No stoichiometry	
		A x 10^3	b_1	b_2	y_{CBZ} *(min)*	y_{CBZ} *(max)*	y_{CBZ} *(min)*	y_{CBZ} *(max)*
Ethanol	CBZ	-3.80±0.14	0	7.62 ± 0.04				
	INA	-2.74±0.10	0	5.92 ± 0.33				
	CBZ-INA	-7.65±1.25	0.060±0.003	15.49 ± 0.40	0.09	0.43	0.06	0.39
Nitromethane	CBZ	-5.85±0.49	0	14.59±1.53				
	INA	-4.06±0.30	0	8.55±0.938				
	CBZ-INA	-8.80±0.34	0.21±0.11	17.79±1.00	0.32	0.89	0.31	0.82
Dioxane	CBZ	-2.79±0.21	0	5.44±0.67				
	INA	-2.19±0.78	0	3.41±0.88				
	CBZ-INA	-5.52±0.38	0.11±0.10	10.11±0.94	0.33	0.68	0.38	0.68

The eutectic point stoichiometries predicted from the simple model (eq. 4) and the stoichiometry dependent model (eq. 6) are also found in table 2. It is clear that stoichiometry has an effect on the predicted eutectic points based on the difference in the y_{CBZ} (min) and y_{CBZ} (max). The solubility of the pure component is constant at a given temperature. The pure component solubility can also be a function of the other components, and the eutectic point is the point where the co-crystal solubility and the pure component solubility intersects, the only factor that can contribute to the change in eutectic point is the change in the solubility product. The new model can now be used to predict the phase diagram at various temperatures. At a given temperature, the solubility product of CBZ-INA at different stoichiometries can be calculated from equation 24 and the values in Table 3, which leads to the co-crystal solubility line at a constant temperature in the phase diagram of CBZ, INA and solvent in Figure 16.

The extent of symmetry of the phase diagram depends on the pure component solubility of the pure co-crystal components. INA is more soluble in ethanol, CBZ is more soluble in nitromethane and dioxane. Therefore, in ethanol, the phase diagram regions where co-crystal is thermodynamically stable skews towards the INA side. The CBZ: INA stoichiometry ranges from 1:1.3 at y_{CBZ} (max) = 0.43 to 1:10.3 at y_{CBZ} (min) = 0.09. In nitromethane and dioxane, the

phase diagram is skewed towards the CBZ side with CBZ: INA stoichiometry ranging from 1:0.11 at y_{CBZ} (max) = 0.89 to y_{CBZ} (min) = 0.32 and 1:0.46 at y_{CBZ} (max) = 0.68 to 1:1.90 at y_{CBZ} (min) = 0.33, respectively. The co-crystal CBZ: INA has a 1:1 stoichiometry. At a solution stoichiometry of y_{CBZ} = 0.5 pure co-crystal would only be formed in nitromethane and dioxane while a mixture of co-crystal and pure co-crystal former would be formed in ethanol according to the phase diagram in Figure 16. This further reinforces the importance of solvent choice during co-crystal screening using solution crystallization and the potential disadvantage when phase diagram construction is based on the solid form stoichiometry.

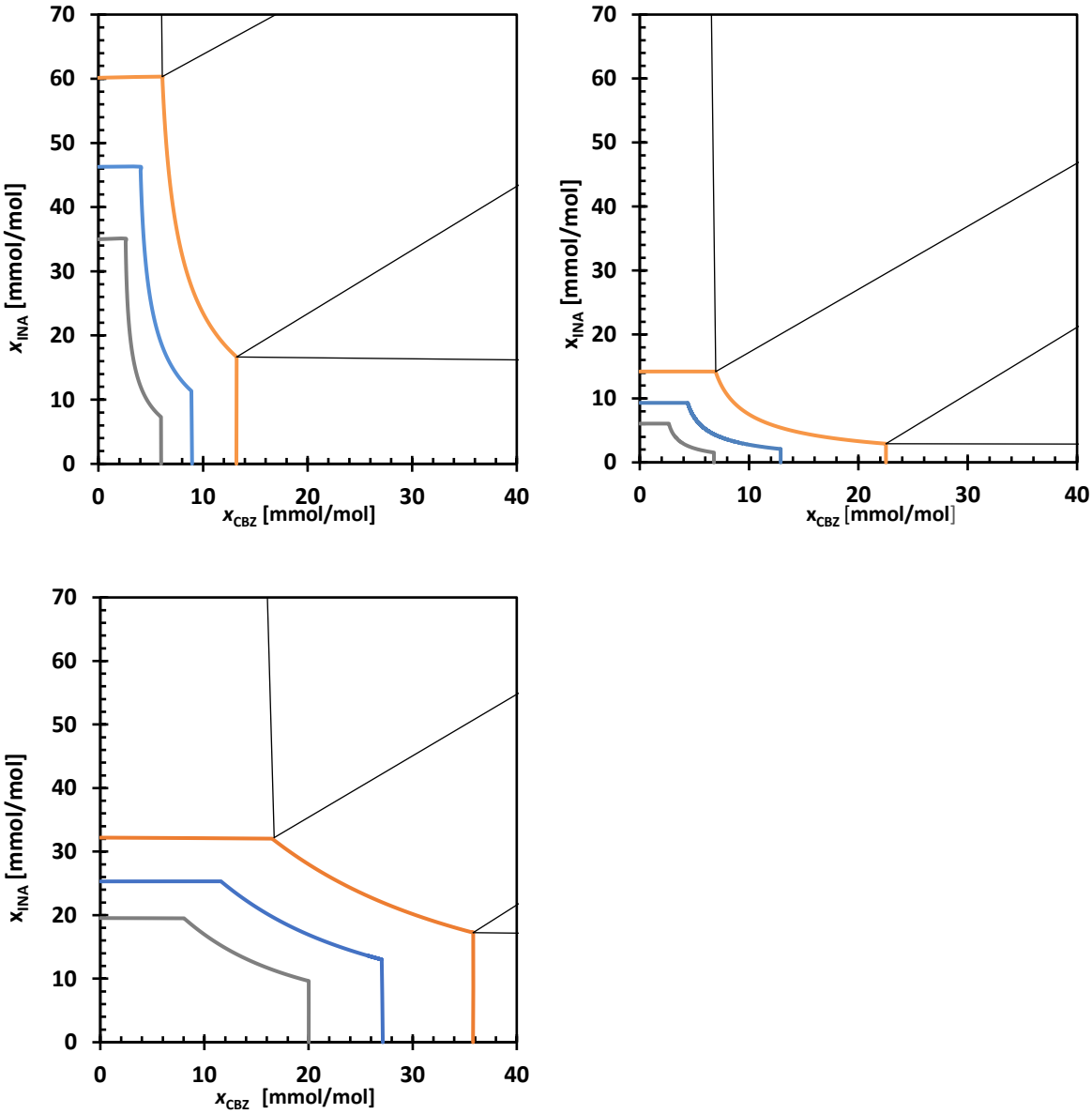

Figure 16. The phase diagram of CBZ-INA based on stoichiometry effect model in ethanol (left), nitromethane (middle) and dioxane (right) at T = 45°C (yellow), 35°C (blue) and 25°C (grey). The curved part of the lines is the solubility of the co-crystal. The straight lines from the axes that intersect the curve line are the solubility of the pure components at that temperature. These diagrams are constructed under the assumption that the solubility of the pure component is unaffected by the presence of the other co-crystal formers.

3.3.4 PXRD of co-crystallization

The solid form outcome of crystallisation in the co-crystal region was characterised at specific solution stoichiometries as shown in Figure 17. The polymorphic form obtained from co-

crystallisation in the co-crystal region after filtration and drying of the solid form produced a reproducible stable polymorphic form confirmed by PXRD. Figure 17 shows a representative pattern for crystallizations for different stoichiometries between y_{CBZ} (min) and y_{CBZ} (max) in all the three solvents. The stable form of CBZ-INA was obtained in all cases.

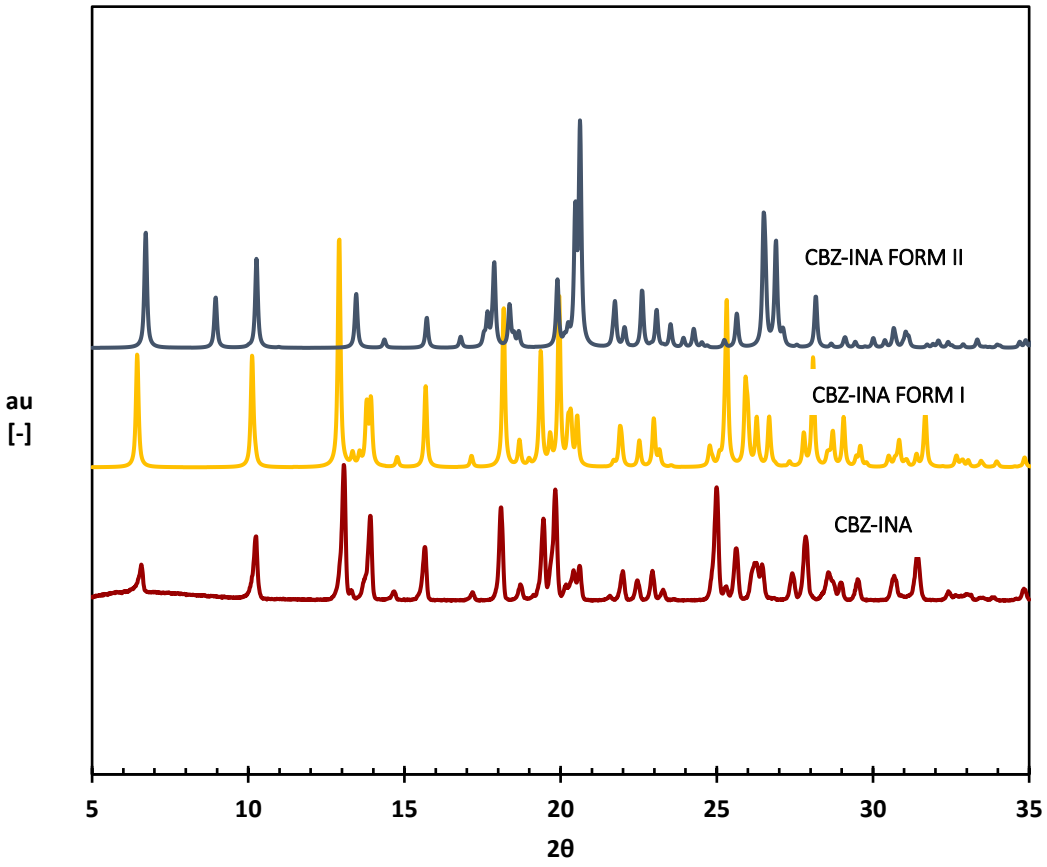

Figure 17. PXRD patterns from top to bottom form II (metastable), Form I (stable), stable CBZ: INA co-crystals pattern obtained from a particular experiment which is representative of those obtained for other experiments.

3.3.5 Solution Composition at the Eutectic Points

In the previous section, the solution stoichiometry effect on the co-crystal solubility product and the predicted eutectic points designated by y_{CBZ} (min) and y_{CBZ} (max) was described. In both cases, it was assumed that the solubility of the pure component is not influenced by the presence of the other. Here, this assumption is checked by determining the eutectic points

experimentally. One way to do this is to equilibrate a suspension with an overall composition in the estimated triphasic region (region II and IV) based on the predicted eutectic point y_{CBZ} (min) and y_{CBZ} (max) with stoichiometric effect and analyse the filtered solution using ^{1}H-NMR to determine the solution stoichiometry y^{E}_{CBZ} at eutectic equilibrium with the help of the calibration in Figure 10.

Figure 18 shows the phase diagram at 35°C for CBZ, INA and solvents ethanol, nitromethane and dioxane respectively. The phase diagram of the co-crystal and pure components at 35°C is divided into 5 regions. The overall compositions used for eutectic equilibration at 35 °C are indicated with red and green lozenges. The solution composition then should be equal to the eutectic solution composition. The intersection of the experimentally determined y^{E}_{CBZ} and the co-crystal solubility line in the phase diagram then gives an estimate of the eutectic solution composition. For example, in the nitromethane system, the solubility product of the co-crystal is then extended to intersect with the solubility of the pure component in the presence of the other components. At these points, the solution stoichiometry y^{E}_{CBZ} can be divided into two, $y^{E}_{CBZ1} = 0.33$ and $y^{E}_{CBZ2} = 0.90$, corresponding to overall compositions of red and green lozenges respectively. The eutectic point composition comprises of the co-crystal and one pure component for both y^{E}_{CBZ1} and y^{E}_{CBZ2} as shown in Table 5.

To accurately determine the eutectic point, the overall composition must be in regions II and IV of the phase diagram so that equilibrium establishes between the two solids and the solution. This is true for the nitromethane system. However, for the ethanol system the effect of the other component on the pure component solubility is substantial, shifting the eutectic point in such a way that the used overall compositional point for eutectic equilibration lies outside the target region when compared to eutectic points derived with the assumption that the solubility of the pure component does not affect the other. Therefore y^{E}_{CBZ1} = 0.06 and y^{E}_{CBZ2} = 0.60 corresponding to overall compositions of red and green lozenges respectively in ethanol

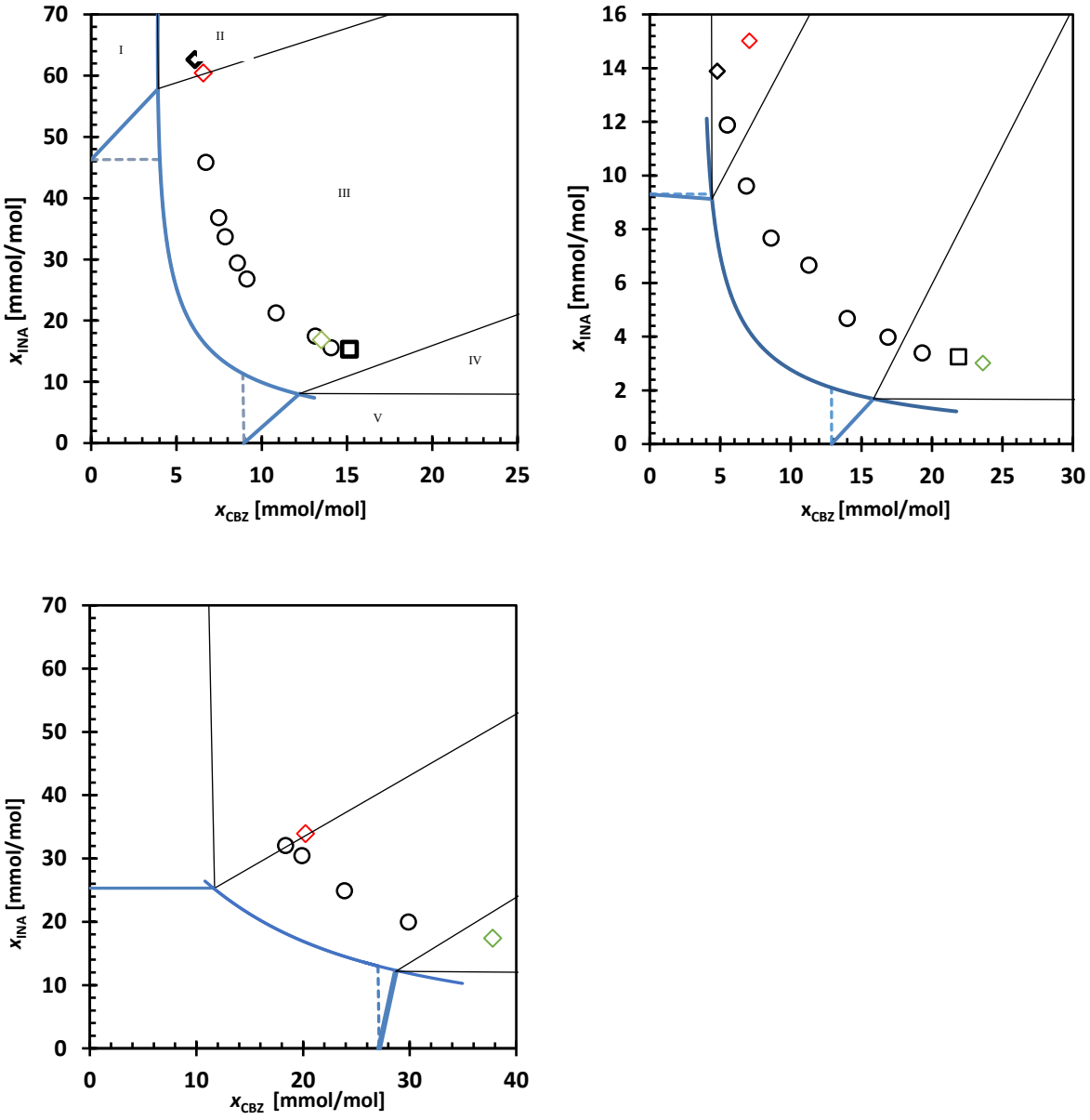

Figure 18. Phase diagram of CBZ-INA in ethanol (left), nitromethane (right) and dioxane at T = 35°C. The curved blue line is the co-crystal solubility which bounds the co-crystal region III. INA is in equilibrium with solvent in region I. CBZ is in equilibrium with solvent in region V. Mixture of co-crystal and pure components are in equilibrium in region II and IV for CBZ and INA respectively. The symbols represent the crystallization outcome of a cooling crystallization experiment of a solution with saturation temperature of 45 ° C, and overall composition (red and green ◊) indicated by the position in the phase diagram which is cooled down to 35°C. ○ – co-crystal; ◊ - INA, □ - CBZ. The dashed blue line is the solubility of the co-crystal former without the effect of the other co-crystal former on its solubility. The solid blue line from the axes is the solubility of co-crystal formers if the presence of the co-crystal formers affects each other this is the more accurate case, compared to the dashed line — the point where these two intercepts are the eutectic point. Eutectic points were not determined in EtOH and DIO systems because the overall compositions are not in regions II or IV.

Thus, there is a strong influence of one component on the solubility of the other pure component in ethanol while this is less in the other solvents. The eutectic solution stoichiometry $y^E_{CBZ} \leq y_{CBZ}$ min in nitromethane suggests that the solubility of INA decreases within measurement error in the presence of CBZ while new $y^E_{CBZ} > y_{CBZ}$ (max) suggests that the solubility of CBZ increases by 2.98 mmol/mol in the presence of INA at 35°C.

Table 4 compares the difference in solution composition with the assumption that no one component affects the solubility of the other and when it does.

Solvent	no one component effect on solubility		one component effect on solubility	
	y^E_{CBZ1}	y^E_{CBZ2}	y^E_{CBZ2}	y^E_{CBZ2}
Ethanol	0.09	0.43	0.06	0.60
Nitromethane	0.32	0.89	0.33	0.90
Dioxane	0.33	0.68	0.33	0.70

3.3.5.1 PXRD of the eutectic solid form

Table 5 shows the summary of the solid analysis outcome of the eutectic equilibrium experiments recovered from the acrosdisk filter. For each solid material analysed, there is a pure component and co-crystal present. The presence of two components indicates that the overall composition used was in the triphasic region. The co-crystal form II is present in the equilibrated samples in ethanol and nitromethane. Form II is metastable and assumed to have a higher solubility, so co-crystal solubility line would be higher in the phase diagram, and the eutectic point would be influenced. This could explain the possible shifts in y_{CBZ} (max) to y^E_{CBZ} for these cases. The differences y_{CBZ} (min) y_{CBZ} (max) to y^E_{CBZ}

Equilibrated samples are expected to contain the stable forms of the co-crystal and the pure components at the equilibrium. Since the samples were crystallised and then equilibrated it

could be that the appearance of the metastable forms is influenced by the composition in the triphasic region as demonstrated by p-Toluenesulfonamide/Triphenylphosphine Oxide co-crystal[17]

Table 5. Polymorphic form obtained from PXRD of Solution composition in the eutectics.

Solvent	y^{E}_{CBZ}		y^{E}_{CBZ}	
	Pure component INA Form	Co-crystal Form	Pure component CBZ Form	Co-crystal Form
Ethanol	I	I	IV	II
Nitromethane	II	I	III	II
Dioxane	III&I	I	III	I

3.4 Discussion

An efficient and sound method that leads to the fast estimation of the co-crystal phase diagram is one of the challenges in the co-crystallization study for process optimisation in pharmaceutical industry. The method developed here relies on a small number of clear point measurements and the workflow for the construction of the phase diagram in Figure 19 shows a detailed flow of the processes involved.

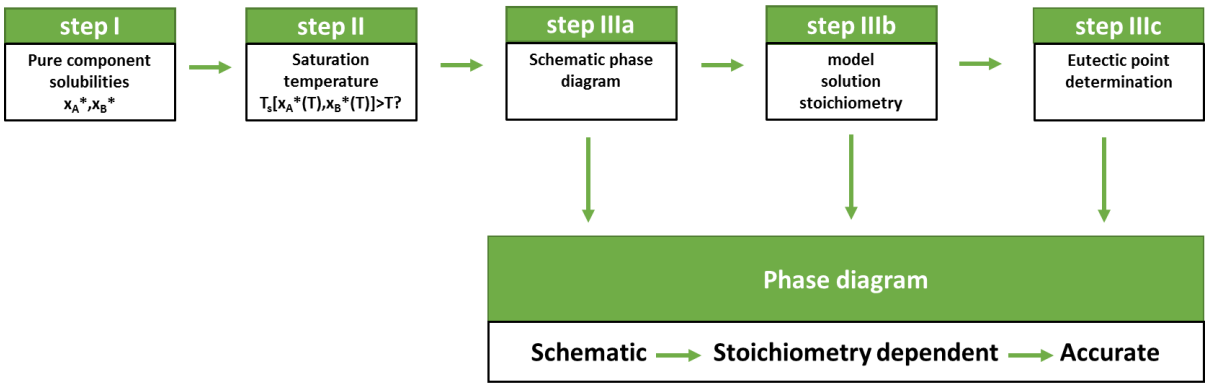

Figure 19. Workflow for phase diagram construction

It is shown that the former effect was captured in the experimental measurements and confirmed through PXRD. After the phase diagram prediction, the screening of different solution stoichiometries within the predicted co-crystal region ensures more data is available for modelling thereby increasing the robustness of the model. However more data point may be needed to capture the stoichiometric effect when this method is applied on another co-crystal system.

The symmetry of the co-crystal region is dependent on the relative solubility of the pure components in solvent. It is expected that the phase diagram would skew towards the most soluble component to produce the incongruent phase diagram as observed in all solvents. The phase diagram in ethanol skewed towards isonicotinamide, while the phase diagram in nitromethane and dioxane skewed towards carbamazepine. Until now, no work has been done to determine the phase diagram of a polymorphic co-crystal system in different solvents by using a systematic approach to determining the co-crystal phase diagram. The use of model based on empirical measurements of the co-crystal clear points provides phase diagram at multiple temperature points.

3.5 Conclusion

Through a systematic approach, we have demonstrated that co-crystal phase diagrams can be constructed using a few clear point measurements. The pure component solubility is used to design clear point measurements in the co-crystal region that result in the temperature dependent co-crystal solubility product. This solubility product, together with the pure component solubilities results in an estimate of the compositional range of the co-crystal region in the phase diagram. This first step assumes that one component does not influence the solubility of the other one and it ignores stoichiometric effects on the co-crystal solubility product. We further show that these stoichiometric effects can influence the co-crystal region

and solubility product. In order to capture this effect, a much larger number of experiments have to be performed. The symmetry of the co-crystal region in the phase diagram is dependent on the solubility of the pure components but independent on the solution stoichiometry of the co-crystal formers since the effect of stoichiometry was observed in other solvent systems apart from 1,4 - dioxane. Determination of eutectic points in a polymorphic co-crystal system is also demonstrated.

3.6 References

1. Brittain, H.G. Cocrystal Systems of Pharmaceutical Interest : 2011. Cryst Growth Des. 2012;12:1046 − 1054.

2. Qiao, N., Li, M., Schlindwein, W., Malek, N., Davies, A., Trappitt, G. Pharmaceutical cocrystals: An overview. Vol. 419, International Journal of Pharmaceutics. 2011. p. 1–11.

3. Grothe, E., Meekes, H., Vlieg, E., Ter Horst, J.H., De Gelder, R. Solvates, Salts, and Cocrystals: A Proposal for a Feasible Classification System. Cryst Growth Des. 2016;16(6):3237–43.

4. Aitipamula, S., Banerjee, R., Bansal, A.K., Biradha, K., Cheney, M.L., Choudhury, A.R., et al. Polymorphs, salts, and cocrystals: What's in a name? Vol. 12, Crystal Growth and Design. 2012. p. 2147–52.

5. Thakuria, R., Delori, A., Jones, W., Lipert, M.P., Roy, L., Rodríguez-Hornedo, N. Pharmaceutical cocrystals and poorly soluble drugs. Vol. 453, International Journal of Pharmaceutics. 2013. p. 101–25.

6. Trask, A. V, Motherwell, W.D.S., William, J. Physical stability enhancement of theophylline via cocrystallization. Int J Pharm. 2006;320:114–23.

7. Urbanus, J., Mark Roelands, C.P., Verdoes, D., Jansens, P.J., Ter Horst, J.H. Co-crystallization as a separation technology: Controlling product concentrations by co-crystals. Cryst Growth Des. 2010;10(3):1171–9.

8. Ter Horst, J.H., Deij, M.A., Cains, P.W. Discovering New Co-Crystals. Cryst Growth Des. 2009;9(3):1531–7.

9. Yu, Z.Q., Chow, P.S., Tan, R.B.H. Operating regions in cooling cocrystallization of

caffeine and glutaric acid in acetonitrile. Cryst Growth Des. 2010;10(5):2383–7.

10. Leyssens, T., Ter Horst, J.H. Solution co-crystallisation and its applications. In: Tiekink R T E, Julio Z-S, editors. Multi-Component Crystals: Synthesis, Concepts, Function. Walter de Gruyter; 2017. p. 205–36.

11. Ter Horst, J.H., Cains, P.W. Co-crystal polymorphs from a solvent-mediated transformation. Cryst Growth Des. 2008;8(7):2537–42.

12. Chadwick, K., Davey, R., Sadiq, G., Cross, W., Pritchard, R. The utility of a ternary phase diagram in the discovery of new co-crystal forms. CrystEngComm. 2009;11(3):412–4.

13. Chiarella, R.A., Davey, R.J., Peterson, M.L. Making co-crystals - The utility of ternary phase diagrams. Cryst Growth Des. 2007;7(7):1223–6.

14. Boyd, S., Back, K., Chadwick, K., Davey, R.J., Seaton, C.C. Solubility, metastable zone width measurement and crystal growth of the 1:1 benzoic acid/isonicotinamide cocrystal in solutions of variable stoichiometry. J Pharm Sci. 2010;99(9):3779–86.

15. Mohammad, K.A., Abd Rahim, S., Abu Bakar, M.R. Kinetics and nucleation mechanism of carbamazepine–saccharin co-crystals in ethanol solution. J Therm Anal Calorim. 2017;130(3):1663–9.

16. Sun, X., Yin, Q., Ding, S., Shen, Z., Bao, Y., Gong, J., et al. Solid-liquid phase equilibrium and ternary phase diagrams of ibuprofen-nicotinamide cocrystals in ethanol and ethanol/water mixtures at (298.15 and 313.15) K. J Chem Eng Data. 2015;60(4):1166–72.

17. Croker, D.M., Davey, R.J., Rasmuson, Å.C., Seaton, C.C. Nucleation in the p - Toluenesulfonamide/Triphenylphosphine Oxide Co-crystal System. Cryst Growth Des.

2013;13:3754–62.

18. Kulkarni, S.A., McGarrity, E.S., Meekes, H., Ter Horst, J.H. Isonicotinamide self-association: The link between solvent and polymorph nucleation. Chem Commun. 2012;48(41):4983–5.

19. Wenju, L., Leping, D., Black, S., Hongyuan, W. Solubility of carbamazepine (form III) in different solvents from (275 to 343) K. J Chem Eng Data. 2008;53(9):2204–6.

20. Caridi, A., Kulkarni, S.A., Di Profio, G., Curcio, E., Ter Horst, J.H. Template-induced nucleation of isonicotinamide polymorphs. Cryst Growth Des. 2014;14(3):1135–41.

21. Li, B., Wu, Y., Zhu, J., Chen, K., Wu, B., Ji, L. Determination and correlation of solubility and mixing properties of isonicotinamide (form II) in some pure solvents. Thermochim Acta. 2016;627–629:55–60.

Chapter 4

Pharmaceutical Co-crystal Screening in Practice

Abstract

As the drive for discovering new multicomponent crystals with advanced physicochemical properties increases in both academia and pharmaceutical industry, Liquid Assisted Grinding (LAG) and solution co-crystallisation remain the two most commonly used preparation techniques for co-crystal screening. However, not all preparation techniques in a co-crystal screening campaign result in co-crystals for the same combination of active pharmaceutical ingredient (API) and co-former. This necessitates the need to determine and use optimum conditions for these co-crystal preparation techniques. Therefore, LAG and solution co-crystallisation were compared for the discovery and preparation of co-crystals of COMPOUND A against 57 co-formers. These co-formers were ranked from an *in-silico* co-former screening based on the tendency of the co-formers to form hydrogen bonds with the API. LAG produced two new solid forms with co-formers methyl gallate and Acesulfame K while the solution method based on clear point measurements produced three new solid forms using 5-nitroisoptahlic acid, tartaric acid and 3,5- dihydroxybenzoic acid. These two techniques resulted in 5 hits in total with no reported shared co-former suggesting that these two methods should be used complementary for the highest success rate. Additionally, as a follow on to expanding the workflow in chapter 3, the solution co-crystal screening procedure was integrated with a phase diagram construction of another co-crystal COMPOUND B to show the seamless transition from co-crystal screening to phase diagram construction demonstrating the application of this workflow in early stage drug discovery.

4.1 Introduction

Active Pharmaceutical Ingredient (API) form selection is the process of identifying the optimal solid form to use in the final formulation. For example, a co-crystalline material with the most desirable physicochemical properties such as enhanced solubility and stability can be selected.[1] Solid form screening is the first step in form selection and is carried out with the aim of identifying new solid forms for characterisation. The possibility of developing pharmaceutical co-crystalline materials with enhanced physicochemical properties serves as the main driver for co-crystal screening. Such co-crystal screening often involves experimental[2] and computational methods.[3][4][5]

While the importance of co-crystal discovery is generally agreed, the definition of a co-crystal is a subject of debate. However, a co-crystal can be defined as a material composed of two or more neutral molecular components[6] in a defined stoichiometric ratio (associated by non-ionic and non-covalent bonds) and solid at room temperature. Co-crystal formation can be achieved through preparation techniques such as solution crystallisation,[7] slurrying,[8] solvent evaporation,[9] neat grinding,[10] liquid-assisted grinding (LAG),[11] hot stage microscopy[12] and can occur spontaneously as in case of theophylline and nicotinamide, where relative humidity and temperature were identified as key factors for spontaneous co-crystal formation without grinding.[13] For the same combination of pharmaceutical API and co-former, not all preparation techniques will result in co-crystals. With the myriad of techniques available, the successful techniques vary from one compound to the other.[14][15] Since the number of possible techniques is large, there is a need to narrow down the range of techniques, to those most successful for screening. From the large number of potential co-formers, it is also necessary to select those most likely to produce co-crystals for screening work. One way to reduce the number while increasing the chances of forming a co-crystal is through computational approaches such as virtual screening.[3][4][5]

Liquid assisted grinding (LAG)[16][17] and solution crystallisation approaches[7] are the most commonly used techniques. High throughput screening capability for both techniques allows their use in co-crystal screening and satisfies the requirement to use the minimum amount of the active pharmaceutical ingredient. While co-crystallisation techniques have been compared in the literature,[15] there is no report that combines virtual screening with the most commonly used co-crystal screening techniques. Specifically comparing only these most commonly used techniques for solid form screening and the integration of phase diagram construction in the screening process. Therefore, the objective of this chapter is to demonstrate the effectiveness of *in-silico* method for coformer selection and compare LAG with the solution co-crystallisation techniques based in the outcome of the screening.

First, this chapter applies *in-silico* screening for co-former selection. Second, LAG and solution solid form screening techniques are compared, to determine the optimal co-crystal screening technique. Finally, the phase diagram for a co-crystal is investigated to integrate co-crystal screening and the construction of a phase diagram for an active pharmaceutical ingredient based on the workflow proposed in chapter 3.

4.2 Methods

All compounds were used as provided by AstraZeneca for co-crystal screening and phase diagram construction (Analytical standard Methanol 99.9%, 6-hydroxy-2-naphthoic acid 98% Sigma Aldrich). The APIs used in this work were AstraZeneca development compounds and as such, the names and structures of these can not be disclosed. Compound A is being investigated for use in the cardiovascular therapy area. Potential hydrogen bond donors and acceptors in this compound are pyrazole, amide and ketone functional groups. Compound B is under investigation for application in the oncology therapy area. Potential hydrogen bond donors and

acceptors for compound B are amide, ether and amine functional groups and aromatic heterocyclic nitrogen.

4.2.1 *In-silico* screening

The *in-silico* co-crystal screening providing the initial list of co-formers for experimental screening was performed in-house at AstraZeneca using COSMO-RS. This virtual screening is based on a universal theory developed by Andreas Klamt[18] to predict the thermodynamic equilibrium properties of liquids, based on the statistical physics of interacting molecular surface segments.[18] This fluid-phase thermodynamics model makes it possible to compute a virtually supercooled liquid mixture of the co-crystallisation components and obtain the excess enthalpy (H_{ex}) of stoichiometric m: n mixtures created out of the pure components A and B:

$$H_{ex} = H_{AB} - x_m H_{pure},A - x_n H_{pure},B \qquad 25$$

Where H_{pure} and H_{AB} represent the molar enthalpies in the pure reference state, H_{ex} represents the total enthalpy contribution. x_m and x_n represents the mole fractions. This molecular model takes into account surface site interaction points. These points are interpreted as the interactions between functional groups to calculate parameter that aid in the ranking of co-formers but not limited to the H-bonds interactions. Compounds with $H_{ex} < 0$ have strong interaction and prefer the mixture enthalpy over their pure components. It is assumed that the supercooled liquid phase mimics the co-crystal amorphous solid state.

4.2.2 Liquid assisted co-crystal screening

Samples of 1:1 and 1:2 molar stoichiometry of Compound A and the selected co-formers were prepared in HPLC vials by weighing the mass of API and co-former. The prescribed mass of

API for the 1:1 stoichiometry was 20 mg API while that for 1:2 was 10mg. It is worth noting here that the 1:2 API co-former stoichiometry was used instead of 2:1. This is because in many of the LAG experiments, the API PXRD patterns dominate the combined powder patterns which made it difficult to see peaks of the co-former in some instances. In addition, this change in stoichiometry helps explore another stoichiometry to increase the chances of forming a co-crystal. A stainless-steel ball of 3mm diameter and 10µl of heptane were added to each vial. The mixture was allowed to grind for 70 minutes at 350rpm using the Pulverisette 6, a planetary ball mill for small scale screening, after which time the samples were characterised by PXRD.

4.2.3 Solution co-crystal screening

4.2.3.1 Solubility determination of pure components

The solubility of the pure components, compound A and co-former, was determined using the Crystal16 (Technobis). The solubility of compound A was determined in a mixture of IPA and water at various compositions. A Composition of 70:30% by volume of IPA and water mixture was selected because it is the optimum solvent composition determined for the best solubility of compound A at any given temperature. This composition is also important for process productivity by reducing the volume of solvent needed. For this reason, the same solvent composition was used for the co-formers. A prepared suspension of co-former was heated at 0.3°Cmin^{-1} from room temperature to 55°C. The clear point or saturation temperature T_s was determined during this heating stage when the suspension becomes clear and the transmission of light is 100%. All the saturation temperature of the co-formers are determined this way. A prepared suspension of compound A was heated at 0.07°Cmin^{-1} to 80°C by AZ scientists. The clear point or saturation temperature T_s was determined during this heating stage when the suspension becomes clear and the transmission of light is 100%. The heating rate of 0.07°Cmin^{-1} was used in practice as part of the procedure at AZ for compound A only and 0.3°Cmin^{-1} was

used for method consistency and to save time. The heating rate was chosen sufficiently low to assume that the determined clear point temperature is equal to the saturation temperature.

4.2.3.2 Solubility determination of compound A and co-former mixtures

A suspension of API and co-former mixture was suspended in 70:30% volume IPA and water mixture. The suspension was heated at 0.3°Cmin^{-1} to 55°C. The clear point temperature was determined during this heating stage.

4.2.4 Characterisation of solid form outcome from co-crystal screening

Solid samples from LAG screening and suspension samples from solution co-crystal screening were analysed by PXRD using the Bruker D8 Endeavour diffractometer. Samples were prepared on silicon wafers. The method for analysis was 'default scan' with parameters 2θ range 2 - 40° and the step size was 0.021°. The instrument was run in locked-coupled mode using Cu Kα radiation. Samples were run under ambient conditions (approx. 20°C).

4.3 Solubility determination of Compound B

The solubility of the pure compound B and co-former was determined using the Crystal16 (Technobis). A suspension of the pure components sample was ramped from room temperature to 55°C at 0.3°Cmin^{-1} in methanol. The solution was held at 55°C for 30minutes to ensure all of the solutes was dissolved. The solution was cooled to 5°C until nucleation occurred. The temperature profile was duplicated to obtain solubility for both the pure co-crystal and pure co-former respectively. The mixed component solubility of the co-crystal and the co-former was determined by using the same temperature profile with the temperature ramped to 60°C to allow for possible increases in temperature when co-crystal and pure coformer are mixed and also to differentiate each experiment due to similarities in parameters.

4.4 Results

This section describes the results of the *in-silico* screening, experimental screening and phase diagram construction for the two APIs.

4.4.1 Solid form screening

4.4.1.1 In-silico screening

In-silico screening is used to rank the co-formers in the order of their tendency to interact with compound A and increase the chances of forming a co-crystal in experimental work. The co-formers were selected from the 'GRAS List' (Generally Regarded As Safe for human consumption) to avoid the need for further toxicological studies for the successful co-formers. Due to the high number of these chemicals, an attempt to screen them all experimentally would be time and resource consuming.

Excess enthalpy H_{ex} could be described as the tendency of the two components to associate in the mixture prior to co-crystallisation. H_{ex} contains all enthalpic contributions as a result of discrete interactions in co-crystal former mixtures and is not limited to H-bonding interactions. Enthalpies H_{ex} are calculated and presented in kcal/mol. The use of this parameter was observed by Klamant et al[18] that the probability of forming a co-crystal increases when H_{ex} is less than zero. This chance increased further the farther away from zero H_{ex} is. Over 300 co-formers are ranked in this way and the first 57 are taken further for LAG and solution co-crystal screening because of experimental time constraints. Table 6 shows these highest ranked co-formers in order of excess enthalpy. The mass of the potential co-crystal components to be used in liquid assisted grinding experiments are also shown. Some co-formers on the list were excluded from both LAG and solution co-crystal solid form screening reducing the number of co-formers for experimental screening to 50. For instance, 1, 5-napthelene disulfonic acid (**2**) is removed because of previously identified salt formation, p-cresol (**56**) and o-cresol (**34**) were removed

for organoleptic reasons (characteristic unpleasant smell), p-vinyl phenol (**35**) and N, N-dimethylpiperazine (**36**) were removed for safety reasons. Ethanesulfonic acid (**41**) is a liquid form at ambient conditions and was eliminated to avoid co-crystallisation mediated by this liquid phase,[17] phenol was removed because it is too hygroscopic for accurate transfer into HPLC vials for the grinding procedure. The removed co-formers are highlighted on the list. The remaining co-formers on the list were used for solid form screening. In this way, the *in-silico* screening was used as a tool to guide the co-crystal screening. This serves as a systematic approach to decide the order in which the co-formers are screened.

Table 6. List of co-formers used in liquid assisted screening and solution co-crystal screening arranged in the order of predicted tendency to form non-covalent intermolecular bonds with the API. Co-formers in red were removed from screening for reasons detailed in the text. Co-formers in orange were not available for screening. From here onwards, the co-formers will be referred to using their rank.

Rank	Co-former	Excess enthalpy H_{ex} (Kcal/mol)	Mass of API (mg)	Mass of Co-formers (mg)
1	**Etidronic acid**	-3.150	19.786	9.507
2	**1,5-Napthlene disulfonic acid**	-2.966	[-]	[-]
3	**Sulfamic acid**	-2.937	23.937	4.110
4	**Gallic acid**	-2.694	20.393	7.662
5	**Oxalic acid**	-2.676	24.274	3.965
6	**3,5-dihydroxybenzoic acid**	-2.410	20.597	6.630
7	**Quercetin**	-2.330	20.284	14.153
8	**3,4-dihydroxybenzoic acid**	-2.296	19.496	6.961
9	**1,2,3-Trihydroxybenzene**	-2.148	19.615	6.009
10	**Phloroglucinol**	-2.040	22.758	6.948
11	**Trimesic acid**	-1.934	24.535	9.440
12	**Tert-butylhydroquinone**	-1.886	20.078	7.758
13	**L -ToluoylTartaric**	-1.886	21.342	18.728
14	**Pamoic acid**	-1.836	20.438	17.804
15	**5-nitroisophthalic acid**	-1.829	25.328	9.630
16	**4-Hexylresorcinol**	-1.815	20.235	8.837
17	**2,4-dihydroxybenzoic acid**	-1.747	19.796	7.335
18	**Acesulfame K**	-1.688	19.775	9.188
19	**L-Anisoyl Tartaric**	-1.634	[-]	[-]
20	**6-hydroxy-2-naphthoic acid**	-1.632	23.587	8.854
21	**3 -hydroxybenzoic acid**	-1.630	20.063	6.780
22	**Methyl gallate**	-1.629	21.358	10.31
23	**4-hydroxybenzoic acid**	-1.571	20.046	6.148

24	**Catechol**	-1.543	20.132	4.614
25	**Fumaric acid**	-1.535	21.383	5.312
26	**Propyl gallate**	-1.523	19.901	9.475
27	**Resorcinol**	-1.519	19.927	4.955
28	**2,5-dihydroxybenzoic acid**	-1.474	19.864	7.423
29	**Gentisic acid**	-1.447	19.388	7.420
30	**Orcinol**	-1.402	19.94	6.557
31	**4-hydroxy cinnamic acid**	-1.380	20.286	7.586
32	**3,5 - Dinitrobenzoic acid**	-1.299	22.213	9.551
33	**Indole**	-1.287	19.544	5.564
34	**o-cresol**	-1.218	[-]	[-]
35	**p - vinylpehenol**	-1.182	[-]	[-]
36	**N,N-Dimethylpiperazine**	-1.178	[-]	[-]
37	**Hydroquinone**	-1.175	19.62	4.855
38	**Tartaric acid**	-1.152	19.78	6.879
39	**Isocitric acid**	-1.133	[-]	[-]
40	**O-phenylphenol**	-1.112	22.573	8.140
41	**Ethanesulfonic acid**	-1.109	[-]	[-]
42	**5-chlorosalicylic acid**	-1.109	22.070	7.816
43	**Thymol**	-1.103	20.258	6.969
44	**Skatole**	-1.097	20.313	6.268
45	**Methanesulfonic**	-1.083	19.948	6.912
46	**2,5-Xylenol**	-1.0822	19.389	5.493
47	**Citric acid**	-1.072	22.768	8.910
48	**Thiodipropionic acid**	-1.044	20.633	7.944
49	**Keto glutaric acid**	-1.032	21.341	7.042
50	**Phenol**	-1.009	[-]	[-]
51	**Octyl gallate**	-0.998	20.249	12.345
52	**piperazine**	-0.987	[-]	[-]
53	**1-hydroxy-2-naphthoic acid**	-0.977	[-]	[-]
54	**P-aminobenzoic acid**	-0.933	[-]	[-]
55	**Phenoxyacetic acid**	-0.901	20.038	7.260
56	**p-cresol**	-0.876	[-]	[-]
57	**Salicylic acid**	-0.870	20.116	7.260

4.4.1.2 Liquid assisted grinding (LAG) co-crystal screening

Generally, one of the main reasons LAG is described in the literature more than solution co-crystallisation is largely to avoid the effects of solubility equilibria and solvent competition (this refers to molecular association between the solvent and the component) that cannot be avoided during solution crystallization. This is an important factor to consider especially with

co-crystal formers with congruent solubility that is with respect to the co-crystal. This could result in either coformer or the cocrystal. However, the likelihood of one of the components crystallising increases for an incongruent solubility. Congruent solubility can be described in respect to a phase diagram when the relative solubility of the pure component is similar and the symmetry of the phase diagram regions is preserved. Incongruent solubility describes a marked difference in relative solubility of the component systems of the phase diagram to the point that one component is skewed. This is not a problem with LAG as the small amount of liquid is used for catalytic purposes to increase the molecular diffusion[17] during liquid assisted grinding.

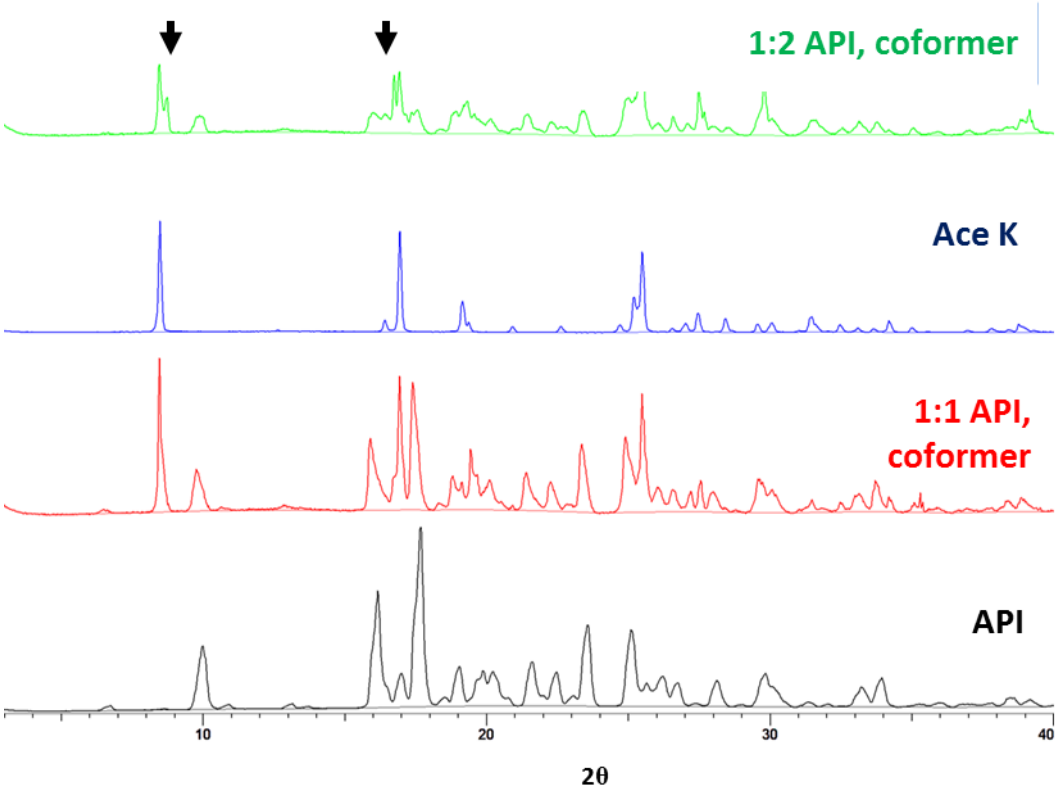

Figure 20. Powder patterns for LAG screening of Acesulfame K with API. The pure co-former (blue), API (black), 1:1 stoichiometry (red), and 1:2 stoichiometry (green). The arrows shows two new peaks at 2θ 8.8° and 18.9° not present in the API or co-former PXRD patterns.

LAG co-crystal screening produced 2 hits. A hit is defined as any powder pattern with new unassignable peaks compared to all known powder patterns of the pure components. The 2 hits were obtained using the co-formers methyl gallate (**22**) and Acesulfame K (Ace K) (**18**). Acesulfame K is an artificial sweetener used in the food industry. The powder pattern of the 1:1 LAG sample of Ace K and API produced no new distinguishable peaks as shown in Figure 20. All peaks can be assigned to the pure components. This suggests that a physical mixture of the pure components was obtained. The 1:2 sample gave a new peak at $2\theta = 8.8°$ and at $2\theta = 18.9°$ which suggests a new solid form is present in the pattern. For this reason, Ace K was concluded to be a hit.

Figure 21 shows LAG screening using methyl gallate. Methyl gallate is a methyl ester of gallic acid that can be found in tea leaves. The only new peak in the pattern of the 1:1 LAG sample of methyl gallate and API is a small peak at $2\theta = 16.5°$. This peak is more visible in 1:2 molar ratio LAG co-crystal screening. In both cases, polymorphic transformation cannot be ruled out. It is not unusual to obtain polymorphs of the pure components during co-crystal screening.[19] However, there are no reported polymorphs of the API or methyl gallate.[20] Therefore, it was concluded that the new solid form is a hit.

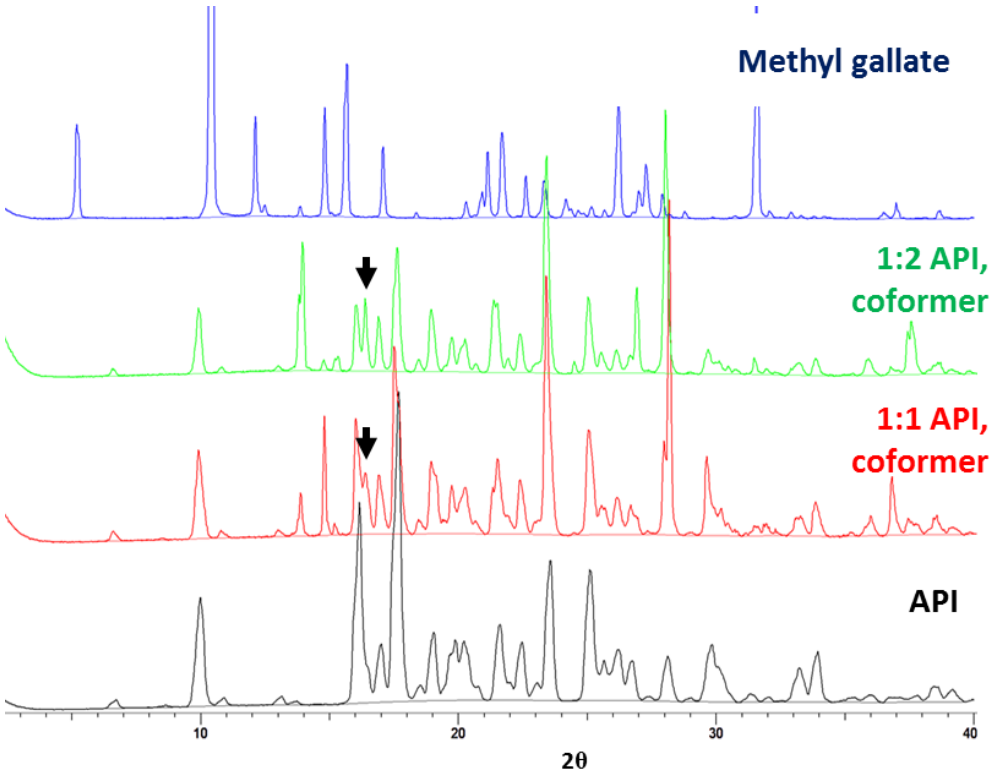

Figure 21. Powder patterns for LAG screening of methyl gallate with API. The pure co-former pattern is blue, API black, 1:1 stoichiometry (red), 1:2 stoichiometry (green). The arrow shows a new peak at 2θ 16.5° not present in the patterns of the pure components.

In both instances, for methyl gallate and Ace K, the pattern change is more distinct at the 1:2 molar ratio suggesting that the quantity of the starting material is of importance during screening and that the co-crystal could be a 1:2 solid stoichiometry ratio.

4.4.1.3 Solution co-crystal Screening

When compared to LAG, the addition of a solvent for co-crystal screening introduces an additional degree of freedom to an already complex system. However, this presents other conditions for co-crystal screening that would otherwise would not be available especially when the solubility of the co-crystal components are similar and congruent.

4.4.1.3.1 Pure API solubility

A mixed solvent ratio of 70:30% by volume of IPA and water was selected to determine the temperature dependent solubility for Compound A. Figure 22a shows the solubility of the API and the selected co-formers from the list in Table 6.The solubility of the API in 70:30% IPA: water is 18mgmL^{-1} at T = 20°C. The temperature dependent solubility of the API shows a doubling effect when T = 40°C, an estimated solubility of 32mgmL^{-1} was determined based on the best fit of all the measured solubility using van't Hoff plot.

4.4.1.3.2 Co-former solubility

Figure 22a shows the temperature dependent solubility of selected co-formers. The solubility of Acesulfame K (**18**), DL-tartaric acid (**38**), methyl gallate (**22**), 5-nitroisophthalic acid (**15**), gallic acid (**4**) and oxalic acid (**5**) was determined in 70:30% IPA and water. These co-formers were selected to see if the excess energies represented by H_{ex} is proportional to solubilities. So co-formers that occupy different positions as H_{ex} decreases in Table 6 were selected. When the solubilities of the co-formers are compared Ace K **(18)** has the lowest solubility (100 mgmL^{-1}) and 5-nitroisophtalic acid **(15)** has the highest solubility (322.9 mgmL^{-1}) at T = 40°C. Table 7 shows the estimated mass of co-former per ml of solvent.

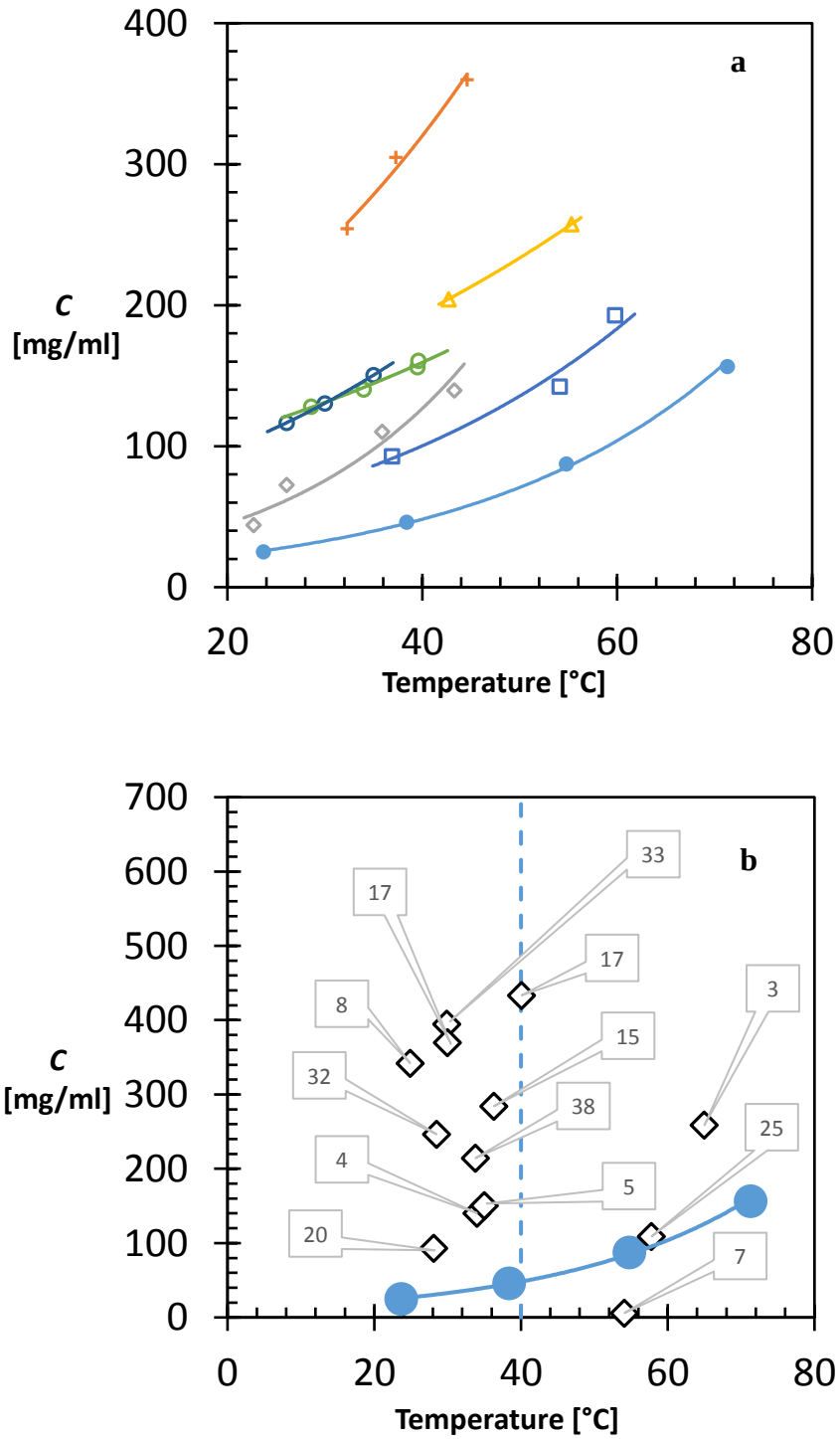

Figure 22(a). The pure component solubility of the co-formers Acesulfame K (**18**) (blue □), DL-tartaric **(38)** acid (grey ◊), methyl gallate **(22)** (yellow Δ), 5–nitroisophthalic acid **(15)** (orange +), gallic acid **(4)** (blue ○), oxalic acid **(5)** (green ○) and API (bold ○) in 70:30% IPA: water. There is no direct proportionality H_{ex} with the solubility of the selected co-formers. (**b)** The one-point solubility of the co-formers compared to the solubility of compound A. Mixed composition at a given temperature is derived from the mass of API and co-former at that saturation temperature shown by the blue line. The composition for a mixed API and co-former **17** at T = 40°C are 32 mgmL^{-1} and 433.4 mgmL^{-1}.

Table 7 shows the solubility of selected co-formers at temperatures 20 and 40°C estimated from van't Hoff plot. The solubility show a doubling effect as shown by the solubility factor.

		solubility ($mgmL^{-1}$)		Solubility factor
Rank	**Co-former**	**20°C**	**40°C**	
4	**Gallic acid**	103.0	159.2	1.5
5	**Oxalic acid**	93.2	169.1	1.8
15	**5-Nitroisophtalic acid**	152.5	322.9	2.1
18	**Acesulfame K**	54.7	100.1	1.8
22	**Methyl gallate**	108.6	192.9	1.7
38	**Tartaric acid**	45.0	126.5	2.8

It was shown that the solubility of a compound approximately doubles for every 20°C increase in temperature as suggested by Black et al.[21] Table 7 shows that this is a reasonable assumption for the selected co-formers as well. We therefore assumed that the remaining one point solubility would have the doubling effect as well. This assumption can be used to extend one point solubility measurements of the remaining co-formers to other temperatures. The solubility doubling temperature was expressed as

$$\Delta T_{sd} = \frac{0.693}{d} \qquad 26$$

Where ΔT_{sd} solubility doubling temperature and d is a constant.

Figure 22b shows a single solubility data point for each of the co-formers in comparison to the solubility of the API as a function of temperature. The solubility of some of the co-formers were removed for clarity. The one point co-former solubilities vary from $5.9 mgmL^{-1}$ at 54°C for quercetin **(7)** to 793.6 $mgmL^{-1}$ at 17.2°C for pyrogallol **(9)** Co-formers with solubilities greater than five times or five times less than that of the API were not used in solution co-crystal screening.

4.4.1.3.3 Mixed components solubility.

The co-former 2,4-dihydroxybenzoic acid **(17)** has a solubility of 433.4 mgmL^{-1} at 40°C according to experimentally determined one point solubility as shown in Figure 22b. The solubility of the API at 40°C is 32 mgmL^{-1}. The temperature at which both components are expected to dissolve in a solution with those concentrations becomes T_{ref} = 40°C. The temperature determined from the mixture of API and co-former is the saturation temperature T_s. Figure 23 shows the difference T_s - T_{ref} between the measured saturation temperature T_s of the mixed components and the reference temperature T_{ref}. A positive difference T-T_{ref} suggests the formation of a more stable solid form. A negative difference indicates that there is no co-crystal formed.

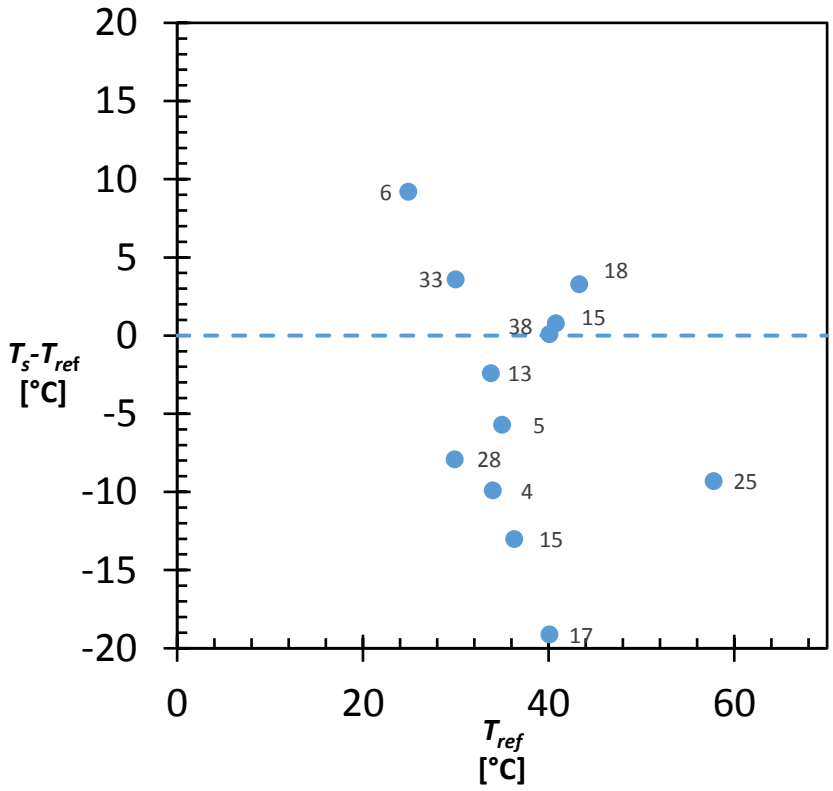

Figure 23. Difference between the expected solubility and the measured solubility based on one solubility measurements. T_s - T_{ref} plotted against T_{ref}. The positive differences suggest that the product formed is more stable than the individual components, due to its higher solubility.

The co-former 3, 5-dihydrobenzoic acid (**6**) has a temperature difference, T_s-T_{ref} of around 10°C so a new solid form is expected. The temperature difference T_s-T_{ref} is very small for co-formers **15, 18, 33, 38**.The co-former DL-tartaric acid (**38**) results in a temperature difference almost equal to zero. Other co-formers show a negative temperature differences.

4.4.1.4 Solid form characterisation

A further indication for co-crystal formation can be obtained from x-ray diffraction of the samples from the solution screening. A crystalline solid was characterised in all available samples except sulfamic acid, where the outcome is gel like solid. The PXRD patterns of the API and the co-former are manually compared to the new XRPD patterns obtained from the suspension. According to Figure 23, five new solid form patterns are expected from co-formers **6**, **15, 18, 33, 38** based on a positive difference T-T_{ref}. However, only three can be confirmed by the PXRD. These three are 3, 5 dihydroxybenzoic acid (**6**), 5-nitroisophthalic acid (**15**), DL-Tartaric acid (**38**). Co-former **18** and **33** cannot be confirmed because no nucleation occurred for the initial hold period of 5 hours at 5°C and the further hold time of 2 weeks at 4°C. Therefore, there is no solid form to characterise and the experiment could not be repeated because of material and time constraint. While methyl gallate (**22**) is of interest from LAG screening, a negative temperature difference was obtained for this co-former for the solution screening. For this reason, the solid form of the co-crystal was not characterised.

Only 3 co-formers produced new patterns that are different from all the known forms of API and the co-former. Figure 24 shows PXRD of 5-nitroisopthalic (**15**) with unassignable peaks at 2θ = 15.2, 22.5°, co-former DL-tartaric acid (**38**) has peaks at 2θ = 13.0, 19.5, 29.5, 30.5° and 3,5-dihydrobenzoic acid has peaks at 2θ = 5, 6.2, 12, 31.8°. In conclusion, solution co-crystallisation produced 3 hits. Some of the diffraction patterns for co-formers with negative temperature differences were also checked, especially for selected co-formers oxalic acid (**5**), gallic acid (**4**), 2, 4-Dihydrobenzoic acid (**17**) used to demonstrate doubling effect on solubility.

There are no new peaks because all the peaks in the patterns are assigned to either API or the co-former indicating no co-crystal formation, further validating the use of temperature difference for determining the formation of a more stable co-crystal.

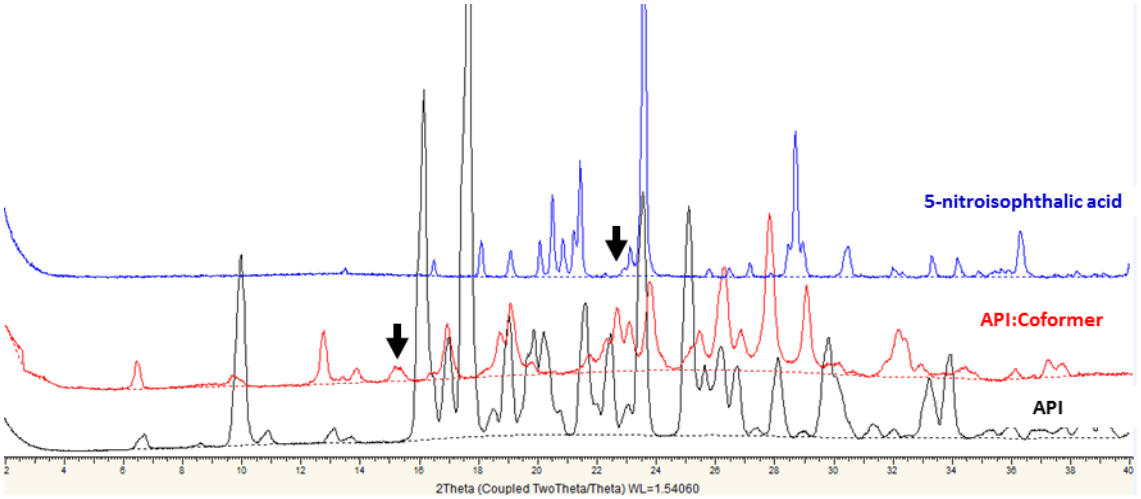

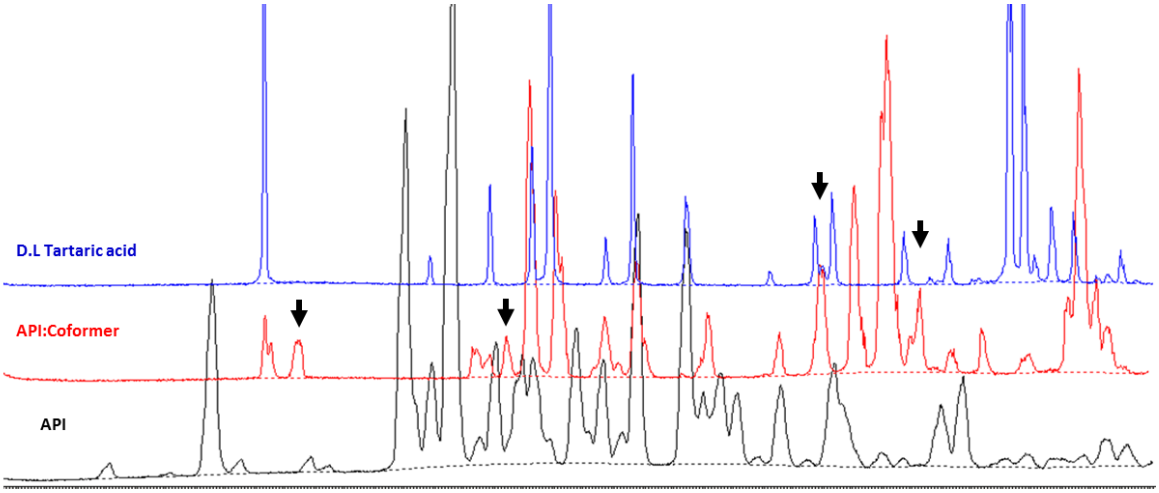

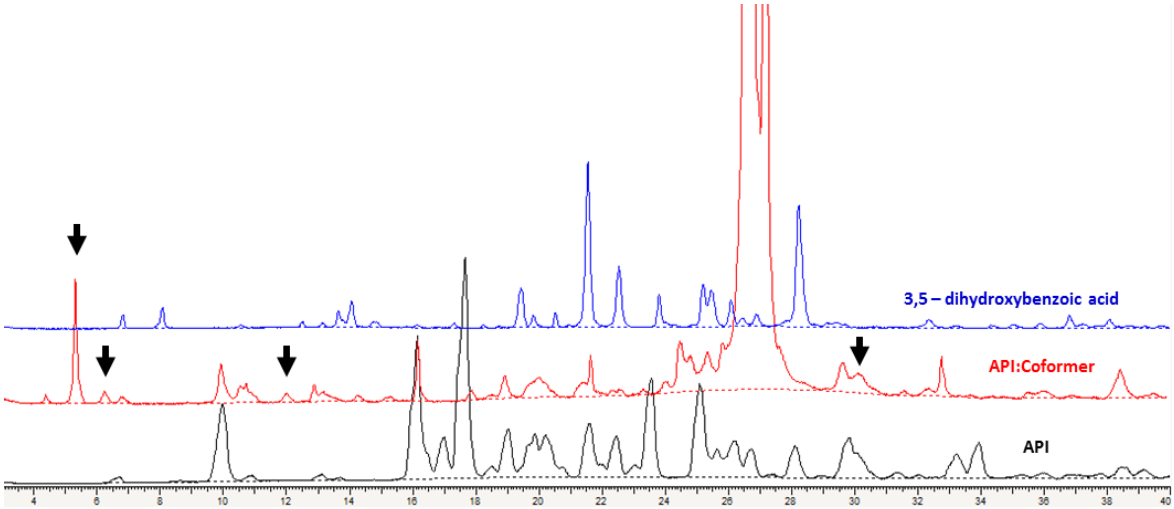

Figure 24. Powder diffraction patterns for solution screening of 5-nitroisopthalic at 2θ = 15.2, 22.5°, tartaric acid, 2θ =13.0, 19.5, 29.5, 30.5° and 3,5-dihydroxybenzoic acid 2θ = 5, 6.2, 12, 31.8°. The pure co-former pattern is blue, crystallisation outcome (red) and API (black)

The solid form screening by LAG and solution screening methods produced 5 hits: two for LAG and three for solution screening. The number of hits alone indicates that solution screening may lead to more co-crystals but does not provide a strong evidence for justifying one method over the other. However, the complementary nature of the two methods is demonstrated by the formation of different co-crystals from different co-formers. Further comparison can be made based on the amount of work, speed of result and information provided in designing a co-crystal process. The amount of work required for sample preparation for either method is similar but LAG methods is quicker in generating results from solid form characterisation within the time solubility of the components are determined. In all, both methods are reliable in generating co-crystals but information for design of cooling crystallisation is readily available through solution screening methods. Solubility phase diagram construction

Now that two methods for co-crystal screening have been compared the next step is to construct a phase diagram using the workflow described in chapter 3. The screening campaign was conducted in parallel with phase diagram construction, therefore, it was decided that a confirmed co-crystal from another work would be used for the phase diagram construction. The approach for the phase diagram differs from chapter three only in the complexity of starting materials. For example, chapter 3 starts with the pure components solubility of carbamazepine and isonicotinamide. In this chapter phase diagram construction starts with the solubility of the co-crystal (compound B) and the co-former expanding the robustness of the workflow.

Compound B is a 1:1 co-crystal of an API and 6-hydroxy-2-naphthoic acid (C). The formation of this co-crystal is an excellent example of using co-crystallisation for product separation and

purification, especially when the freebase is neither purified nor crystalline. The API that forms compound B is not crystalline and the amorphous material is not a free flowing, filterable solid.

4.4.1.5 Solubility measurements

The solubilities of the co-crystal Compound B and the pure co-former 6-hydroxy-2-naphthoic acid were determined in methanol. Since the pure API is not a crystalline solid form and challenging to transfer into the vials used for solubility determination, no solubility could be determined for the API. Figure 25 shows the temperature dependent solubility of Compound B and the co-former in methanol. The temperature dependence makes it ideal for cooling crystallisation. The solubility of the co-crystal and the co-former approximately doubles every 20°C. Compound B has a solubility of 8.78 $mgmL^{-1}$ at T = 40°C. This solubility can be expressed based on weight content of the co-former in the co-crystal so that the solubility of dissolved co-former is effectively 1.24 $mgmL^{-1}$ while the pure co-former has a much higher solubility of 199.5 $mgmL^{-1}$ at the same temperature provided that the co-crystal is stable in solution and the API does not precipitate and the co-crystal does not fall apart into a pure component co-former crystal phase. A quick confirmation of the co-crystal stability was done by suspending solids in the solvent and assessing the solid form by XRPD after filtration. The XRPD did not show the presence of any pure co-former solid and was consistent with the dry solid form of the co-crystal and no colour separation was observed.

The solubility measurements can be expressed as a van't Hoff plot by converting the solubility as a mole fraction and the temperature in kelvin (K^{-1}). The mole fraction of the co-former can be determined from equation 27 and the mole fraction of the co-crystal can be determined from equation 27.

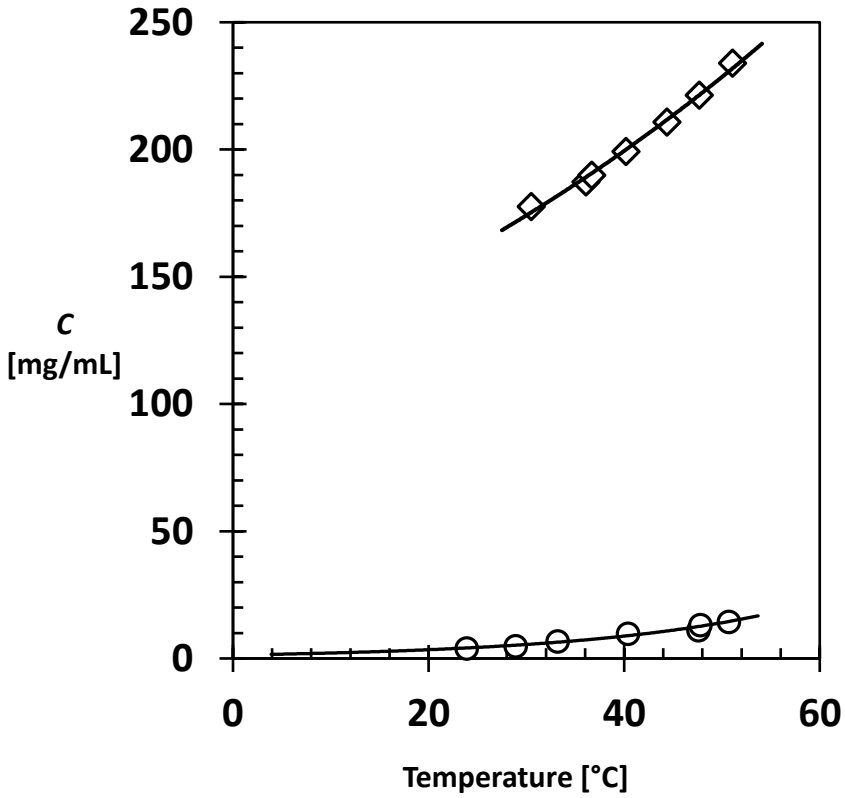

Figure 25. The solubility of the co-crystal compound B (○) and the co-former (◊) in methanol.

$$x_i = \frac{\frac{m_{cc}}{M_{w\,cc}}}{2 * \left(\frac{m_{cc}}{M_{w_{cc}}}\right) + \left(\frac{m_{MeOH}}{M_{w_{MeOH}}}\right)} \qquad 27$$

Where m_{cc} and m_{MeOH} are the mass of co-crystal and methanol respectively, $M_{w,CC}$ and $M_{w,MeOH}$ are the molecular weight of co-crystal (API and co-former C) and methanol respectively. Compound B has a 1:1 solid state stoichiometry of API and co-former C which means that the solubility product $x_{API}.x_C$ of this co-crystal can be determined. Figure 26 shows the van't Hoff plot of the co-crystal system using this solubility product. Expressing solubility in this way improves the ease of extrapolating solubility at small temperature range using van't Hoff models.

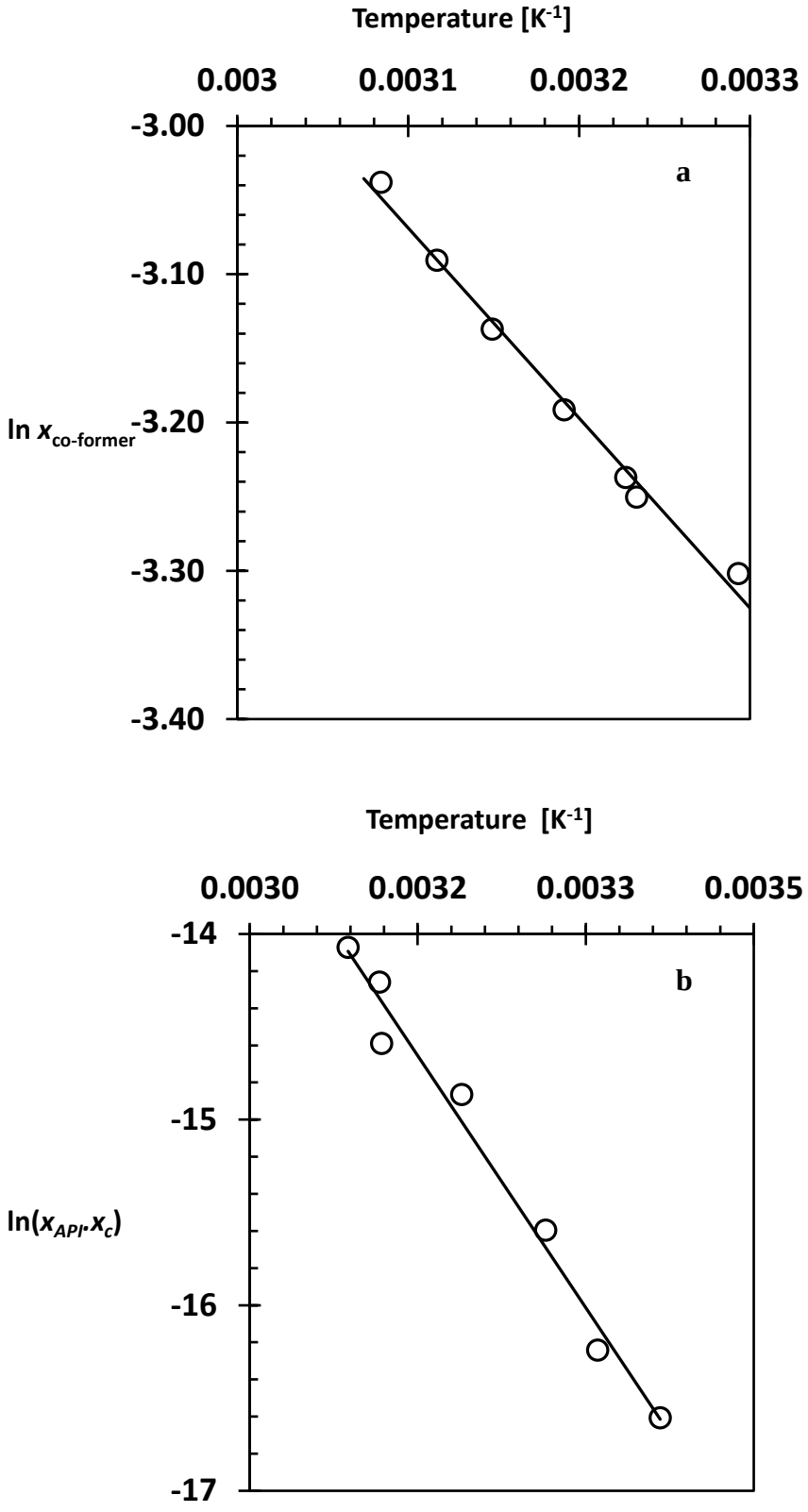

Figure 26. **Top** Van't Hoff plot of co-former solubility **Bottom.** Van't Hoff plot of co-crystal solubility product in methanol.

Equation 28 represents the model for the co-crystal that relates its solubility product with temperature. For the co-former, equation 28 can be rewritten to get equation 29

$$\ln \left(x_i x_j\right)^* = A\left(\frac{1}{T}\right) + B \qquad 28$$

$$\ln x_c = A\left(\frac{1}{T}\right) + B \qquad 29$$

Where $\left(x_i x_j\right)^*$ is the co-crystal solubility product with *i* =API, *j* = C is the solubility product, x_c is the mole fraction of co-former, and *A* and *B* are constants derived from the intercept and slope of the van't Hoff plot. *T* is the measured saturation or dissolution temperature. The constants *A* and *B* determined from the graphs in Figure 26 are given in Table 8.

Table 8. Parameters *A* and *B* determined from the van't Hoff plots of the co-crystal solubility and co-former solubility.

	A	***B***
Co-crystal	-9051 ± 55	13.86 ± 0.12
Co-former	-1282 ± 56	0.90 ± 0.18

4.4.1.6 Solubility phase diagram screening of compound B, co-former and methanol

The phase diagram screening was approached in two complementary steps. The first approach involves modelling the phase diagram based on determined parameters and the second approach involves validating this model by measuring the saturation or dissolution temperature T_s of different compositions of the co-crystals and co-formers derived from the model. A starting temperature of 20°C was selected based on the solubility of the co-crystal.

When the co-crystal dissolves in methanol to form a saturated solution, the solution stoichiometry of the API to the co-former is expected to be 1:1. Addition of excess co-former

to this system changes the API:co-former ratio in solution. This would affect the overall composition and thus reflect in the saturation temperature. The model in equation 3 and 4 with the constants in table 3 was used to predict the saturation temperature at various compositions from a reference point of 20°C for the co-crystal solubility. Saturation temperatures up to the solvent boiling point of methanol were considered.

Figure 27 shows the saturation temperature of a system of 3mg/ml of co-crystal and various amounts x_C(e) of additional co-former in methanol. There is a good agreement between the predicted saturation temperature and the measured saturation temperature as a factor of excess co-former concentration in both reference temperatures. Indicating that the model is robust for prediction. More data points were obtained for the starting point of 20°C than 30°C because saturation or dissolution temperatures higher than the boiling points of methanol were reached quicker at 30°C.

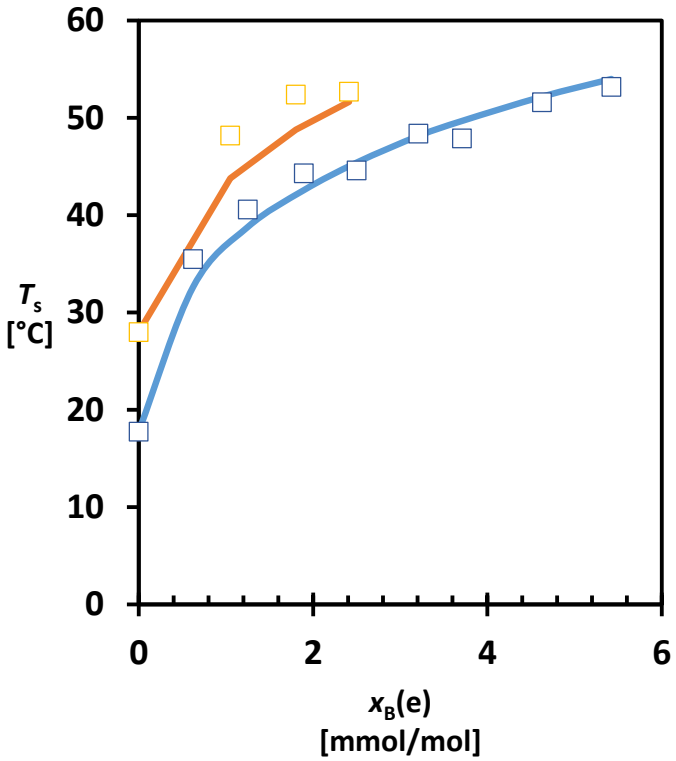

Figure 27. The clear point temperature of the co-crystal in the presence of an excess x_C(e) of co-former (excess compared to the 1:1 solution created from the dissolved co-crystal). The excess of co-former

makes the concentration x_C(e) of co-former larger in solution, so concentration product of API and co-former is higher and in order to dissolve co-crystal, the suspension has to be heated to higher *T*. Hence the clear point T_s increases for both guide temperatures 20 (blue) and 30°C (orange). In this way, less API would dissolve in solutions with an excess of co-former. Therefore, more co-crystal can be crystallised when using excess co-former.

The good agreement between the experimental and the predicted saturation temperatures makes predicting the saturation temperature of the concentration product in the presence of excess co-former using of Parameters *A* and *B* generated for the co-crystal in Table 8 more reliable. For instance, the effect of excess co-former for a particular concentration in solution on the co-crystal solubility can be expressed as a concentration product. This concentration product can be assumed to be equivalent to the solubility product for a range of temperatures. This is important for co-crystallisation process design because more co-crystalline materials can be crystallised out of the solution when using excess of co-former. This way more valuable API can be removed from solution.

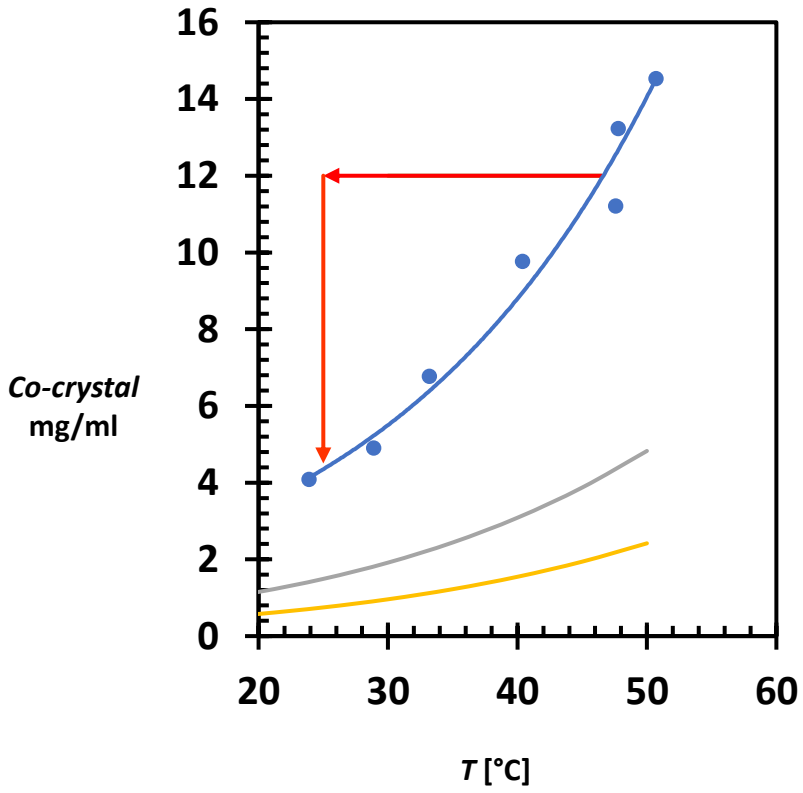

Figure 28: solubility phase diagram of the co-crystal in the presence of different concentrations of excess co-former. Solubility of co-crystal (○ blue), 5 mgmL^{-1} excess co-former (yellow) 20 mg mL^{-1} excess co-crystal (grey). A substantial increase of co-crystal material is obtained from a cooling crystallization as shown by the red lines starting from 12 mg/ml co-crystal and cooled to 25°C. Addition of excess co-former would reduce co-crystal solubility. However the amount of excess co-crystal to be added during cooling co-crystallisation should be chosen carefully.

4.5 Discussions

4.5.1 Solid form screening

4.5.1.1 Why did some co-formers form co-crystal and not others?

The characterisation and confirmation of a new crystalline solid form is generally done with multiple analytical techniques. In order to differentiate between co-crystals and other solid forms PXRD, DSC, IR spectroscopy, solid state NMR and single crystal x-ray diffraction are some of the techniques that could be used. In this work only PXRD was used because the initial

screening step focused on identifying potential hits and more detailed characterization would follow on from this. Therefore, further analytical techniques would be required to characterise the new solid forms. However, the PXRD pattern reveals peaks that are different from all known forms of the starting materials. It is known that the formation of a co-crystal requires both hydrogen bonding and close packing.[7][22] Figure 29 shows the molecular structure of the co-formers that formed co-crystals with the API.

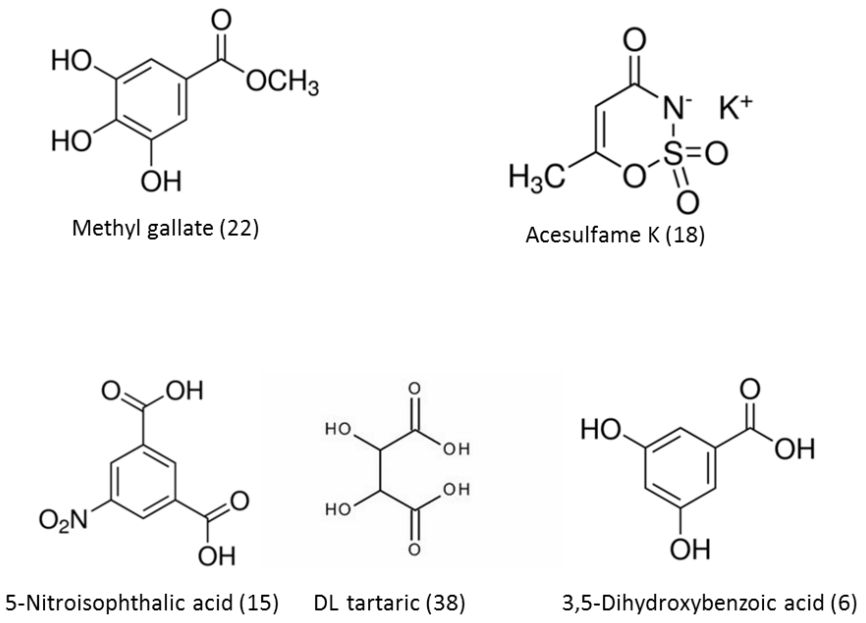

Figure 29. Molecular structure co-formers used in the screening that has peaks not positively assigned for by Compound A.

The two hits from LAG screening (API – methyl gallate and API – Acesulfame K) and three hits from solution methods (API- 5-Nitroisophthalic acid, API- Tartaric acid and API – 3,5-dihydrobenzoic acid) display a propensity to form hydrogen bonds. Compound A has amine and amide functional groups that are known to act as hydrogen bonds synthons with other functional groups like carboxylic acids and hydroxyl groups that are present in the functional groups of the successful co-formers could interact by forming hydrogen bonds but experimentally only a few of the co-formers resulted in a co-crystal. *In-silico* screening suggests

that all the co-formers can interact by forming hydrogen bonds but only a few of the co-former resulted in a co-crystal. This could be explained based on Etters rule[23][24] that states that in a crystal structure all strong H-bond acceptors or donors form hydrogen bonds after which the weaker H-bond donors and acceptors remaining after intramolecular hydrogen-bond formation form intermolecular hydrogen bonds to one another. So that the hydrogen bond interactions is stronger in co-formers that form co-crystals and the resulting interaction is energetically stable. The intermolecular interactions between Compound A and the co-formers could be too weak in some cases to drive formation of a co-crystal.

Obtaining only five co-crystals from the list of >200 co-formers of which only 57 was tested shows the specificity of co-crystal formation to the technique used and the co-former molecules used during screening.The formation of co-crystals that share the same co-former using LAG and solution screening method was not obtained in this work. This is consistent with the literature for quinhydrones where co-crystals obtained through grinding are not available in solution[14] and instances where the formation of co-crystals is duplicated for the same co-former regardless of the method used in the case of trospium chloride[15], so the inability of the two methods sharing the same co-former should not always be expected.

4.5.1.2 In-silico screening

An *in-silico* screening method was applied to select co-formers for experimental screening based on the propensity for interactions between the API and the co-former. This predictive approach resulted in a co-former ranking. It is rational to expect two outcomes from *in-silico* screening. First, co-formers with the same functional groups would be predicted in co-former clusters and second, a higher chance of co-crystal formation would be observed experimentally for the higher ranked co-formers. The first five did not give a co-crystal hit, with the exception of 1,5-Napthlene disulfonic acid which forms salt, identified in a different screening. The

potential to form co-crystals is not concentrated at the top of the list. However, the majority of the hit are in the first twenty co-formers.

Table 9 shows a series of sterically similar co-formers **15, 18, 22,** while in a cluster have different functional groups with abundance of hydroxyl moieties. The remaining two hits **6** and **38** also show less steric resemblance. This suggests that there may be other factors not considered in the virtual screening. This screening campaign suggests that the use of virtual screening as a means to reduce the number of co-formers in preparation for empirical co-crystal screening may be an effective strategy. However the use of result generated in this work for validation of *in-silico* screening may depend on various factors such as the nature of the API and how easily it can form a co-crystal, other co-formers beyond number 57 on the list may form co-crystal, the prediction method might not be very good for this API and It could depend on the experimental techniques used. A search for co-crystal is not a guarantee that one would be found, the use of very diverse techniques like LAG and solution co-crystallisation should result in a high chance of identifying a co-crystal if one exists.

Table 9. Summary of the *in-silico* screening showing greater propensity to form co-crystals in higher ranked co-formers. The different functional groups in the co-formers is identified to show similarities and difference in the functional groups available. A * depicts co-former involved in salt formation,✓ indicates the presence of the functional group and – absence of the functional group.

Rank	Co-former range	Number of hit	Functional groups				
			Aromatic	Carboxylic	Hydroxyl	Ester	Nitro
2	1-10	2	*	*	*	*	*
6			✓	✓	✓	-	-
15	11-20	2	✓	✓	-	-	✓
18			-	-	-	-	✓
22	21-30	1	✓	-	✓	✓	-
38	31-40	1	-	✓	✓	-	-
	41-50						

4.5.2 Phase diagram

The process of screening for a co-crystal using a solution method and subsequent phase diagram construction is not usually an integrated task. In both cases, the solubility determination of the pure component is a starting point which makes these activities ideal for integration. Since it was not possible to fully characterise our co-crystal hits within the timeframe of the project, an alternative compound was used to demonstrate the robustness of the workflow that is shown in Figure 30. The phase diagram in Figure 9 was terminated at step IId where experimental saturation points coincide with the model-based prediction.

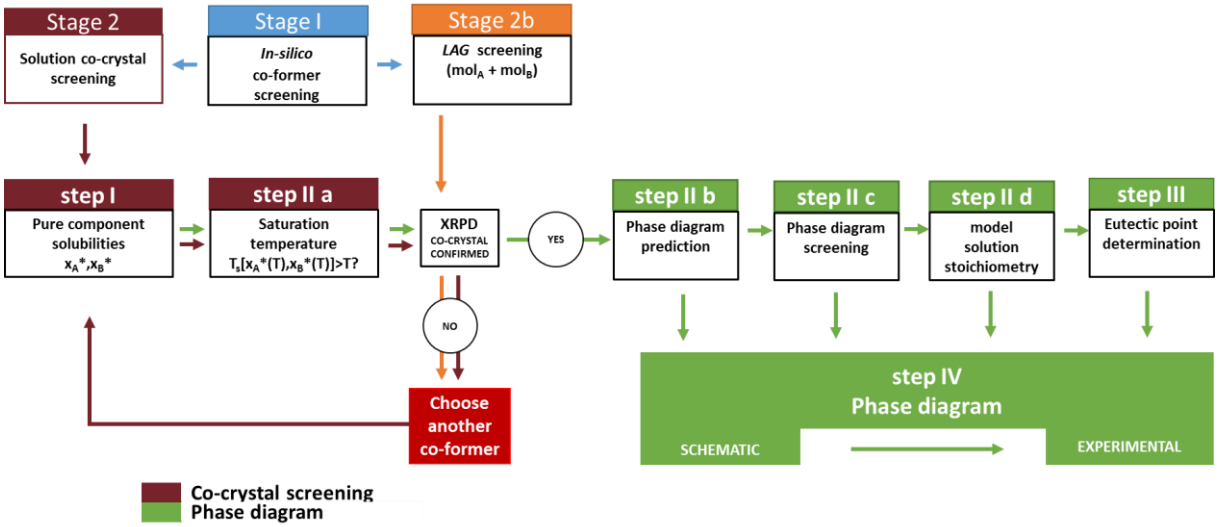

Figure 30. Workflow that combines solution screening methods with the phase diagram construction method. Burgundy linkers are for solution co-crystal screening and green linkers are for phase diagram. Details of the process in each step is in chapter three of the thesis.

The supersaturation that drives co-crystallisation can be generated from decrease in temperature. Once the co-crystal has nucleated, the formed co-crystal can consume the supersaturation. The API and coformer is then undersaturated in respect to the co-crystal

therefore neither can nucleate. One way to shift the direction of the co-crystal formation is to include excess amount of the co-former as shown in Figure 28 this would reduce the solubility of the co-crystal in methanol and ensure that all the co-crystal formed is captured.

The accuracy of this phase diagram can be affected by the low purity of the API, models and estimation of the eutectic points in the presence of the excess co-former. It is logical to assume that the co-crystal boundary would be exceeded at some point with the addition of excess co-former. Since we know that the predicted and the measured saturation temperature are in good agreement, the eutectic points based on the solubility of the co-former can be predicted. In this case, the eutectic point is the point where the predicted co-crystal solubility in the presence of excess co-former meets the solubility of the pure co-former. It is estimated that the eutectic points would be out of range of the measurable saturation temperatures in methanol. At T = 20°C the eutectic point saturation temperature (not shown) is estimated to be about 85°C. At T = 30°C the eutectic point saturation temperature (not shown) is estimated to be about 95°C.

4.5.3 Workflow

This workflow presumed a thorough solvent selection process as demonstrated in the literature[25] especially from stage two to stage four. Alternatively, a self-association method [26] can also be used. The workflow also shows that the the data collected in step 1 and IIa is needed for both screening and phase diagram measurement. It was stated that LAG can be used in tandem or parallel to the solution screening methods this is because grinding of the samples are faster and this information can help inform the screening process by helping to identify co-formers that may be of interest. This area of developing ways of integrating these two screening methods with phase diagram maybe of interest in the future.

4.6 Conclusion

Solid form screening using LAG method and solution co-crystal screening method has been compared and used to validate the use of virtual experimentation. The LAG method resulted in 2 hits with methyl gallate and Acesulfame K at different compositions and 3 hits for solution co-crystal screening. Suggesting the solution method is better than LAG contrary to literature. The use of solution co-crystal screening in this way has helped expand workflow for phase diagram construction by integration screening process with phase diagram construction and versatility of the workflow tested by using slightly different starting point of workflow.

Screening for a co-crystal is an unpredictable practice so the formation of a co-crystal cannot always be duplicated for the same co-former using different co-crystallisation methods. Virtual screening method in conjunction with other co-crystal screening method can help reduce the number of co-former used in screening and lead to an optimised approach to co-crystal discovery. Out of all the methods used solution based method is the most laborious but the only one relatively translatable to scale up.

4.7 Acknowledgement

Special thanks to Helen Wheatcroft for her invitation to AstraZeneca. Thanks for your support, discussion and advice to produce this chapter. Anna Jawor-Baczynska for supplying the solubility measurements of compound A used in this chapter. Jim Mccabe for the virtual screening of the coformers. Special thanks to Prof Joop Ter Horst for his guidance, direction and critical appraisal of this work from experimental stage, data analysis and report writing throughout this project.

4.8 References

1. Sugandha, K., Kaity, S., Mukherjee, S., Isaac, J., Ghosh, A. Solubility enhancement of ezetimibe by a cocrystal engineering technique. Cryst Growth Des. 2014;14(9):4475–86.

2. Malamatari, M., Ross, S.A., Douroumis, D., Velaga, S.P. Experimental cocrystal screening and solution based scale-up cocrystallization methods. Adv Drug Deliv Rev. 2017;117:162–77.

3. Grecu, T., Hunter, C.A., Gardiner, E.J., Mccabe, J.F. Validation of a Computational Cocrystal Prediction Tool: Comparison of Virtual and Experimental Cocrystal Screening Results. Cryst Growth Des. 2014;14:161–71.

4. Grecu, T., Adams, H., Hunter, C.A., Mccabe, J.F., Portell, A., Prohens, R. Virtual Screening Identifies New Cocrystals of Nalidixic Acid. Cryst Growth Des. 2014;14:1749−1755.

5. Taylor, C.R., Day, G.M. Evaluating the Energetic Driving Force for Cocrystal Formation. Cryst Growth Des. 2018;18:892–904.

6. Grothe, E., Meekes, H., Vlieg, E., Ter Horst, J.H., De Gelder, R. Solvates, Salts, and Cocrystals: A Proposal for a Feasible Classification System. Cryst Growth Des. 2016;16(6):3237–43.

7. Ter Horst, J.H., Deij, M.A., Cains, P.W. Discovering New Co-Crystals. Cryst Growth Des. 2009;9(3):1531–7.

8. Croker, D.M., Rasmuson, A.C. Isothermal Suspension Conversion as a Route to Cocrystal Production: One-Pot Scalable Synthesis. Isothermal Suspens Convers as a Route to Cocrystal Prod One-Pot Scalable Synth. 2014;18:941–6.

9. Basavoju, S., Boström, D., Velaga, S.P. Pharmaceutical cocrystal and salts of norfloxacin. Cryst Growth Des. 2006;6(12):2699–708.

10. Hu, Y., Gniado, K., Erxleben, A., McArdle, P. Mechanochemical reaction of sulfathiazole with carboxylic acids: Formation of a cocrystal, a salt, and coamorphous solids. Cryst Growth Des. 2014;14(2):803–13.

11. Weyna, D.R., Shattock, T., Vishweshwar, P., Zaworotko, M.J. Synthesis and Structural Characterization of Cocrystals and Pharmaceutical Cocrystals: Mechanochemistry vs Slow Evaporation from Solution. Cryst Growth Des. 2009;9(2):1106–23.

12. Berry, D.J., Seaton, C.C., Clegg, W., Harrington, R.W., Coles, S.J., Horton, P.N., et al. Applying hot-stage microscopy to co-crystal screening: a study of nicotinamide with seven active pharmaceutical ingredients- Supplementary information. Cryst Growth Des. 2008;8(5):1697–712.

13. Ervasti, T., Aaltonen, J., Ketolainen, J. Theophylline – nicotinamide cocrystal formation in physical mixture during storage. Int J Pharm. 2015;486(1–2):121–30.

14. Patil, A.O., Curtin, D.Y., Paul, I.C. Solid-State Formation of Quinhydrones from Their Components. Use of Solid-Solid Reactions To Prepare Compounds Not Accessible from Solution. J Am Chem Soc. 1984;106(2):348–53.

15. Sládková, V., Cibulková, J., Eigner, V., Šturc, A., Bohumil, K., Rohlíče, J. Application and Comparison of Cocrystallization Techniques on Trospium Chloride Cocrystals. Cryst Growth Des. 2014;14:2931–6.

16. Grecu, T., Prohens, R., Mccabe, J.F., Carrington, E.J., Wright, J.S., Hunter, C.A. Cocrystals of spironolactone and griseofulvin based on an in silico screening method. CrystEngComm. 2017;19:3592–9.

17. Friscic, T., Jones, W. Recent Advances in Understanding the Mechanism of Cocrystal Formation via Grinding. Cryst Growth Des. 2009;9(3):1621–37.

18. Abramov, Y.A., Loschen, C., Klamt, A. Rational coformer or solvent selection for pharmaceutical cocrystallization or desolvation. J Pharm Sci. 2012;101(10):3687–97.

19. Karanam, M., Dev, S., Choudhury, A.R. New Polymorphs of Fluconazole : Results from Cocrystallization Experiments. Cryst Growth Des. 2012;12:240–52.

20. Sun, C.C., Hou, H. Improving Mechanical Properties of Caffeine and Methyl Gallate Crystals by Cocrystallization. Cryst Growth Des. 2008;8(5):1575–9.

21. Black, S., Muller, F. On the Effect of Temperature on Aqueous Solubility of Organic Solids Abstract : Org Process Res Dev 2010,. 2010;14(3):661–5.

22. Issa, N., Barnett, S.A., Mohamed, S., Braun, D.E., Copley, R.C.B., Tocher, D.A., et al. CrystEngComm Screening for cocrystals of succinic acid and 4-aminobenzoic acid. CrystEngComm. 2012;14:2454–64.

23. Margaret E. Etter. Hydrogen Bonds as Design Elements in Organic Chemistry. J Phys Chem. 1991;95(8):4601–10.

24. Etter, M.C. Encoding and Decoding Hydrogen-Bond Patterns of Organic Compounds. Acc Chem Res. 1990;23(4):120–6.

25. Brown, C.J., Mcglone, T., Yerdelen, S., Srirambhatla, V., Mabbott, F., Gurung, R., et al. Enabling precision manufacturing of active pharmaceutical ingredients: workflow for seeded cooling continuous crystallisations. Mol Syst Des Eng. 2018;3(3):518–49.

26. Kulkarni, S.A., McGarrity, E.S., Meekes, H., Ter Horst, J.H. Isonicotinamide self-association: The link between solvent and polymorph nucleation. Chem Commun. 2012;48(41):4983–5.

Chapter 5

Compositional Dependent Co-crystal Nucleation

Abstract

This chapter aims to determine the compositional dependence of the solution on co-crystal nucleation. These compositions or solution stoichiometries y_{CBZ} were chosen within the co-crystal region of the phase diagram developed in chapter 3 and used to study co-crystal nucleation kinetics captured in metastable zone widths and induction times. The nucleation behaviour of carbamazepine – isonicotinamide co-crystal was determined in a number of organic solvents based on the stochastic nature of crystal nucleation in small volume that is apparent in induction time measurements. The metastable zone width showed the stochastic nature of nucleation and no dependence on stoichiometry across the solvents used. At a single stoichiometry, the nucleation rate *J* was supersaturation dependent as expected. The effect on the nucleation rate *J* of the solution stoichiometry in ethanol, nitromethane and dioxane was analysed based on classical nucleation theory, which suggests that a change in solution stoichiometry has an effect on the nucleation rate but does not always follow a proportional relationship with solution stoichiometry. Application of different analytical approaches on the induction time measurements suggests that estimated values of *A* and *B* may differ based on the chosen analytical approach and assumptions.

5.1 Introduction

The study of the nucleation process is driven by the influence of nucleation on product quality attributes and the development of new nucleation theories.[1][2] The control of product quality attributes such as purity, crystal form and morphology is vital in pharmaceutical manufacturing where other downstream processes are reliant. This makes nucleation from solution a crucial step in crystallisation process. Several attempts have been made to describe nucleation in simple organic molecules using the classical nucleation theory.[3][4][5][6][7] The use of this established theory at different conditions may lead to a new view and better understanding of nucleation process.

Understanding the nucleation of multicomponent crystals from solution requires knowledge of both phase equilibria and kinetics. The phase diagram of the compound used here has been described in details in chapter 3. The work available in the literature on nucleation in multicomponent systems is limited. Yu et al.[8] concluded that consideration of phase diagram alone is not efficient and there is a need for evaluating possible kinetic pathways in a phase diagram. Gagniere et al.[9] identified pathways for crystal nucleation by monitoring co-crystallisation of carbamazepine – nicotinamide co-crystal in ethanol using Raman probes and concluded that temperature, concentration and the polymorphic outcomes are factors that may influence the pathway in crystallisation kinetics. Boyd et al. [10] demonstrate that an excess of benzoic acid or isonicotinamide appears to increase the metastable zone width of benzoic acid – isonicotinamide co-crystal in ethanol.

Despite these insights into nucleation kinetics in co-crystals little is known about the effect of solution composition or stoichiometry on the nucleation rates of co-crystals. One way to increase understanding of the effect of solution stoichiometry on co-crystals is by measuring crystal induction time in the solution and subsequently determine the nucleation rates under

various solution stoichiometric conditions. A general method to determine the nucleation rate is the cumulative probability distribution of the induction time. This method has only been used in simple organic crystals.

This work aims to gain understanding of the effect of solution stoichiometry on the nucleation rate of carbamazepine - isonicotinamide co-crystal in different solvents by measuring induction time. First, the metastable zone of the co-crystal is determined at various solution stoichiometries and in different solvents to design conditions for induction time measurements. Secondly, induction time distributions of the co-crystal is then measured at different supersaturations for specific stoichiometries in different solvents. Finally, the nucleation rate data is analysed and interpreted.

5.2 Methods

Carbamazepine (≥98%), Isonicotinamide (99%), Ethanol (99.9%), Nitromethane (≥95%), Dioxane (99%) was obtained from Sigma Aldrich.

Metastable zone measurements and induction time measurements were performed using the Crystal16 multiple-reactor (Technobis, The Netherlands). It is designed with 16 wells to hold 16 standard HPLC glass vials with a capacity up to 1.8mL. The crystal16 measures the transmission of light through the vials in the wells, if a suspension is present in the vial, the light is blocked and transmission of light is reduced. If a clear solution is present in the vial, the light passes through the sample undisturbed which results in maximum transmission. Upon increasing the temperature of a suspension in the vials the light transmission through the samples reaches an upper limit, as the crystals dissolve in the solvent, the suspension turns into clear solution. This upper limit is the clear point temperature (T_s). When this clear solution is cooled at some temperature or moment in time, crystals will form and grow to be detectable size. The temperature where crystal is detected is the cloud point (T_c). Induction time is the time

taken for the saturated solution to fall below 100% transmitivity when held at constant temperature.

5.2.1 Metastable zone width measurement

Metastable zone width were measured for specific solution stoichiometry (y_{CBZ}) in ethanol, nitromethane and dioxane using crystal16. The solution stoichiometry y_{CBZ} is the solvent free mole faction of carbamazepine and isonicotinamide. The selected y_{CBZ} is based on compositions within the co-crystal region of the phase diagram in Chapter 3. Multiple cloud points were measured at various y_{CBZ} using sample composition with a saturation temperature of T_s = 45°C. The metastable zone width was obtained for stoichiometry y_{CBZ} = 0.07, 0.09, 1.11, 0.14, 0.17, 0.20, 0.25, 0.29, 0.32, 0.40, 0.43, 0.46 in ethanol. 0.43, 0.46, 0.53, 0.61, 0.67, 0.75, 0.80, 0.84, 0.86, 0.88 in nitromethane and 0.30, 0.36, 0.39, 0.45, 0.49, 0.51, 0.60, 0.62, 0.66 in dioxane. To obtain these solution stoichiometries, carbamazepine and isonicotinamide were weighed simultaneously into vials and 1 ml of solvent added. A magnetic stirrer with dimensions 7 x 3 mm was added and the standard cap screwed on tight. Vials were weighed before and after the experiment to make sure there was no evaporation during the temperature cycle. To determine the saturation temperature T_s and cloud point T_c respectively, the solution was heated to 55°C at 0.3°Cmin^{-1} at a stirring rate of 700 rpm. The solution was then held at 55°C for 10 minutes, tuned and cooled down to 0 - 5°C at 0.3°Cmin^{-1}. The stirring rate was maintained at 700 rpm throughout the temperature profile. Triplicate measurements were taken for each sample. The temperature difference between the co-crystal saturation temperature T_{s} and the cloud point temperature T_{c} cooled at a constant rate is the metastable zone width ($\Delta T = T_s - T_c$).[11]

5.2.2 Induction time measurements

A total of 80 induction time was measured per composition at 5 supersaturations so 16 per supersaturation. The induction time measurements were done for CBZ-INA co-crystal at y_{CBZ} = 0.129, 0.204, 0.295 in ethanol at temperature 34°C - 38°C. In nitromethane y_{CBZ} = 0.499, 0.752, 0.833 at supersaturation of 33°C - 37°C and in dioxane y_{CBZ} = 0.395, 0.505, 0.615 at supersaturation of 32°C – 36°C. Supersaturation is a function of temperature so by controlling the temperature the supersaturation can be controlled. Stock solution with a saturation temperature of T_s = 45°C was made in 20ml of solvent for each y_{CBZ}. The stock solution was left on hotplate stirred at 300 rpm for 20 – 30 minutes until the crystalline material dissolved. The solution stirring rate was then reduced to 150 rpm and 1 ml of stock solution samples was quickly transferred into 16 vials. After which a magnetic stirrer was added and the lid was screwed on tight. The vials were transferred into the crystal16 and heated to 55°C at 0.3°Cmin^{-1}, held at 55°C for 10 minutes and cooled down at 5°C min^{-1} to the target temperature or supersaturation and held there for 5 hours. The appearance of a crystalline phase was monitored by changes in transmission of light through the solution.

5.3 Results

5.3.1 Phase diagram and supersaturation ratios

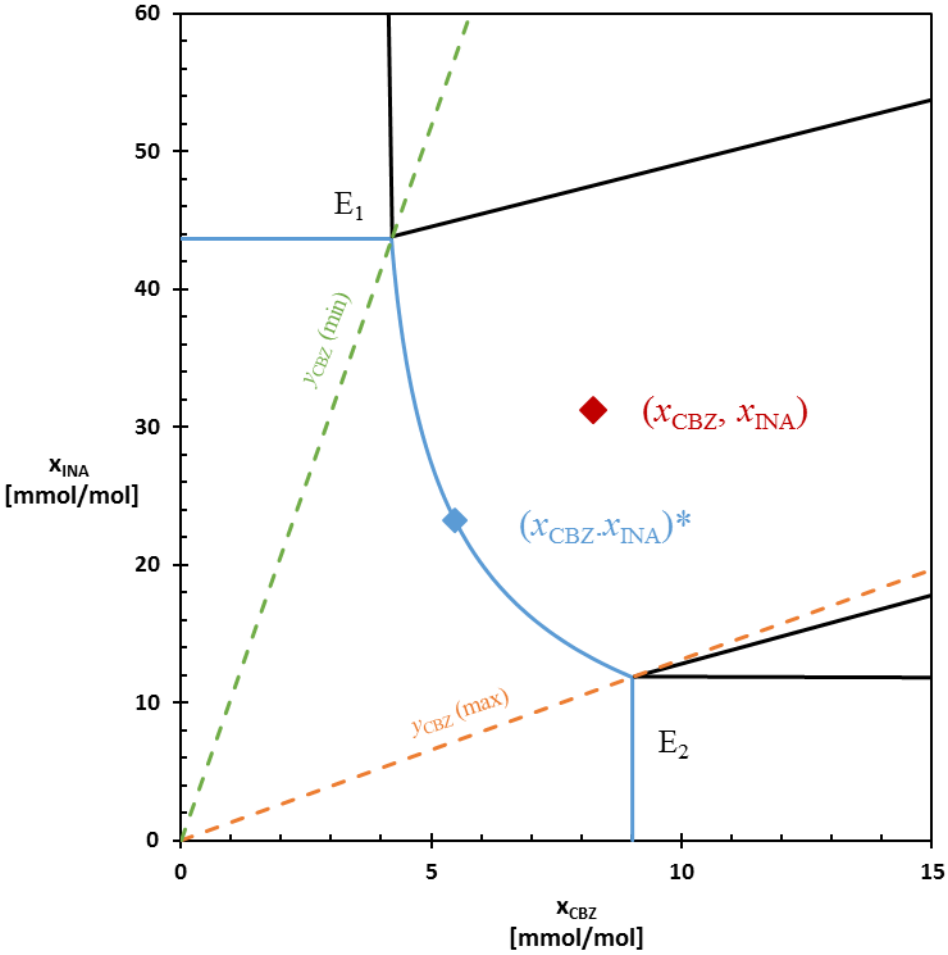

Figure 31 the schematic phase diagram of CBZ-INA at T = 35°C. The curved part of the blue line is the solubility of the co-crystal. The straight lines from the axes that intersect the curve line are the solubility of the pure components at 35°C. The assumption here is that the solubility of the pure component is unaffected by the presence of the other co-crystal formers. y_{CBZ} (min) and y_{CBZ} (max) are the minimum and maximum stoichiometries in the co-crystal region respectively. The stoichiometry within this range is important for co-crystallisation kinetics. E_1 and E_2 are the eutectic points mole fractions based on solubility of the pure components. The supersaturation ratio is determined from the ratio of the concentration product (x_{CBZ},x_{INA}) and the solubility product $(x_{CBZ}x_{INA})^*$.

The previous work (chapter 3) on the phase diagram of carbamazepine and isonicotinamide in the solvents ethanol, nitromethane and dioxane identified the co-crystal region of the phase diagram where the stable form of the CBZ-INA co-crystal equilibrates in all solvents. For a

particular temperature and solvent, this co-crystal region extends over a range of mole concentration of co-crystal pure components carbamazepine and isonicotinamide. To represent the stoichiometry of carbamazepine and isonicotinamide, we can define the stoichiometry through the mole fractions x_{CBZ} and x_{INA} of CBZ and INA as in the equation below. Where y_{CBZ} is the solvent free mole fraction.

$$y_{CBZ} = \frac{x_{CBZ}}{x_{CBZ} + x_{INA}} \qquad 30$$

The mole fraction of the pure component solubilities at a given temperature limits the pure co-crystal region because a saturated solution cannot further dissolve additional pure component crystals. Therefore, the eutectic point at a given temperature is the point where the co-crystal solubility and the pure component solubility intersects. Since this system contains two components, the solubility of one component is x_{CBZE1} and the other component $x_{INAE1.}$ Where E1 can be substituted for E2 for the other eutectic point. Then, the minimum and maximum stoichiometries y_{CBZ} (min) and y_{CBZ} (max) in the co-crystal region can be determined:

$$y_{CBZ}(min) = \frac{\left[\frac{(x_{CBZ} \cdot x_{INA})^*}{x^*_{INA}}\right]}{\left[x^*_{INA} + \frac{(x_{CBZ} \cdot x_{INA})^*}{x^*_{INA}}\right]} \qquad 31$$

$$y_{CBZ}(max) = \frac{[x^*_{CBZ}]}{\left[x^*_{INA} + \frac{(x_{CBZ} \cdot x_{INA})^*}{x^*_{CBZ}}\right]} \qquad 32$$

Figure 31 shows a typical phase diagram of a co-crystal and pure components divided into 5 regions. Region I is the region of the phase diagram in which the pure component solid INA is in equilibrium with the solution. Region II is the part of the phase diagram where there is equilibrium between INA, CBZ: INA and solution of eutectic composition. Region III is where CBZ-INA is equilibrium with the solution. Region IV is where CBZ-INA and CBZ are in equilibrium with the solution while region V is where the pure CBZ is at equilibrium with solution.

Table 10 shows parameters used for the phase diagram construction and stoichiometries y_{CBZ} (min) and y_{CBZ} (max). The difference in the eutectic point stoichiometry is due to the solvent. For example, the stoichiometry $y_{CBZ} = 0.5$, which is equivalent to the solid form stoichiometry of the co-crystal does not fall within the co-crystal region in ethanol as it is in nitromethane and dioxane. Also, the CBZ-INA is demonstrated to display a solvent mediated transformation from the metastable form to the stable form when suspended in ethanol.[12] We are interested in the co-crystal nucleation behaviour as a function of the stoichiometry y_{CBZ} between y_{CBZ} (min) and y_{CBZ} (max). Within these values, the stable form of the co-crystal is obtained in all solvents. Outside these values, another solid is the stable form.

Table 10. The stoichiometry range y_{CBZ} (min) $< y_{CBZ} < y_{CBZ}$ (max) determined from the phase diagram eutectic point determination.

		Parameters			Eutectic points	
Solvents	Solute	$A \times 10^3$	b_1	b_2	y_{CBZ} (min)	y_{CBZ} (max)
EtOH	CBZ-INA	-7.65±1.25	0.060± 0.003	15.49 ± 0.40	0.09	0.43
NM	CBZ-INA	-8.80±0.34	0.21±0.11	17.79±1.00	0.31	0.89
DIO	CBZ-INA	-5.52±0.38	0.11±0.10	10.11±0.94	0.33	0.68

Supersaturation is the driving force of nucleation. The supersaturation ratio towards a co-crystal can be expressed as

$$S = \frac{(x_A.x_B)}{(x_A.x_B)^*} \qquad 33$$

Where $(x_A.x_B)$ and $(x_A.x_B)^*$ are the co-crystal concentration product and solubility product in solution respectively. The solubility product was determined from the parameters in Table 10. The concentration product was determined by the mass of CBZ and INA transferred into the vial. For example, the supersaturation ratio for y_{CBZ} = 0.129 at 34°C in ethanol with $x_{CBZ} =$ 6.77 and $x_{INA} = 45.39$ concentration product is expressed as $S = \frac{0.000307}{0.000129}$ = 2.34.

We want to measure nucleation rates under controlled supersaturation ratio conditions within the co-crystal region. This means that at the measurement temperature the composition determined by $(x_A.x_B)^*$ lies on the co-crystal solubility line within the co-crystal region is limited by y_{CBZ} (min) and y_{CBZ} (max).

5.3.2 Co-crystallisation Kinetics

5.3.2.1 Metastable zone width measurements

Figure 1a, b and c show the cloud points T_c and the average clear point temperature T_s measured at different solution stoichiometries in EtOH, NM and DIO, respectively. The clear point temperatures are approximating the saturation temperature and therefore are a thermodynamic quantity not expected to be influenced by kinetics. The variation of the clear point temperature in the multiple measurements of a single sample is no more than 1.5°C. The small variations

in clear points at different stoichiometries are due to slight variations in sample composition originating from sample preparation.

In contrast, the measured cloud point temperatures T_c for a single sample show a substantial variation. For example, the measured T_c for stoichiometry y_{CBZ} = 0.140 in the solvent EtOH varies from 15.4°C to 33.2°C. This variation in T_c attests to the stochastic nature of nucleation in small stirred volume. Similar variations were observed at other stoichiometries and solvents. The black dashed lines in Figure 32 signifies eutectic point compositions based on the phase diagram described at the beginning of this section. These black dashed lines indicate y_{CBZ} (min) and y_{CBZ} (max) and all stoichiometries between the dashed black lines are within the co-crystal region of the phase diagram.

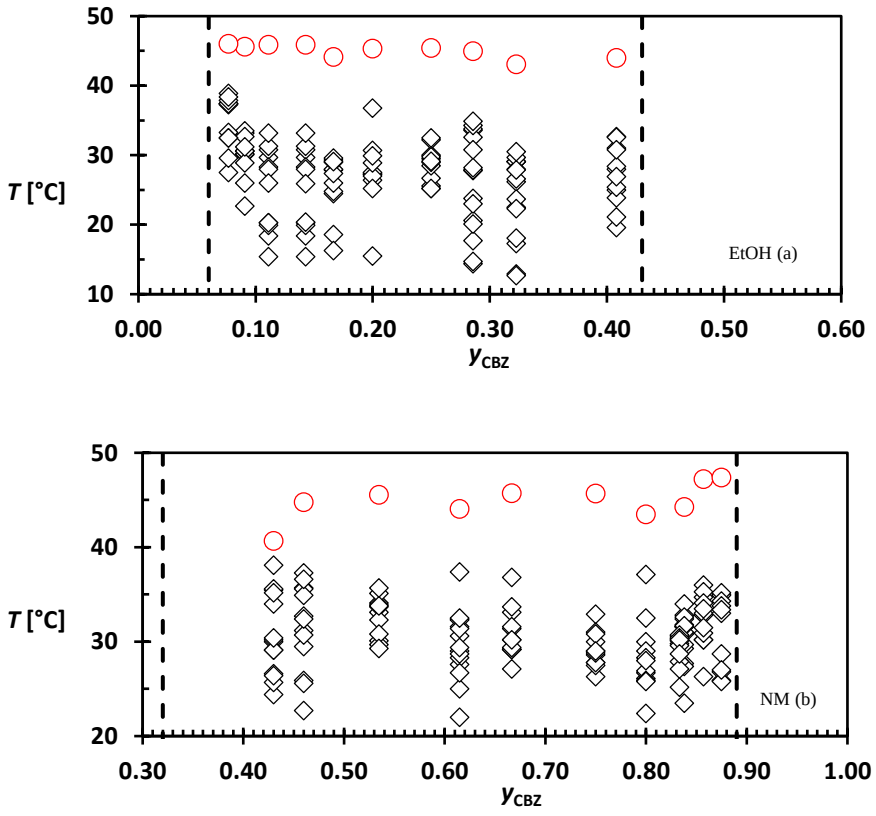

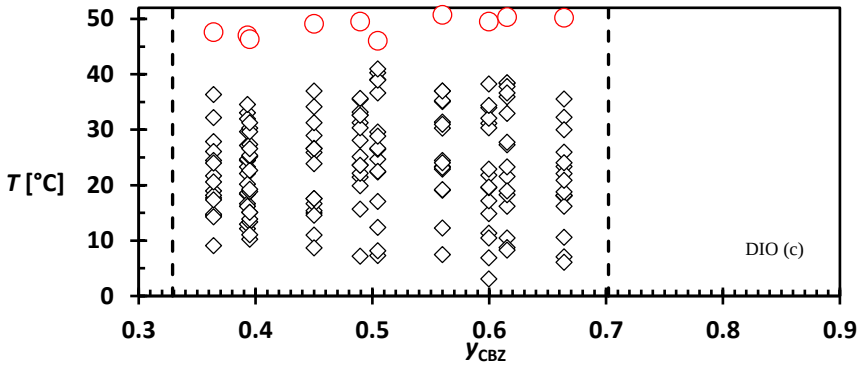

Figure 32. Clear point (red ○) and Cloud point (◊) temperature measurements as a function of stoichiometry in CBZ and INA solutions in EtOH (a), NM (b) and DIO (c). The clear point is an average of all measured points. The deviation in these measured T_s for a particular y_{CBZ} and all y_{CBZ} is less than the symbol size and not more than 1.5°C. The eutectic point stoichiometry of the co-crystal region y_{CBZ} (min) and y_{CBZ}(max) is indicated by black dash lines. The variation of clouds points in different solutions describes the stochastic nature of nucleation in multicomponent system.

The metastable zone width ΔT is determined from the difference between the average clear point T_s and the cloud points T_c of the same y_{CBZ}. Figure 33 shows the metastable zone widths of CBZ-INA in EtOH, NM and DIO For all cloud points. There is a lot of variation in the measured ΔT at different stoichiometries in all solvent system. Even at stoichiometry with the smallest ΔT. For example, the smallest ΔT in ethanol is at y_{CBZ} = 0.25 ranges from 12.9 to 19.8°C. The variation in the measured ΔT at different stoichiometries in all solvent system reflects the stochastic nature of nucleation.

The MSZW is approximately 10°C for all solvents which indicates no solvent effect on the MSZW of this co-crystal. As a result, there is a chance CBZ-INA co-crystal has similar crystallisation behaviour regardless of the solvent used. This is opposite of the conclusion reached by Fredrik et al [13] where solvent has an effect on the metastable zone width. However, the variation in the smallest ΔT (y_{CBZ} = 0.25 for ethanol) data for each solvent system is too large to conclude. Therefore, the result of the metastable zone width in EtOH, NM and DIO show no clear observable trend in regards to increase in the concentration of co-crystal pure component. This is consistent with Boyd et al.[10] where no stoichiometry dependent effect on

the MSZW of benzoic acid –isonicotinamide co-crystals in ethanol at 1ml volume was observed.

The measured MSZW indicates the design space for induction time measurements which should take place within this zone. Therefore, we chose a temperature range between 32°C and 39°C to measure induction times for compositions with saturation temperature T_s = 45°C for all the solvents.

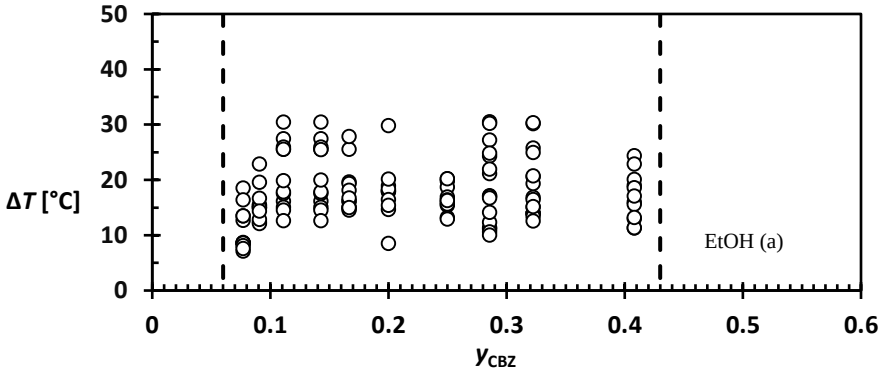

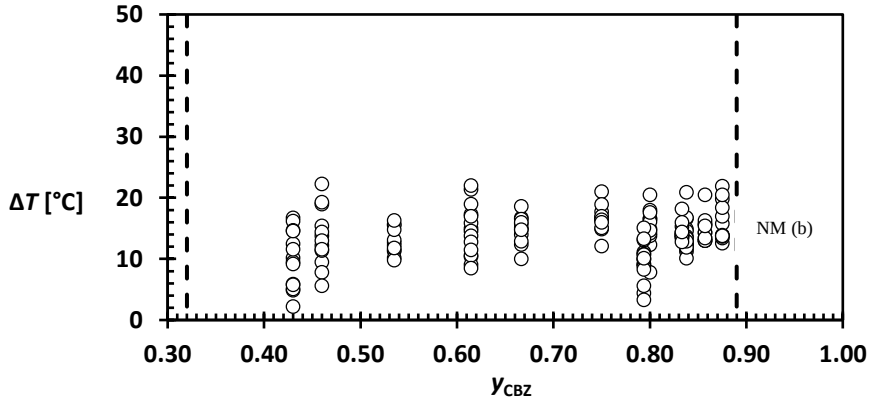

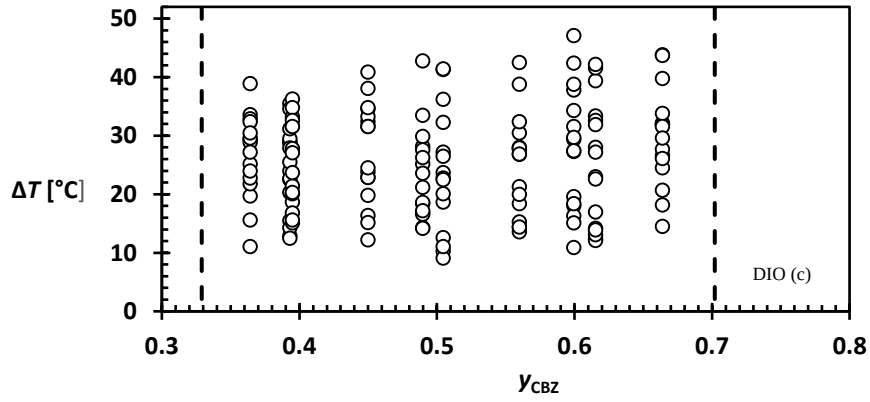

Figure 33. The metastable zone width of the CBZ - INA co-crystal for EtOH (a) NM (b) and DIO(c). There is no clear trend for the effect of y_{CBZ} on the MSZW in EtOH, NM and DIO.

5.3.2.2 Induction time distributions

The induction time *t* of a crystal from a solution is the period between the achievement of a constant supersaturation and the detection of crystals. The probability *P*(*t*) to detect crystal at time *t* can be represented by the cumulative distribution function below. This function is valid when $t \geq t_g$

$$P(t) = 1 - \exp\left(-JV\left(t - t_g\right)\right) \qquad 34$$

Where *J* is the nucleation rate of a crystallising solution, *V* is the volume in which crystallisation is taking place, t_g is the growth time, the time delay between the formation of the first nucleus and the detection of crystal in a solution. The probability distribution of the induction time can be determined from experiments at identical conditions. For *M* experiments, the probability *P*(*t*) to measure an induction time *t* is defined as

$$P(t) = \frac{M^+}{M} \qquad 35$$

Where M^+ is the number of experiment in which crystals were detected up to time *t*. Equation 3 can be used to directly fit the experimental induction time probability distribution from eq. 4 in order to determine nucleation rate *J* and growth time t_g. According to the classical nucleation theory, the nucleation rate *J* at a supersaturation *S* can be represented by:

$$J(\mathrm{S}) = AS \exp\left(-\frac{B}{ln^2 \mathrm{S}}\right) \quad 36$$

Where *A* is the kinetic parameter and *B* is the thermodynamic parameter. These parameters are made up of other variables that can help explain the determined parameters and improve our understanding of factors affecting the nucleation rates. The parameter *B* reflects the thermodynamic level information on the effective interfacial energy between the nucleus and the solution and is a measure for the free energy barrier for nucleus formation. For heterogeneous nucleation, *B* can be described as

$$B_{HEN} = \frac{4}{27} c^3 v^2 \left(\frac{\gamma_{HEN}}{KT}\right)^3 \quad 37$$

Where *c* is a shape factor of the nucleus, *v* is the molecular volume of the crystals and γ_{HEN} is the effective interfacial energy. The pre-exponential factor *A* describes the molecular kinetics of the nucleation process and is described by

$$A = zf^* C_0 \quad 38$$

Where z is the zeldovich factor that expresses the tendency of the building unit clusters larger than the nucleus size to grow or decay. The attachment frequency of building units to the nucleus is reflected by *f**. In a single component system, the building units are assumed to combine one after the other. In a multicomponent system like co-crystal, the two components can attach. One of them might be rate limiting. C_0 is the concentration of nucleation sites and it is associated with the concentration of heterogeneous particles.

5.3.2.2.1 Experimental induction time distributions

The induction time measurements under equal conditions such as solution stoichiometry $y_{CBZ,}$ supersaturation S and solvent type produces a range of measurements. For example, the measured induction time at y_{CBZ} = 0.129 in EtOH at supersaturation S = 1.87 ranges from 300 s to 13,374 s. The smallest measurement at this condition represents the initial period within which no crystal were detected. In other words, the smallest induction time at 300s is the growth time t_g. Figure 34 shows the smallest induction time t_g plotted against the supersaturation for different solution stoichiometry and solvent. The smallest induction time measured in all solvent did not always decrease with increase in supersaturation. The smallest induction time at y_{CBZ} = 0.205 in EtOH at supersaturation S = 2.37 is 1.2 s and at S = 1.72 is 120 s. However, the trend in EtOH and NM is clearer than in DIO for the conditions examined as shown in Figure 34. For example, the measured t_g at y_{CBZ} = 0.505 in NM did not change significantly for the first three supersaturations before it starts to reduce as supersaturation increases.

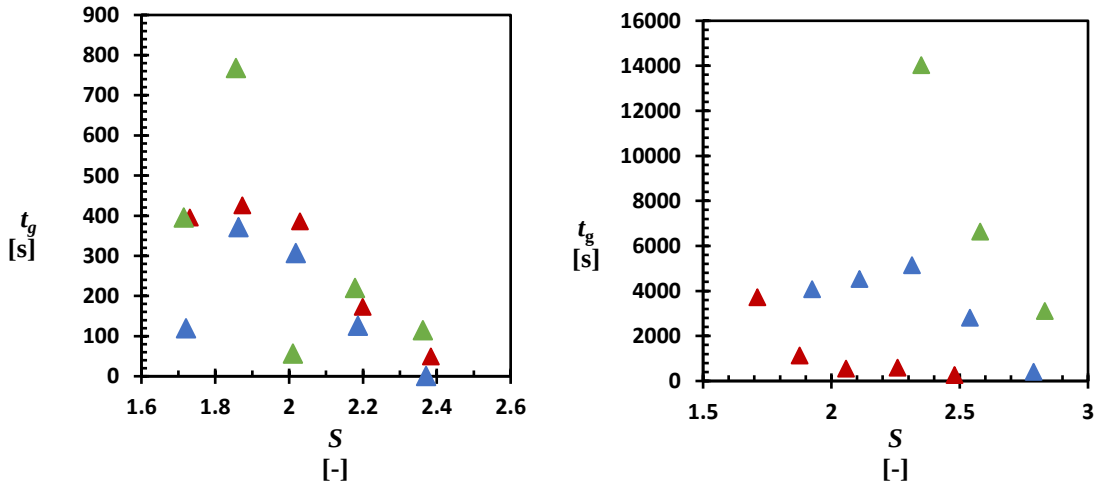

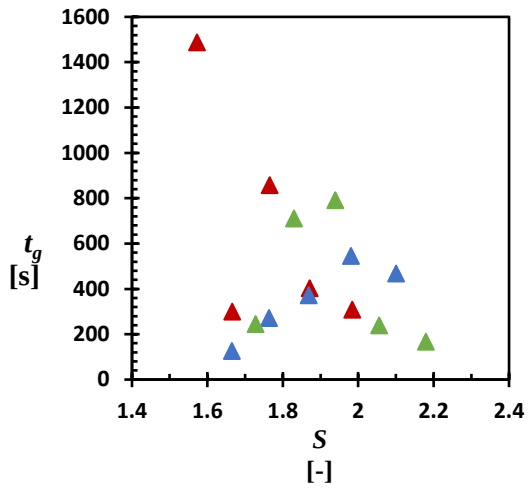

Figure 34. Growth rate t_g based on the smallest induction time measured at conditions in EtOH, NM and DIO as a function of supersaturation. (a) In EtOH for y_{CBZ} = 0.129 (red Δ), 0.203 (blue Δ) and 0.295 (green Δ) indicate that t_g is dependent on supersaturation. **(b)** NM for solution stoichiometry y_{CBZ} = 0.498 (red Δ), 0.752 (blue Δ) and 0.833 (green Δ) shows a slight dependence on supersaturation. (**c)** growth rate t_g in DIO as a function of supersaturation for y_{CBZ} = 0.393 (red Δ), 0.504 (blue Δ) and 0.615 (green Δ) shows less dependence on supersaturation.

The Induction time measurements under equal conditions for a multicomponent crystal like CBZ-INA from solution can be expressed in probability distributions using equation 6. For example, the expression of an induction time to the experimental probability *P*(t) for a solution stoichiometry y_{CBZ} = 0.129 in EtOH at supersaturation *S* = 1.87 when the total number of experiment is 16 and the probability that the 14th vail would nucleate is 0.87. The same procedure can be used for all other induction time at the same condition. As a result, a probability distribution of the induction time at this condition is presented as a curve when experimental probability *P*(t) [-] is plotted on the vertical axis and induction time *t* (s) on the horizontal axis. The probability distributions *P*(t) quickly increases and levels off towards a probability of 1 after the probability of the smallest induction time measurement. Figure 35, Figure 36 and Figure 37 shows the fitted probability distributions at different conditions in EtOH, NM and DIO respectively.

5.3.2.2.2 Experimental induction time distributions in ethanol

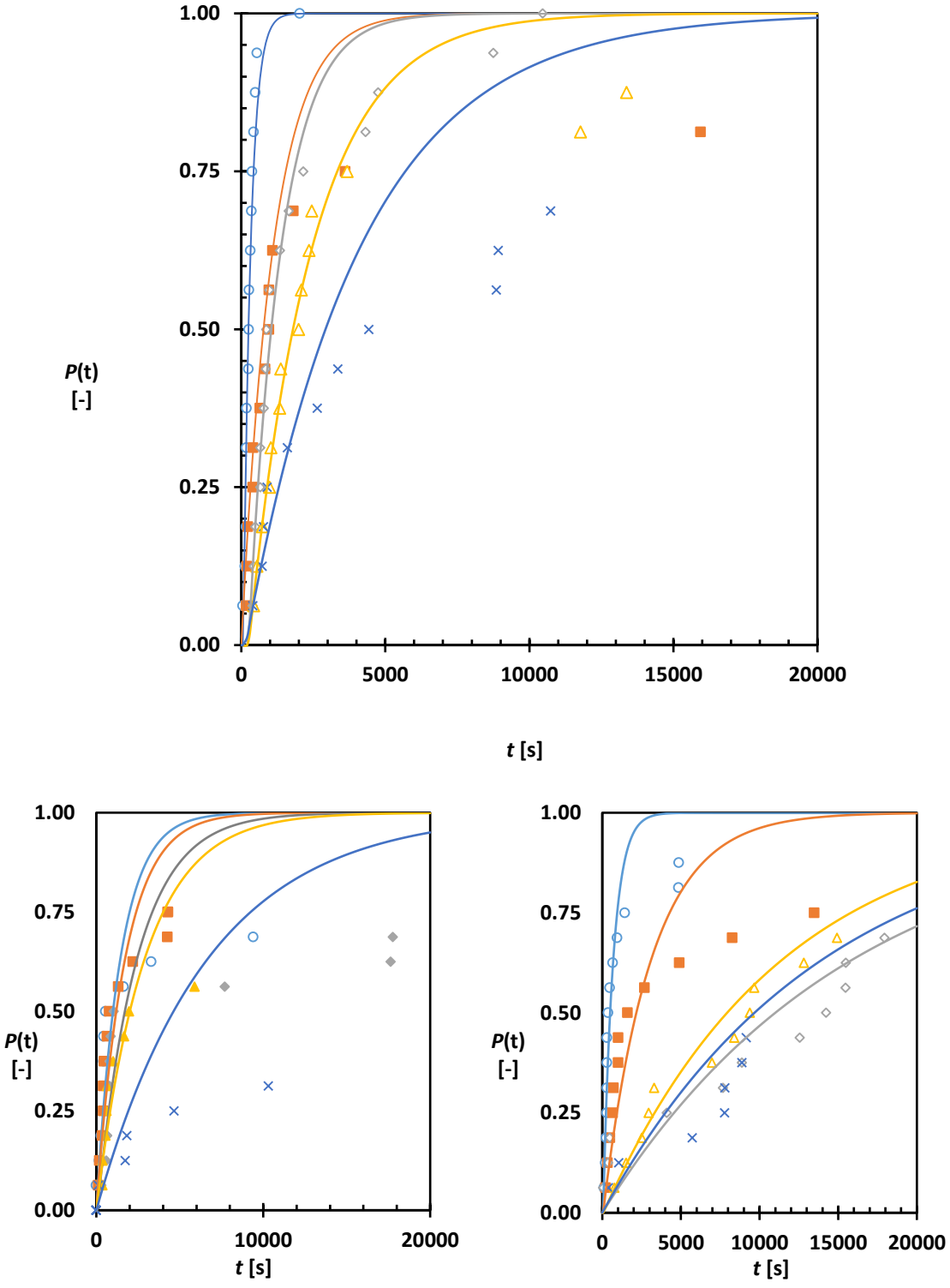

Figure 35. Experimentally determined probability distributions P(*t*) of CBZ - INA co-crystal in ethanol formed at solution stoichiometries y_{CBZ} **0.129** (a) at 5 different supersaturation ratios S = 1.73(blue □), 1.87(Yellow Δ), 2.03(grey ◊), 2.19(orange □), 2.38 (blue ○). y_{CBZ} **0.204** (middle) at 5 different supersaturation ratios S = 1.72(blue □), 1.86(Yellow Δ), 2.02(grey ◊), 2.19(orange □), 2.37 (blue ○) and y_{CBZ} **0.2948** (right) at 5 different supersaturation ratios S = 1.71(blue □), 1.86(Yellow Δ), 2.01(grey ◊), 2.18(orange □), 2.36 (blue ○)

5.3.2.2.3 Experimental induction time distributions in Nitromethane

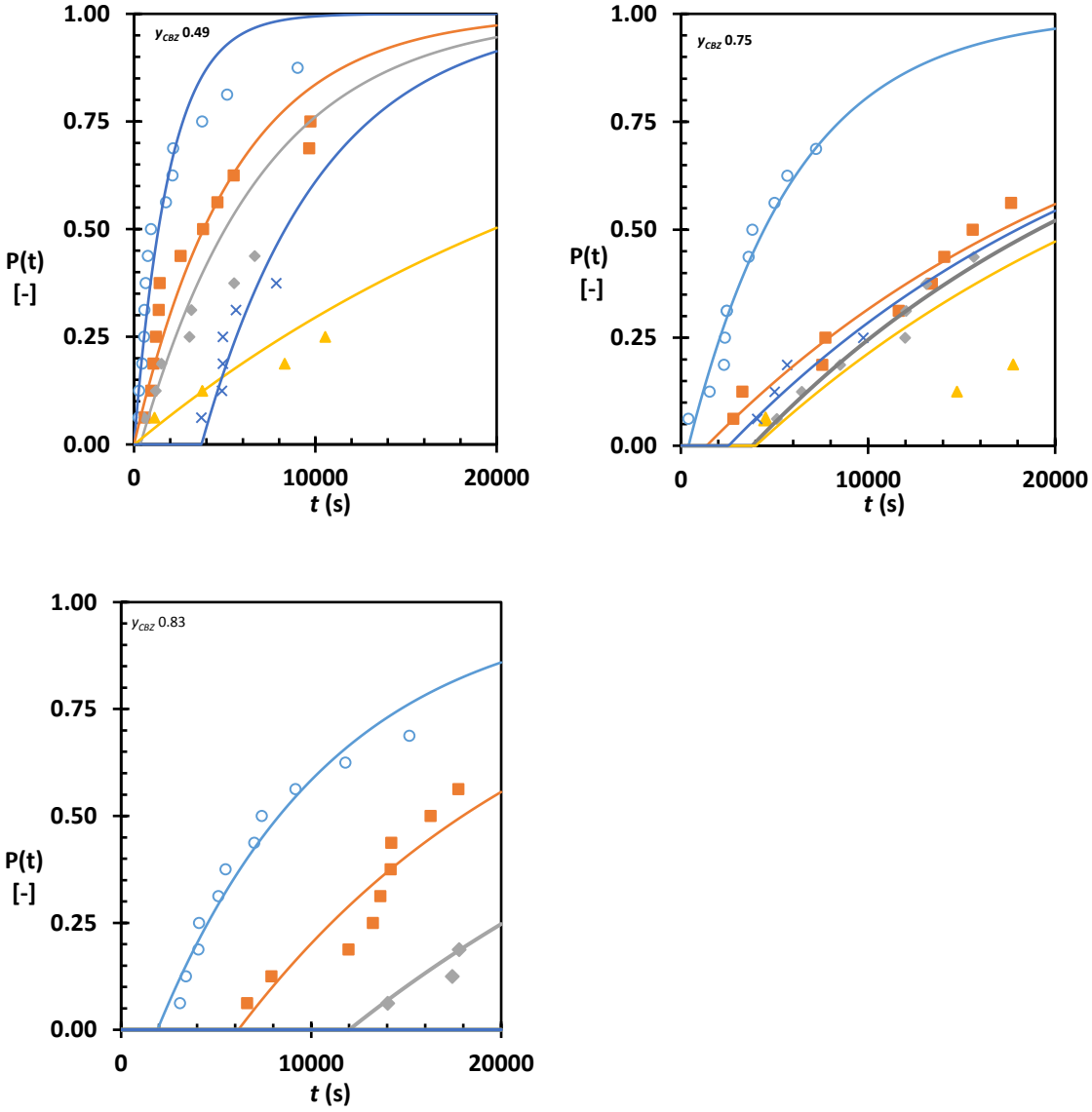

Figure 36. Experimentally determined probability distributions P(*t*) of CBZ - INA co-crystal in Nitromethane formed at solution stoichiometries y_{CBZ} **0.498** (left) at 5 different supersaturation ratios S = 1.71(blue x), 1.88(Yellow Δ), 2.06(grey ◊), 2.26(orange □), 2.48 (blue ○). y_{CBZ} **0.752** (middle) S = 1.92 (blue x), 2.11 (Yellow Δ), 2.31 (grey ◊), 2.54 (orange □), 2.79 (blue ○) and y_{CBZ} **0.833** (right) at supersaturations S = 2.35 (grey ◊), 2.58 (orange □), 2.83 (blue ○)

5.3.2.2.4 Experimental induction time distributions in dioxane

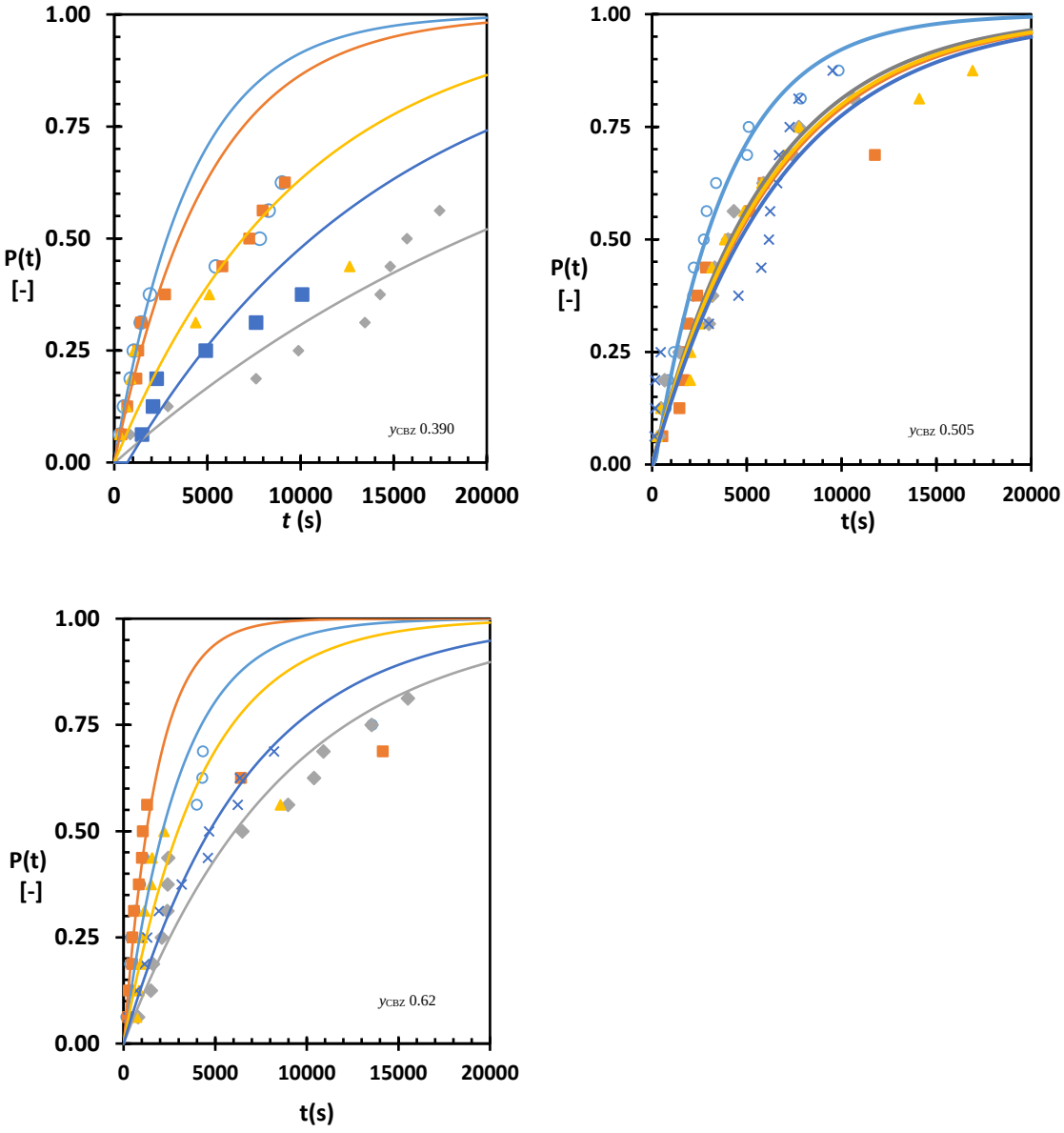

Figure 37. Experimentally determined probability distributions P(*t*) of CBZ - INA co-crystal in dioxane formed at solution stoichiometries y_{CBZ} **0.390** (left) at 5 different supersaturation ratios S = 1.57(blue □), 1.67(Yellow Δ), 1.77(grey ◊), 1.87(orange □), 1.98 (blue ○). y_{CBZ} **0.505** (middle) S = 1.67 (blue □), 1.76 (Yellow Δ), 1.87 (grey ◊), 1.98(orange □), 2.01 (blue ○) and y_{CBZ} **0.62** (right) at supersaturations S = 1.73 (blue □), 1.83 (Yellow Δ), 1.93 (grey ◊), 2.05(orange □), 2.18 (blue ○)

5.3.2.3 Distribution analysis

The induction time probability distribution makes induction time measurements accessible for the determination of nucleation rate J, growth time t_g and parameter A and B according to the classical nucleation theory. The kinetic parameter A and thermodynamic parameter B for CBZ-INA co-crystal at different conditions can be determined by using three different approaches with the aim of identifying the effect of data processing approach on parameter estimations. These approaches are tagged: approach I, Approach II and Approach III. These approaches are differentiated by the assumptions used during analysis.

Approach I

The measured induction time distributions were analysed using three approaches to determine the kinetic factor A and thermodynamic factor B of the nucleation rate equation from the classical nucleation theory.[14] **Approach I** was applied as an example to the measured induction time distribution at solution stoichiometry y_{CBZ} = 0.129 at S = 1.72, 1.87, 2.02, 2.19 and 2.38 in EtOH following three steps. First, the experimentally measured induction time is expressed as a probability distribution using equation 35. Secondly, the obtained induction time probability distribution is then fitted using equation 34 to obtain growth rate t_g and nucleation rate J. The third step involves plotting ln J/S against $\ln^{-2}S$ for the determination of parameters A and B using equation 7.

Figure 35a shows the fitted experimental probability distribution P(t) for solution stoichiometry y_{CBZ} = 0.129 at S = 1.72, 1.87, 2.02, 2.19 and 2.38 in EtOH using equation 5. At the low end of the supersaturation range S = 1.72, for nucleation rate J of 250 $m^{-3}s^{-1}$ and t_g of 150s. At the high end of the supersaturation S = 2.38, nucleation rate J of 3931 $m^{-3}s^{-1}$ and t_g 72.39s. Using the same approach for all supersaturations examined at y_{CBZ} = 0.129 in EtOH, the determined nucleation rate and growth rate can then be determined. Now that J and t_g are estimated for conditions examined in EtOH, a plot of ln J/S against $\ln^{-2}$S according to equation

36 can be used to determine the parameters *A* and *B*. Figure 38 shows the plot for ln *J*/S against $\ln^{-2}S$ for solution stoichiometry y_{CBZ} = 0.129 for all supersaturations. Where kinetic parameter *A* = 3646.8 $m^{-3}s^{-1}$ ± 0.036 and thermodynamic parameter *B* is 1.026 ± 0.295 from the slope and intercept respectively. The estimated parameters for other y_{CBZ} in EtOH and other solvents can be determined. The summary of parameter estimations using approach 1 is shown in Table 11

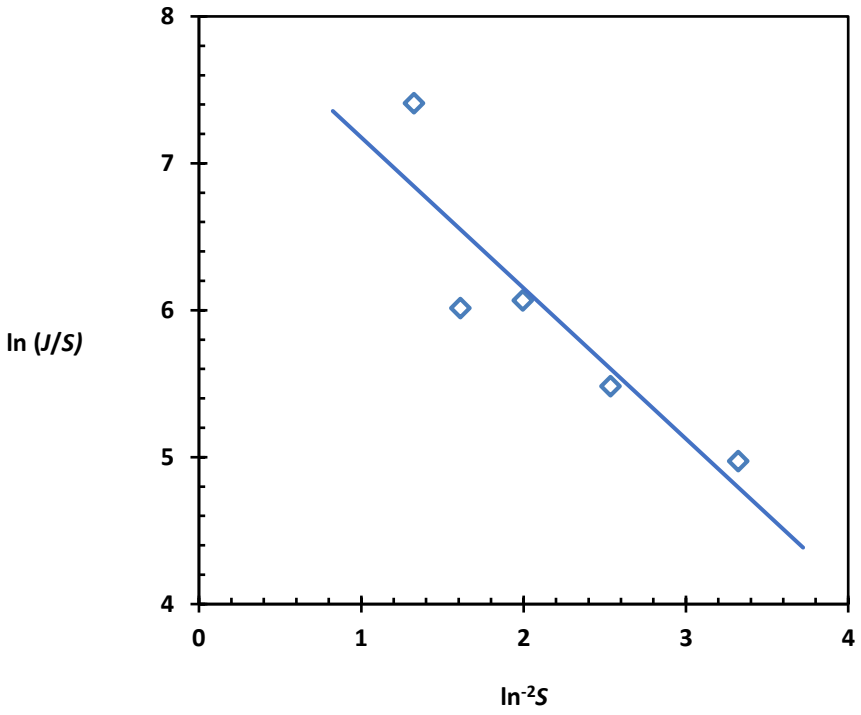

Figure 38. ln (*J*/*S*) against $1/\ln^2 S$ of the set of induction time measurements for y_{CBZ} = 0.129 for EtOH. The nucleation rate parameters *A* and *B* are determined from intercept and slope respectively for approach I

Approach II

In **approach II** the growth time t_g is set to the fastest induction time measured in a series of induction time for solution stoichiometry y_{CBZ} = 0.129 at *S* = 1.72, 1.87, 2.02, 2.19 and 2.38 in EtOH. In this case t_g varies with increase in supersaturations. The difference between approach II and approach I is that t_g is set as the smallest induction time in approach II and fitted for approach I. In this way, equation 32 at a measured induction time *t* has only one unknown variable, the nucleation rate *J*, which can then be determined for each induction time *t* measured

at a particular supersaturation S for a solution stoichiometry y_{CBZ}. The average nucleation rate J can then be determined and $\ln J/S$ and $\ln^{-2} S$ can be plotted to determine parameters A and B. The details of estimated parameters are shown in Table 11.

Table 11 the kinetic parameter ln A and thermodynamic parameter B of the nucleation rate equation from the classical nucleation theory determined from induction time measurements analysed using three different approaches for comparison.

		Approach I		Approach II		Approach III		
Solvent	y_{CBZ}	ln A	B	ln A	B	ln A	B	R^2
EtOH	0.129	8.20 ± 0.67	1.02± 0.29	8.61 ± 0.22	1.05 ± 0.20	6.62 ±	0.40 ±	0.65
	0.204	6.51 ± 0.18	0.57 ± 0.08	7.22 ± 1.99	0.67 ± 0.86	6.10 ±	0.95 ±	0.82
	0.295	6.95 ± 1.41	1.11 ± 0.60	7.58 ± 0.99	1.24 ± 0.42	6.00 ±	0.40 ±	0.02
NM	0.498	5.15 ± 1.15	0.41 ± 0.51	5.91 ± 1.36	0.64 ±0.598	5.90 ±	0.70 ±	0.71
	0.752	4.64 ± 1.21	1.07 ± 0.88	3.71 ± 1.46	0.24 ± 0.91	4.50 ±	0.11 ±	0.39
	0.833	5.49 ± 0.36	2.05 ± 0.31	6.54 ± 1.42	2.68 ± 1.24	3.59 ±	0.40 ±	0.62
DIO	0.390	5.55 ± 0.14	0.37 ± 0.04	4.82 ± 1.52	0.22 ± 0.44	4.60 ±	0.90 ±	0.71
	0.505	4.75 ± 0.30	0.08 ± 0.11	5.35 ± 0.44	0.19 ± 0.16	5.20 ±	0.11 ±	0.87
	0.615	5.81 ± 1.07	0.43 ± 0.43	6.32 ± 1.22	0.46 ± 0.47	5.80 ±	0.50 ±	0.65

Approach III

The growth time t_g in **Approach III** is set to the shortest induction time similar to approach II for solution stoichiometry y_{CBZ} = 0.129 at S = 1.72, 1.87, 2.02, 2.19 and 2.38 in EtOH. In this approach we assume the nucleation rate equation describes the data well so that parameter A and B can be obtained directly by fitting combined equation 34 and equation 36 to obtain equation 37.

$$P(t)_{model} = 1 - \exp\left[-\left(ASexp\left(-\frac{B}{\ln^2 S}\right)\right) * V(t - t_g)\right] \quad 39$$

Following the fit, the experimentally determined induction time probability distribution $P(t)$ can be plotted against $P(t)_{model}$ for all three stoichiometries in each solvent system. Figure 39 shows the best fit of $P(t)$ plotted against $P(t)_{model}$ for the first solution stoichiometry y_{CBZ} in each solvent systems. Solution stoichiometry y_{CBZ} = 0.129 in EtOH, 0.490 in NM and 0.393 DIO respectively. When $P(t) = P(t)_{model}$ the R^2 value in the plot would be expected to be 1. In all the plots, the R^2 is less than one, so $P(t) \neq P(t)_{model}$ suggesting that the model is not fully describing the experimental data. In all cases the coefficient of determination R^2 was used as an indicator for the best fit to determine parameter *A* and *B*.

The plot of experimental data $P(t)$ and model $P(t)_{model}$ for y_{CBZ} = 0.129, 0.203 and 0.298 in EtOH result in R^2 value of 0.65, 0.82 and 0.02 respectively. The decrease in coefficient of determination for 0.298 was attributed to the model prediction at supersaturations S = 2.18 and 2.36 based on the comparatively low value of J used in the calculation. The remaining predicted probability distribution at other supersaturations is within the same order of magnitude. In NM system the investigated y_{CBZ} = 0.498, 0.752, 0.830 and 0.618 has a respective R^2 values of 0.71, 0.39 and 0.618. In DIO system solution stoichiometry y_{CBZ} = 0.393, 0.505 and 0.615 yielded parameter *A* and *B* at R^2 of 0.71, 0.87 and 0.65 respectively. The reliability of the fit varies considerably when coefficient of determination is used so R^2 value was used as a guide. The plot for the experimental and the model probability distribution for other conditions is detailed in appendix C.

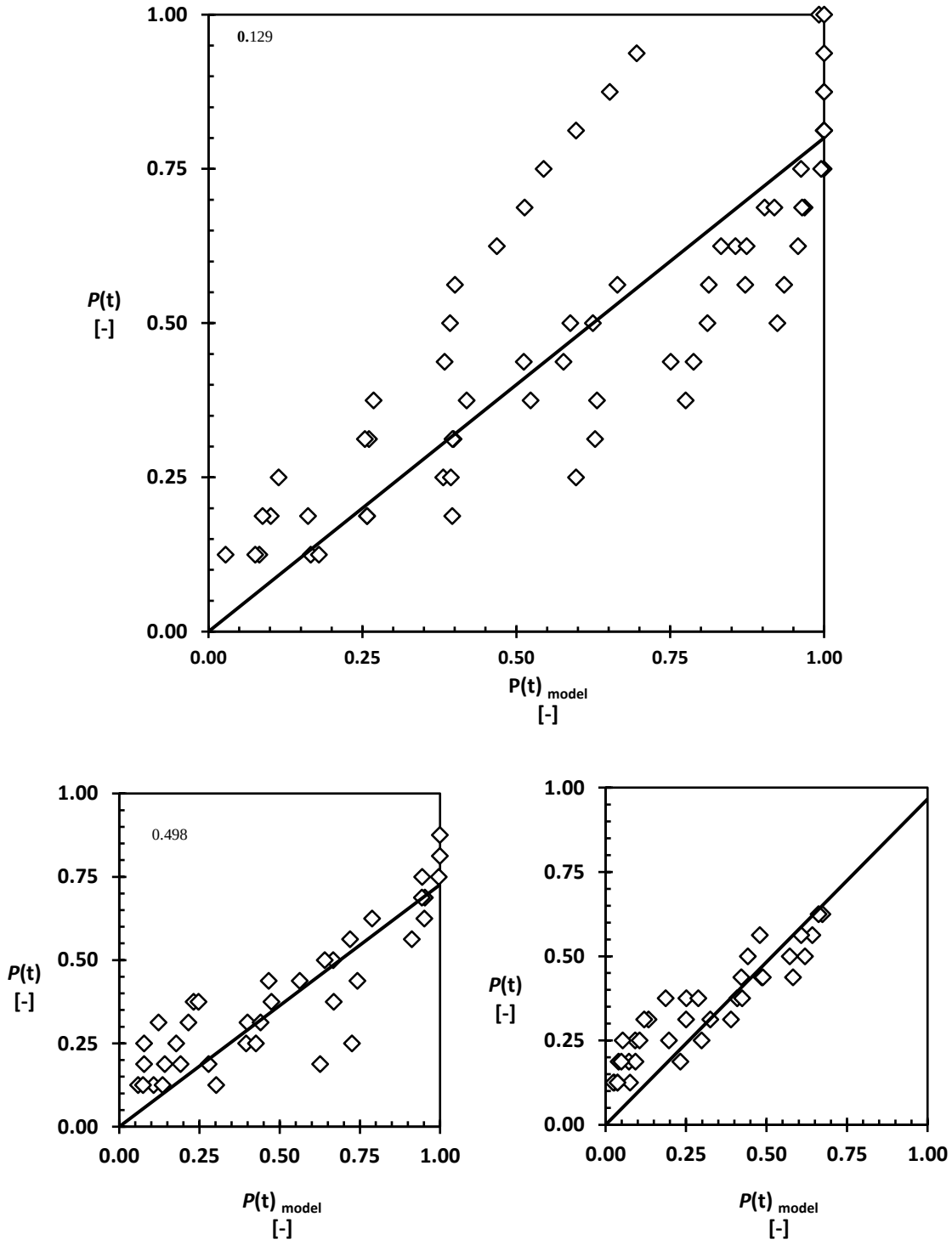

Figure 39. Plot of $P(t)$ and $P(t)_{model}$ at solution stoichiometry y_{CBZ} 0.129, 0.498 and 0.393 in EtOH, NM and DIO respectively to determine parameter *A* and *B*.

5.3.2.4 Approach comparison

Different distribution analysis was performed to capture and demonstrate the extent the non proportional supersaturation dependent changes in the experimental growth rate t_g determined either from the shortest induction time measured in the experimental induction time distributions in Figure 34 or fitted probability distribution to obtain nucleation rate J and tg using approach I as summarised in Figure 40 and appendix C. Approach I was used in detail here because it is generally used in the literature.

Figure 40 shows the nucleation rate *J* and for all conditions examined in EtOH, NM and DIO. The nucleation rate *J* increases with supersaturation *S* in EtOH. In other words the induction time distribution shifts to shorter times at higher supersaturation in EtOH. A partial dependence on supersaturations was observed in NM and DIO systems. For example, at y_{CBZ} = 0.498 in NM, nucleation rate decrease from 150 $m^{-3}s^{-1}$ at *S* = 1.71 to 35 $m^{-3}s^{-1}$ at *S* = 1.88 and then increase to 148 $m^{-3}s^{-1}$ at *S* = 2.06 beyond which an increase in a supersaturation shows increase in nucleation rate *J*. The direct proportionality of supersaturation on nucleation rate *J* in DIO is less obvious compared to the other solvents but there are indications that *J* is dependent on *S* for this system at certain conditions. For example, there are supersaturations where the nucleation rate *J* is lower than the preceding measurements or relatively constant when *S* is increasing. At solution stoichiometry y_{CBZ} = 0.393 where nucleation rate decreased from 100$m^{-3}s^{-1}$ at *S* = 1.67 to 36.8 $m^{-3}s^{-1}$ and then increased again to 200$m^{-3}s^{-1}$ at *S* = 1.87 is in contrast to y_{CBZ} = 0.504 where the nucleation rate was almost constant as *S* increases.

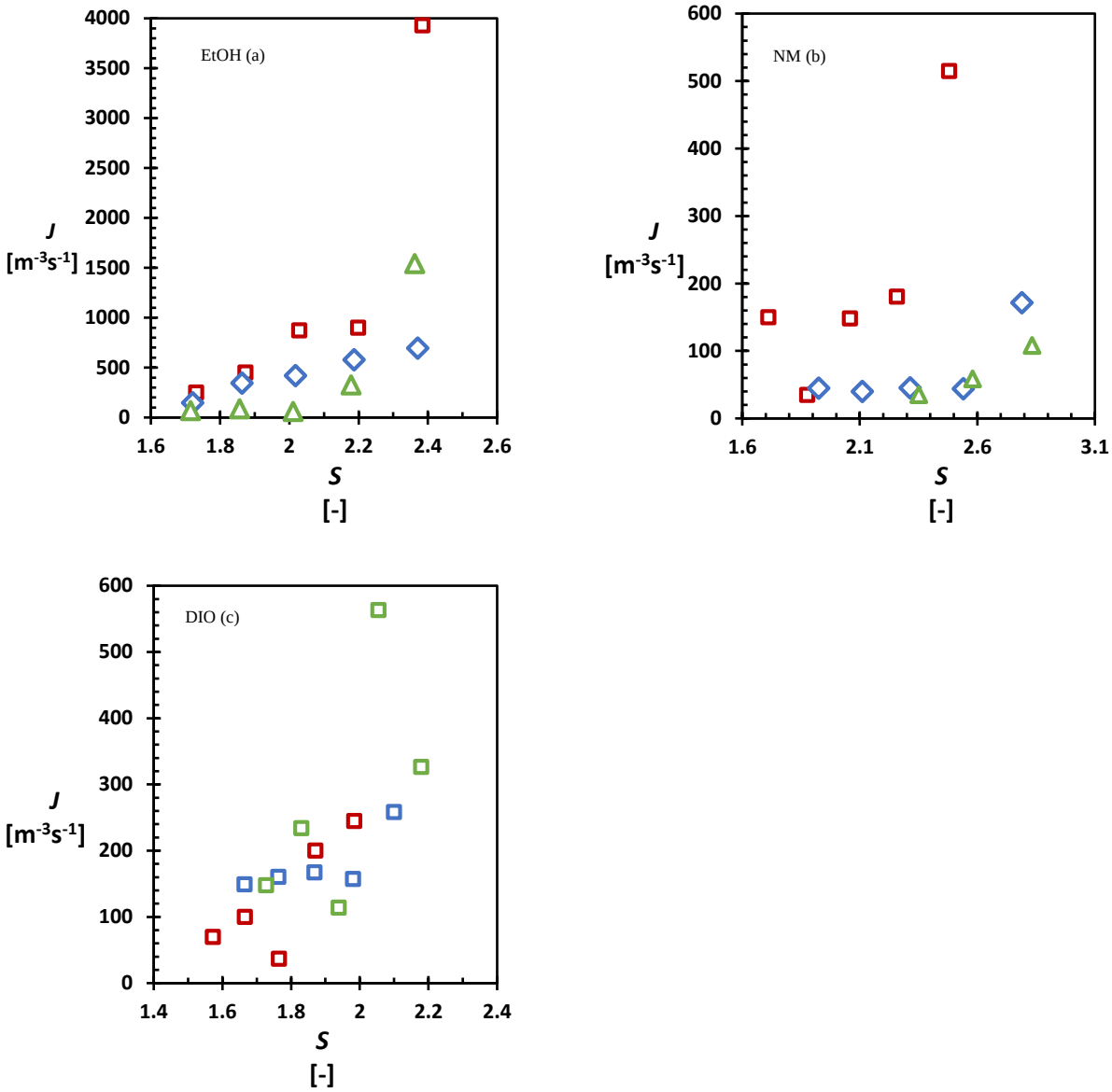

Figure 40 Nucleation rate of CBZ-INA co-crystal in EtOH, NM and DIO at conditions based on solution stoichiometry and supersaturations. (a) Nucleation rate J of CBZ-INA in EtOH as a function of supersaturation for y_{CBZ} = 0.129 (red □), 0.203 (blue ◊) and 0.295 (green Δ). The nucleation rate increases in EtOH as supersaturation increases. (b) Nucleation rate J of CBZ-INA in NM as a function of supersaturation with solution stoichiometry y_{CBZ} = 0.498 (red □), 0.752 (blue ◊) and 0.833 (green Δ). J increases partially as supersaturation increases at certain supersaturations NM system (c) nucleation rate J in DIO for y_{CBZ} = 0.393 (red □), 0.504 (blue □) and 0.615 (green □). Nucleation rate in DIO does not show a direct supersaturation dependence at certain supersaturations suggesting that crystal form obtained may be different at different supersaturations.

The partial or unclear supersaturation dependent growth rate t_g and nucleation rate J at certain conditions is not in agreement with expectation. It was expected that the relationship between nucleation rate J should be directly dependent on S in all y_{CBZ} investigated and t_g should be inversely relatable with S judging from previous experiments conducted for single component crystals.[3][6] The partial supersaturation dependence on J and t_g occurs in EtOH, NM and DIO to varying degree. It was suspected that conditions where supersaturation dependence disagrees with expectation may be due to polymorphism wholly or in part. However, the PXRD of randomly selected samples describes the presence of the stable CBZ-INA co-crystal. Since these variations is seen in all the solvents, this suggest that the variation is not localised to only one solvent and the effect of solvent on the nucleation rate of the co-crystal would be challenging to determine.

Now that the general nature of our experimental induction time distributions is described and the distribution analytical approach is described the best analytical approach for this data can be determined. Data for y_{CBZ} 0.129 in EtOH at supersaturation ratios S = 1.73, 1.87, 2.03, 2.19, 2.38 was selected for approach comparison. Figure 41 shows the fit of experimental data at these conditions. Approach II shows the poorest fit for P(t) below 0.5 when t_g was taken as the smallest induction time measurement and the variation observed in growth time is indicated in the nucleation rate obtained. Approach I showed a better fit by accounting for most of the probability distributions below P(t) = 0.5 and less so as probability increases to 1. Approach III showed the best fit for the data because it gives the scope and variables can be changed despite a low coefficient of distribution of 0.65 for instance the probability distribution for when S = 1.73 accounts for all data below or above P(t) = 0.5 but showed the poorest resolution of the fit at range of higher supersaturations.

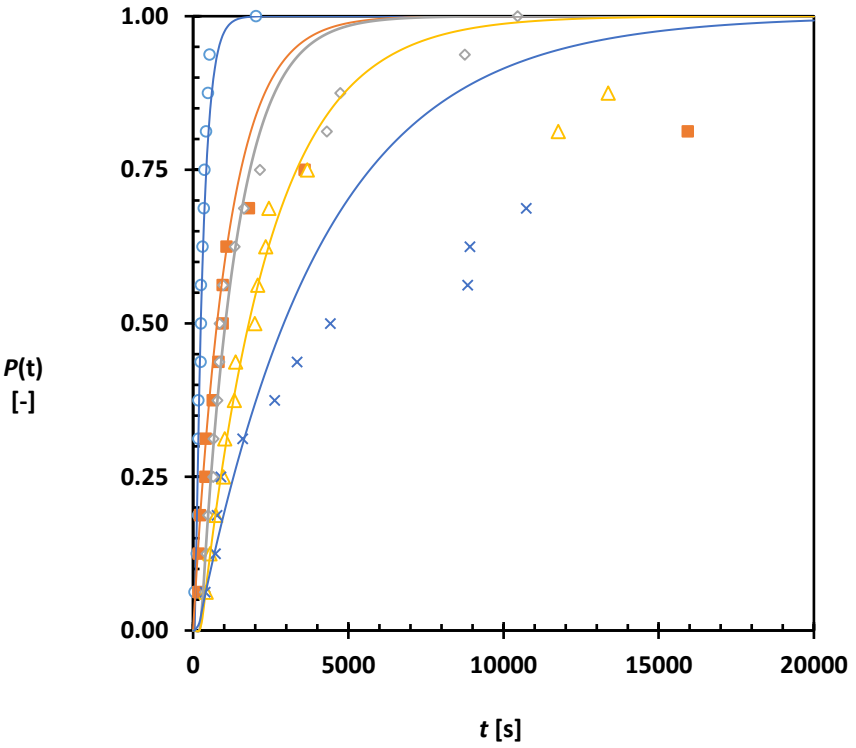
1.00
0.75
0.50
0.25
0.00
P(t)
[-]
0
5000
10000
15000
20000
t [s]

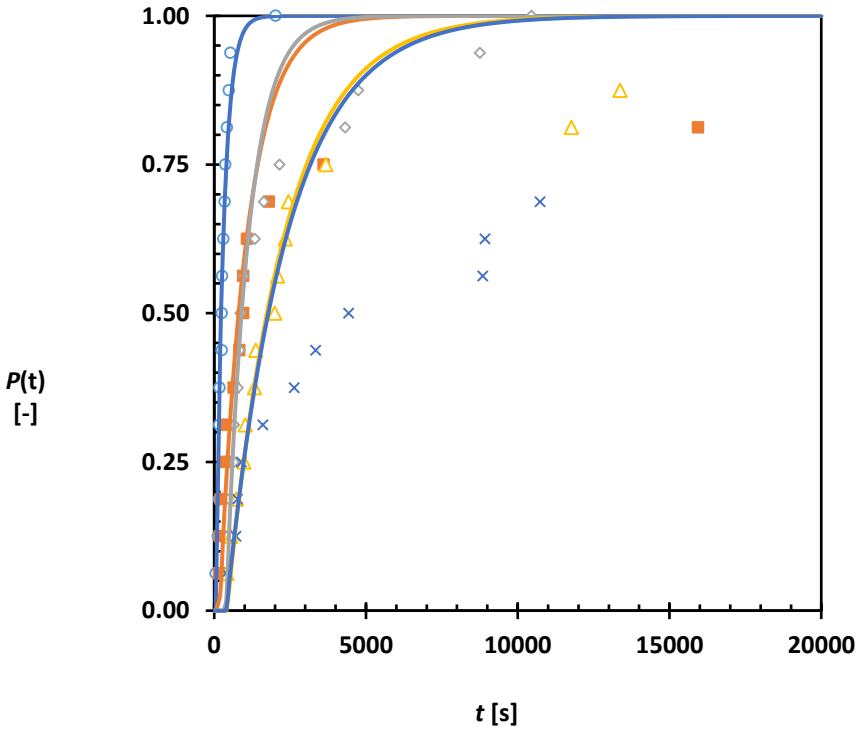
1.00
0.75
0.50
0.25
0.00
P(t)
[-]
0
5000
10000
15000
20000
t [s]

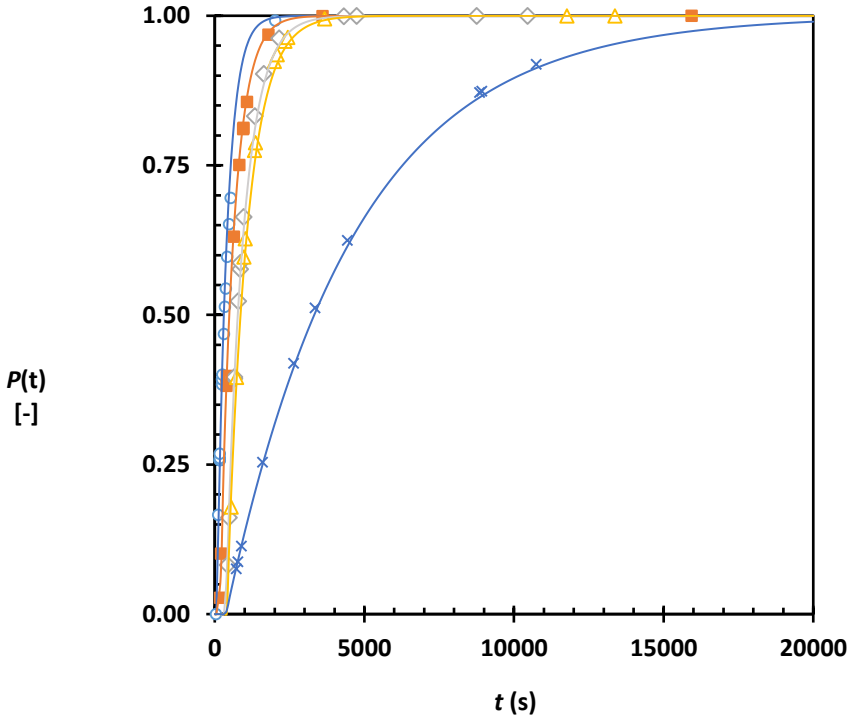

Figure 41 comparing the analytical approach for the determination of nucleation rate J and growth rate t_g for CBZ - INA co-crystal in ethanol at solution stoichiometry y_{CBZ} 0.129 and supersaturation ratios S = 1.73(blue □), 1.87(Yellow Δ), 2.03(grey ◊), 2.19 (orange □), 2.38 (blue ○) using the three approaches. (a) Approach I involves fitting the probability distribution to determine J and t_g and ultimately A and B according to the classical nucleation theory (b) involves determination of growth rate t_g from the shortest induction time measured at particular supersaturation to determined J and then parameter A and B using the classical nucleation theory (c) approach III is based on using a model to determine parameter A and B by combining all data set. Approach III showed the best fit for the probability distribution data.

Table 12 shows the determined nucleation rate J and t_g from the approach comparison for distribution analysis. The trend for nucleation rate J is similar except for approach II S = 2.20 where J = 1100 $m^{-3}s^{-1}$ is lower than the preceding nucleation rate at 1345 $m^{-3}s^{-1}$. The nucleation rate at approach I, II and III at the lowest supersaturation ratio S = 1.73 are 250, 500 and 235 $m^{-3}s^{-1}$ respectively. Showing a relatively small deviations compared to nucleation rate at the highest supersaturation S = 2.38 are 3931, 3931 and 3000 $m^{-3}s^{-1}$ showing a massive difference in nucleation rate. Despite this difference, approach III model, account for all the data compared to other approaches therefore it was chosen as the best approach for analysis.

Table 12 approach comparison for distribution analysis. The nucleation rate J and growth rate t_g for y_{CBZ} 0.129 and supersaturation ratios S = 1.73, 1.87, 2.03, 2.19, 2.38. Approach III was selected as the best approach for analysis because the fit accounts for all the data.

Distribution analysis	Solvent	y_{CBZ}	S	J	t_g
Approach I	EtOH	0.129	1.73	250	150
		0.129	1.87	451	255
		0.129	2.03	874	246
		0.129	2.20	900	0
		0.129	2.38	3931	72
Approach II	EtOH	0.129	1.73	500	396
		0.129	1.87	530	426
		0.129	2.03	1345	386
		0.129	2.20	1100	173
		0.129	2.38	3931	50
Approach III	EtOH	0.129	1.73	235	375
		0.129	1.87	1500	400
		0.129	2.03	1694	360
		0.129	2.20	2200	170
		0.129	2.38	3000	72

5.3.3 Parameter estimations

Figure 42 shows the estimation of parameter A and B from the three analytical approaches for EtOH, NM and DIO each. The natural log of A on the primary vertical axis shows the kinetic parameter ln A and the thermodynamic parameter B on the secondary vertical axis, both plotted against y_{CBZ}. The parameters are plotted this way to accommodate for both parameters on the same graph. The upper part of each plot shows the ln A estimations and the lower part of the plot shows the thermodynamic factors B of the solvent systems.

Using approach III to describe the parameter estimation. In DIO system, the kinetic parameter ln A indicate an increase with increase in stoichiometry for y_{CBZ} = 0.395, y_{CBZ} = 5.05 and y_{CBZ} = 0.62 at 4.59, 5.20 and 5.8 respectively. This means the kinetic factor increases with an

increase in CBZ compositions. However no similar trend was observed in *B* estimations. Suggestion that each compositions influence the estimation differently and not depend on the increase in CBZ composition in the system. In EtOH system, there is no significant change in the natural log of the kinetic parameter at different stoichiometries. The kinetic parameter is the similar so ln *A* for y_{CBZ} = 0.129 is 6.6, 6.01 for y_{CBZ} = 0.205 followed by 6.0 for y_{CBZ} = 0.298. The thermodynamic parameter *B* for y_{CBZ} = 0.129 is 0.4, 0.9 for y_{CBZ} = 0.205 and 0.4 for y_{CBZ} = 0.298. No trend was observed between solution stoichiometry and parameters *A* and *B* in ethanol.

The kinetic parameter ln *A* determined in NM system at solution stoichiometry y_{CBZ} = 0.49, y_{CBZ} = 0.75 and y_{CBZ} = 0.83 are 5.9, 5.0 and 3.58 respectively suggests that stoichiometry may have effect on the kinetic parameter. However the trends and variations in parameter estimations when compared to other distribution analysis approach indicate that ln *A* is underestimated at this stoichiometry. This could be because of sample size. The induction time sample size used here is the lowest at 23 points than any other stoichiometries therefore highlighting the effect of sample size on the accuracy of approach III analysis which does not affect approach I and II. Therefore the effect of stoichiometry on ln *A* does not follow a direct relationship. Thermodynamic parameter *B* showed no stoichiometry effect with estimation 0.7, 1 and 1 at y_{CBZ} = 0.49, y_{CBZ} = 0.75 and y_{CBZ} = 0.83 respectively. There is no proportional stoichiometry dependence y_{CBZ} on the estimation of ln *A* and *B* the data suggests that each stoichiometry influence the parameter *A* and *B* individually and it is not dependent of the increase of the CBZ as CBZ was varied to make the co-crystal in this system based on the relative solubilities of CBZ and INA.

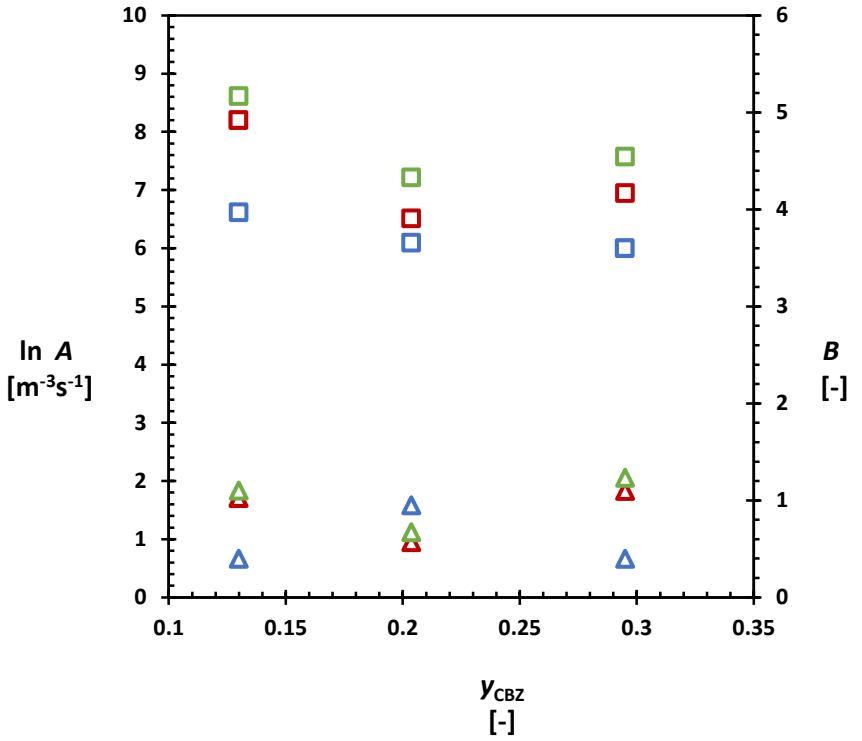
ln A
[m-3s-1]
B
[-]
yCBZ
[-]
10
9
8
7
6
5
4
3
2
1
0
6
5
4
3
2
1
0
0.1
0.15
0.2
0.25
0.3
0.35

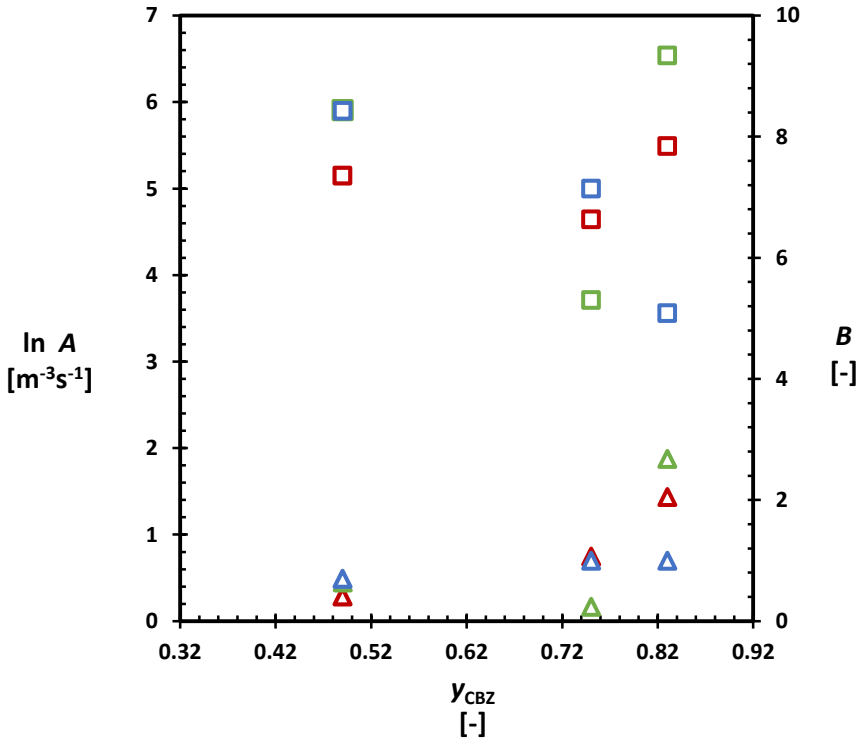
ln A
[m-3s-1]
B
[-]
yCBZ
[-]
7
6
5
4
3
2
1
0
10
8
6
4
2
0
0.32
0.42
0.52
0.62
0.72
0.82
0.92

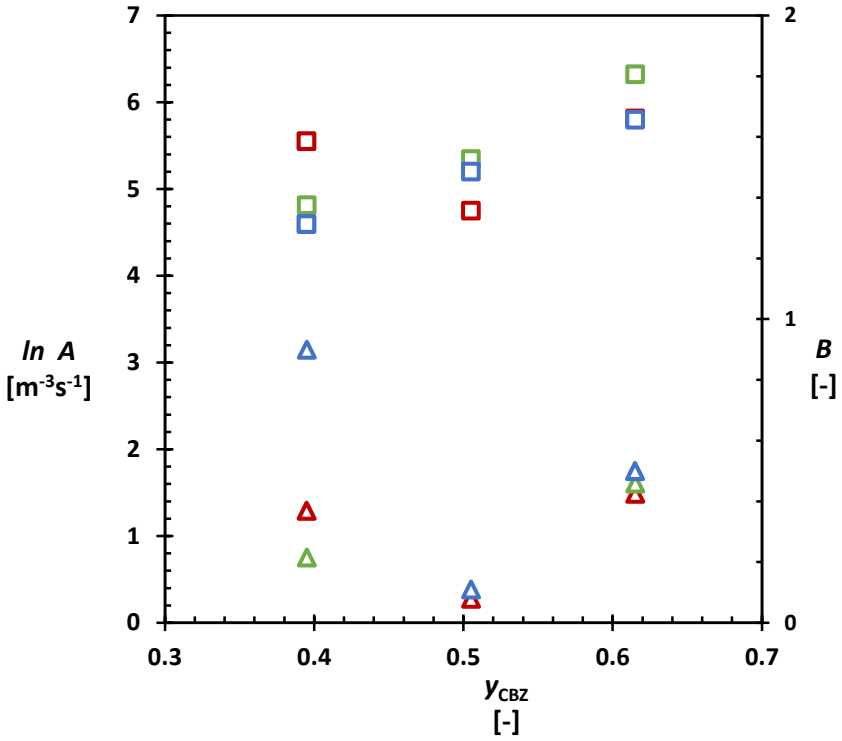

Figure 42: Parameter estimation of ln *A* (□) left vertical axis and *B* (Δ) right vertical axis from the induction time distribution measurements using the three analytical approaches for EtOH (a), NM (b) and DIO (c) with approach I (red), approach II (green) and approach III (blue). Accuracy of the parameters shows that no strong conclusion can be made on the influence of stoichiometry on ln *A* and *B* as different approaches results in different estimation of *A* and *B* and in the majority of the cases the difference in estimations is within the error range and some points overlap. The error bar is not included for clarity.

5.4 Discussion

Three probability distribution analysis approach based on the classical nucleation theory is described in this work. Approach I and II are generally used in the literature for the analysis of single component systems. Approach III was introduced as a viable approach for analysis when compared to approach I and II because it accommodate the variations in growth tg that is not dependent on changes in supersaturations and nucleation rate J that occurs at certain stoichiometries enabling individual data and not the average to be represented for parameter estimations. In addition it also ensures the sample size is large enough for a minimum sample size of 80 induction time measurements.[15][16] as it is commonly known that the uncertainty in

the induction time measurements reduces with increase in the sample size. The result suggests that approach III is more sensitive to sample size changes and may not be an ideal approach for sample size n ≤ 23.

The effect of stoichiometry on the nucleation rate *J* in ethanol at the range of supersaturation examined, suggests that stoichiometry has an effect on the nucleation rate *J* in EtOH while the stoichiometry effect on NM and DIO system is indicated but unclear. More importantly this does not translate to the kinetic parameter A estimations in EtOH and NM. However the estimated kinetic parameter A in DIO system indicates that ln A is stoichiometry dependent and it is directly proportional to the stoichiometric excess of CBZ. The kinetic factor A is described by $A = zf^*C_0$ where z is the zeldovich factor and it is expected to be steady at equilibrium and c_o is the concentration of the heterogeneous particles present in the system. Nucleation sites c_o is not known and can only be assumed, the only factor remaining is the attachment frequency (f^*). It is assumed that the building units in a solution self-associate one molecule at a time to form a critical nucleus for nucleation to occur in a single component system. In a multicomponent system, similar concept is proposed but this time with the added complexity that the interaction between the components may influence the attachment frequency. Result from DIO suggests that there is an influence attachment frequency and so the crystallisation behaviour in DIO is different from EtOH and NM as suggested by the metastable zone width.

The compositions used in this investigation is all within the confirmed co-crystal region of the phase diagram. The characterised solid form from the nucleation experiments chosen at random largely produced the stable form regardless of the solvent. For this reasons it is logical to assume that the outcome of the nucleation at all stoichiometries would produce the stable form of the co-crystal. It is suspected that the nucleation rate that is inconsistent with other data set may have resulted from an incomplete co-crystallisation process due to the *in-situ* preparation of the co-crystal where the excess co-crystal former is present at levels lower than the limit of

detection of the PXRD but conspicuous enough to be detected by the transmission of light especially when the nucleation rate of the co-crystal former is higher thereby influencing the induction time measurements. Another explanation could be that the metastable form of the co-crystal nucleates faster and quickly transforms to the stable form. To rule out these two possibilities, it may be important to design crystal nucleation studies in multicomponent systems in future *ab-inito* from both nucleation rate measurements and nucleation pathway determination standpoint. The nucleation rate measurement is self-evident from this work. The nucleation pathway determination would require monitoring the nucleation process to ensure that there is no polymorphic transformations or in complete co-crystallisation by monitoring the rate of co-crystal component consumption *in-situ*. This is a more involved proposal that may be necessary to investigate the extent of the effect of stoichiometry on nucleation rates. In summary the future study of nucleation rate of co-crystals may benefit from using non – polymorphic co-crystal. Make a bulk co-crystal for the experiment and only vary the compositions of the co-crystal former to make sure that the level of incomplete concentration is the same for all stock solution.

5.5 Conclusions

The kinetic parameter *A* derived from induction time probability distribution according to the classical nucleation theory and MZSW indicates a direct proportional dependence on solution stoichiometry in dioxane. In this system, the attachment frequency is influenced by an increase in carbamazepine composition in the solution. The kinetic parameter *A* in ethanol shows no stoichiometry dependence and this effect is inconclusive in nitromethane. The thermodynamic parameter *B* is small and relatively constant in all solvent except in nitromethane at solution stoichiometry 0.83. The small value of this parameter *B* suggests heterogeneous nucleation as the dominant mechanism in the systems. Three analytical approaches were used for the analysis of the induction time measurement which have a substantial effect on the determined values of

the kinetic and thermodynamic parameters of the classical nucleation rate equation. The approach III introduced in this work is a viable approach for distribution analysis. This involves combining all the induction time probability distribution in such a way to obtain parameter *A* and *B* directly. This approach may be more susceptible to sample size than other approaches.

5.6 References

1. Davey, R.J., Schroeder, S.L.M., ter Horst, J.H. Nucleation of Organic Crystals-A Molecular Perspective. Angew Chemie Int Ed. 2013;52(8):2166–79.

2. Vekilov, P.G. Nucleation. Cryst Growth Des. 2010;10(12):5007–19.

3. Kulkarni, S.A., Kadam, S.S., Meekes, H., Stankiewicz, A.I., Ter Horst, J.H. Crystal nucleation kinetics from induction times and metastable zone widths. Cryst Growth Des. 2013;13(6):2435–40.

4. Caridi, A., Kulkarni, S.A., Di Profio, G., Curcio, E., Ter Horst, J.H. Template-induced nucleation of isonicotinamide polymorphs. Cryst Growth Des. 2014;14(3):1135–41.

5. Jiang, S., Ter Horst, J.H. Crystal nucleation rates from probability distributions of induction times. Cryst Growth Des. 2011;11(1):256–61.

6. Brandel, C., Ter Horst, J.H. Measuring induction times and crystal nucleation rates. Faraday Discuss. 2015;44(179):199–214.

7. Ter Horst, J.H., Kashchiev, D. Determining the nucleation rate from the dimer growth probability. J Chem Phys. 2005;123(11):1–5.

8. Yu, Z.Q., Chow, P.S., Tan, R.B.H. Operating regions in cooling cocrystallization of caffeine and glutaric acid in acetonitrile. Cryst Growth Des. 2010;10(5):2383–7.

9. Gagniere, E., Mangin, D., Puel, F., Bebon, C., Klein, J.P., Monnier, O., et al. Cocrystal formation in solution: In situ solute concentration monitoring of the two components and kinetic pathways. Cryst Growth Des. 2009;9(8):3376–83.

10. Boyd, S., Back, K., Chadwick, K., Davey, R.J., Seaton, C.C. Solubility, metastable zone width measurement and crystal growth of the 1:1 benzoic acid/isonicotinamide cocrystal in solutions of variable stoichiometry. J Pharm Sci. 2010;99(9):3779–86.

11. Mullin, J.W. Crystallization. 4th ed. Boston: Butter-Worth-Heinemann; 2001.

12. Ter Horst, J.H., Cains, P.W. Co-crystal polymorphs from a solvent-mediated

transformation. Cryst Growth Des. 2008;8(7):2537–42.

13. Nordstrom, F.L., Svard, M., Rasmuson, Å.C. Primary nucleation of salicylamide: the influence of process conditions and solvent on the metastable zone width. CrystEngComm. 2013;15:7285–97.

14. Davey, R.J., Schroeder, S.L.M., Ter Horst, J.H. Nucleation of organic crystals - A molecular perspective. Angew Chemie - Int Ed. 2013;52(8):2167–79.

15. Xiao, Y., Tang, S.K., Hao, H., Davey, R.J., Vetter, T. Quantifying the Inherent Uncertainty Associated with Nucleation Rates Estimated from Induction Time Data Measured in Small Volumes. Cryst Growth Des. 2017;17:2852–63.

16. Maggioni, G.M., Mazzotti, M. Stochasticity in Primary Nucleation : Measuring and Modeling Detection Times. Cryst Growth Des. 2017;17:3625–35.

Chapter 6

Template Enhanced Induction Time Probability Distribution Measurements using Temperature Probes

Abstract

Nucleation rate determination in the presence of template can provide a wealth of information on heterogeneous nucleation. The presence of well-defined template particles at high template concentrations presents a challenge by limiting the reliability of measurements on platforms that rely on the transmission of light to obtain nucleation characteristics such as induction time distribution in solution. Here, a method is presented to determine induction time distributions in solutions in the presence of high concentrations of well-defined templates based on the detection of temperature variations upon crystallisation. This method is applied to model compounds glycine and picolinamide which shows that the template anatase and rutile are effective in enhancing nucleation in solution.

6.1 Introduction

The stochastic nature of nucleation has been used to determine the crystal nucleation kinetics of small organic compounds from induction time distribution measurement in stirred supersaturated solutions.[1] This approach relates measured series of induction times under equal conditions to a probability distribution to determine the crystal nucleation rate.[1][2][3] The rationale to use this approach to determine crystal nucleation kinetics is based on an outcome of a comparative experiment that concluded that the induction time distribution method is more accurate than metastable zone width measurements and it is also easier to analyse.[2]

Heterogeneous rather than homogeneous nucleation is thought to be the dominant nucleation mechanism in industrial crystallization processes. The addition of well-defined template particles to induce nucleation and influence crystal solid form[4] is well established. In most industrial processes template particles are not deliberately added[5] and the particles that induce nucleation in such solutions (e.g., dust particles) are ill-defined in terms of type, concentration and template performance[6] which severely complicates understanding of heterogeneous nucleation. Thus, in order to understand heterogeneous nucleation well-defined template particles should be used in nucleation measurements.

The induction time measurement method based on light transmission can be extended to allow the measurement of template induced heterogeneous nucleation rates at very low template particle concentrations (around $1 \mu g m L^{-1}$)[4] The method is limited to low template particle concentrations since the transmission of light through a solution is blocked for large template concentrations even when no crystals are present. This limitation hinders further research into the effect of templates particles on crystal nucleation.

The aim of this chapter is to develop an alternative method to light transmission measurements to determine the induction time distribution in the presence of high templates concentrations

where transmission of light becomes unreliable. It is known that if sufficient material crystallizes out of solution of a compound with a sufficiently high heat of crystallization the resulting suspension shows an increase in temperature.[7] We use this effect to detect the nucleation of crystals in the solution sample of pilcolinamide and glycine as model compounds. First the solubility of the model compounds was determined. The effect of template particle concentration on the transmission of light was investigated, then transmission based induction time distribution in the presence of template particles was determined. Finally the template particle induced induction time distributions measured through temperature changes for pilcolinamide and glycine was determined.

6.2 Method

Ethanol (Fisher 99.8%), Glycine (>99.0% Tokyo Chemical Industry, Rutile titanium oxide (99.99%), Anatase titanium oxide (99.7%) Pilcolinamide (98%) from Sigma were all used as received. Deionized water (milli-Q integral 15).

6.2.1 Solubility measurements

The solubility of glycine and picolinamide (PIL) in deionized water and ethanol (EtOH) respectively were measured using the Crystal16 equipment (Technobis). Samples of known overall compositions were heated at 0.3°Cmin^{-1} to a temperature of 55°C (80°C for glycine) at which the sample was held for 10 minutes (30 min for glycine) to make sure that all the crystals have totally dissolved while stirring at 700rpm. The clear point temperature of the sample was determined during heating stage. The clear point temperature is temperature where suspension turns into a clear solution and the transmission of light through the vial is 100%. The clear point temperature was taken as the saturation temperature T_s of the sample. The solution was then cooled to 5°C at 0.3°Cmin^{-1} in order for recrystallization to occur. Triplicate clear point temperature measurements per sample were done.

6.2.2 Induction time measurements

6.2.2.1 Solution preparation

A hundred and sixty millimetres of stock solutions of PIL in ethanol (155.2 $mgmL^{-1}$) and glycine in deionised water (355.8 $mgmL^{-1}$) were separately prepared in 250mL Fisher brand bottle to minimise concentration deviations. The prepared suspension was allowed to dissolve at a temperature of 63°C and a stirring rate of 400rpm for 60 minutes. The hot PIL solution was filtered into a preheated flask using a preheated chemically resistant syringe and filter (0.45µm) at 65°C.The flask with the solution was sealed and the solution was left on the hot plate for additional 30 minutes to make sure all solute are dissolved. The hot Glycine solution was directly used without filtration. The stock solutions of glycine were then carefully divided by volume into 20ml portions and stored at 5°C until use. The stored samples were then stirred at 63°C for 1 hour prior to use.

Stock solutions with a concentration of 4 $mgmL^{-1}$ of rutile or anatase were made in deionised water. The solution was sonicated for 15minutes using FB11211 sonicator set at 37 Hz and 55°C to allow homogenous particle dispersion. An aliquot of template suspension was then added to a known volume of deionised water. Series of dilutions were performed to obtain target template concentrations in solvent only solution. 5 ml of the target template concentration is then added to 20 ml of glycine stock solution to make a total volume of 25 ml with 284.69 mg of glycine and known template concentration in 1 ml of deionised water. The mixture of template and glycine solution was again sonicated at 37 Hz at 55°C for 15 minutes to disperse the templates in this volume. A known amount of anatase (1.09 mg ± 0.09) or rutile (1.08 mg ± 0.11) was added directly into the vials after which 1 ml of PIL stock solution was added to the templates powder. The mixture was sonicated at 37 Hz at 55°C for 15 minutes to disperse the templates.

6.2.2.2 Light transmission based induction time measurements

The induction time was measured using the Crystal16 equipment (Technobis) by exposing vials to a heat-hold-cool-hold temperature cycle while monitoring the sample light transmission with no templates and low template concentrations. The heating rate was set to 0.3°Cmin^{-1} while the hot hold temperature was respectively 40°C for the PIL samples and 55°C for the glycine samples. The solutions were held at these temperature for 10 and 30 minute respectively at this hot hold temperature for the PIL and glycine samples. The solution was then cooled with a rapid rate of 5°Cmin^{-1} to 23.5°C for the PIL samples and 22°C for the glycine samples. Once the low set temperature was reached, the PIL samples were held for 5 hours and the glycine samples were held for 3 hours at that temperature. Four induction time measurements per samples were done. This method was used for determining induction time measurement in the presence of probes and absence of probes to determine the effect of probe on the induction time measurements.

6.2.2.3 Temperature probes based induction time distribution measurement

The induction time was measured using the Crystal16 equipment (Technobis) by exposing vials to a heat-hold-cool-hold temperature cycle while monitoring the sample changes in temperature with temperature probes. The heating rate was set to 0.3°Cmin^{-1} while the hot hold temperature was respectively 40°C for the PIL samples and 55°C for the glycine samples. The solution was then cooled with a rapid rate of 5°Cmin^{-1} to 23.5°C for the PIL samples and 22°C for the glycine samples. Once the low set temperature was reached, the PIL samples were held for 5 hours and the glycine samples were held for 3 hours at that temperature. Four induction time measurements per samples were done. The probe temperatures were collected using 2 Picolog modules with 8 probes attached to each module.

6.2.2.3.1 Probe test induction time measurement

Similar temperature profile as in section 6.2.2 was used for the probe test experiment except the solution was cooled with a rapid rate of 5°Cmin^{-1} to 21, 22, 23, 24 °C for the PIL solution concentration of 157.7mgmL^{-1}.Once the low set temperature was reached, the PIL samples were held for 5 hours and the temperature profile repeated twice.

6.2.3 Analysis

The induction time measured through the probes and transmission is based on different response. However in both cases the induction time data was analysed based using this definition. The induction time is defined as the time period between the moments a constant supersaturation is created and crystals are detected. [8][9] For light transmission measurement crystals are detected when the light transmission begins to decrease from 100% for a clear solution. For probe this is when the preceding constant temperature increased momentarily. The setup allows induction time measurement using probes and transmission at the same time as shown in Figure 43.

Figure 43. The induction time measurement vial containing a suspension and a magnetic stirrer bar, equipped with the temperature probe and transmission based setup.

6.3 Results

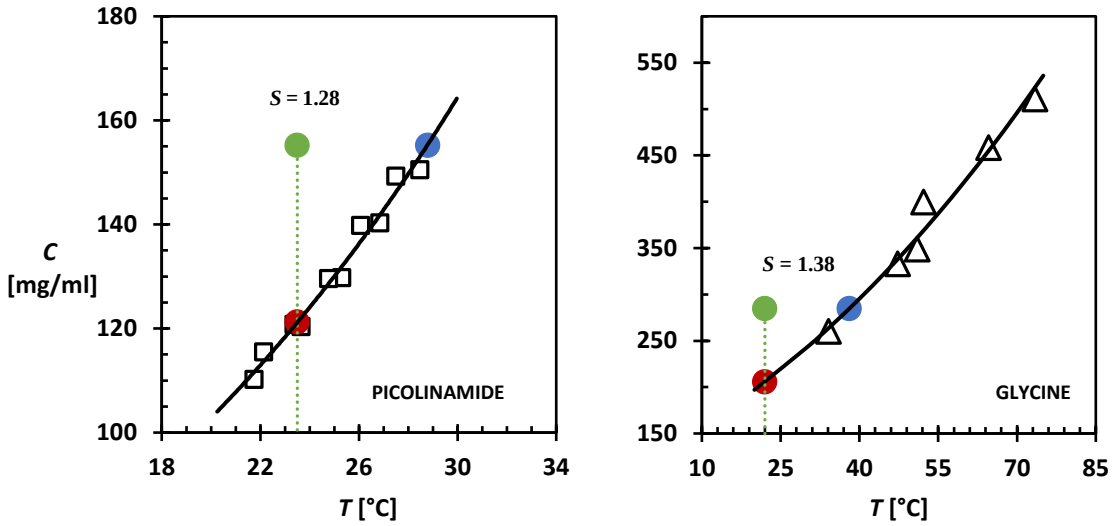

Figure 44. The temperature dependent solubility of PIL (□) and glycine (Δ) in EtOH and deionized water respectively. Each point on the graph represents the average saturation temperature measurements for each sample. The error bars are smaller than the symbol used to represent the points. The best fit line is a fit of Van't Hoff equation to the experimental data. The saturation temperature of the stock solution used in these experiments is signified by blue point and the red point is the saturation temperature induction time was measured. The green point is the condition induction time was measured to determine the nucleation rate S = 1.28 and 1.38 for PIL and glycine respectively

The systems PIL in ethanol and glycine in deionized water are used in this study. Figure 2 shows the temperature dependent solubility of these systems. At 25°C the solubility of PIL in EtOH and glycine in deionized water are 130 $mgmL^{-1}$ and 219 $mgmL^{-1}$ respectively. There is no reported solubility for PIL in EtOH in the literature for comparison. However, the solubility of glycine in this work is in agreement with the work of Xia Yang et al.[10] Each experimental solubility point is an average measurement. The model compounds both have a substantial solubility and a good temperature dependence. High supersaturations can therefore be created using a decrease in temperature of a saturated solution which is likely to coincide with a temperature increase upon crystallization. The blue point signifies the chosen saturation concentration and saturation temperature of the stock solution. The induction times are chosen

to be measured at 23.5 and 22 °C for PIL and glycine respectively. The red points indicate the solubilities of 121.3 and 205.8 $mgmL^{-1}$ at these temperatures for PIL and glycine, respectively. The measurement condition for the induction time can be represented as a supersaturation ratio S = 1.28 and 1.38 for PIL in EtOH and glycine in water, respectively.

6.3.1 Temperature probe test for induction time measurements

Detecting a temperature change that accompany a crystallising solution during induction time measurement at different conditions can simply be done if the supersaturation or amount of crystallising material is high enough. Figure 45 shows the temperature change and the maximum amount of material that can form (C - C*). This is estimated by the concentration difference (C-C*) between the equilibrium concentration of PIL and the target concentration when cooled. The change in temperature ΔT is the difference in temperature between the maximum temperature after crystallization and the average temperature just before crystallization. This temperature measured by the probes is on average lower when the solution is cooled to 24 °C than when it was cooled to 21 °C. The set cooling temperature (21, 22, 23 and 24°C) is a function of supersaturation. This suggests that the temperature response may not be detected at very low supersaturations S or when the solution is cooled to temperature close to the saturation temperature of the solution. It can be estimated that when $C = C^*$, $\Delta T = 0$. A detectable temperature change can be used for induction time measurement provided the supersaturation of the solution is within detectable temperature range. Suggesting that a good volume of crystallization material may be required to obtain a noticeable temperature change.

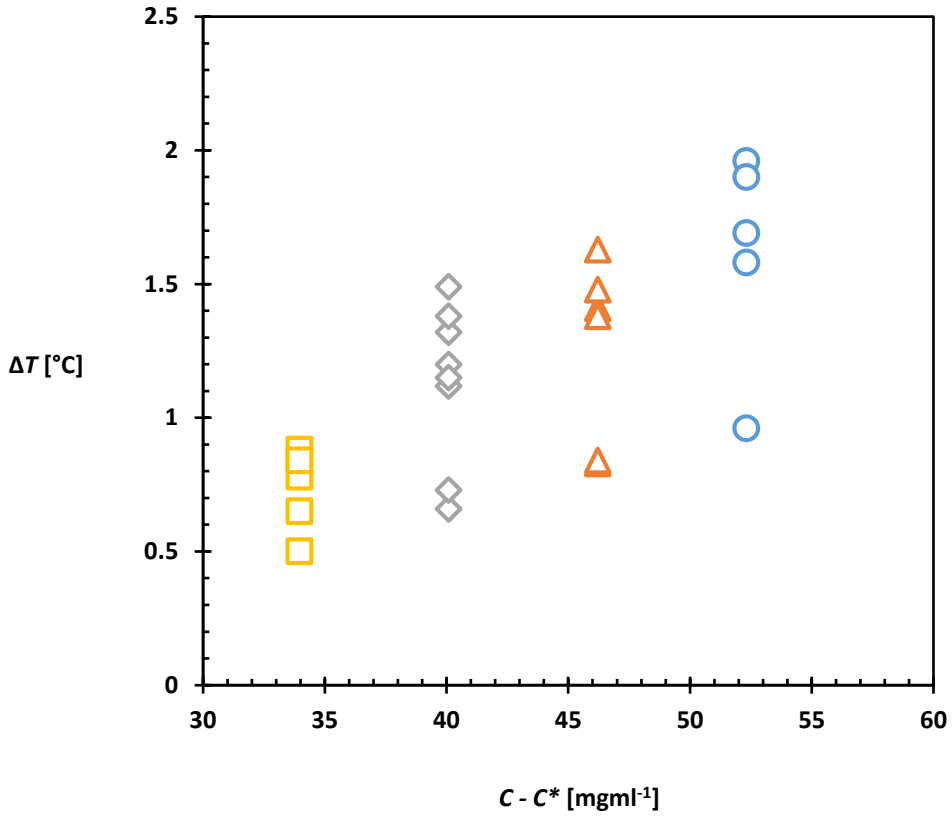

Figure 45. The difference in temperature between the maximum temperature after crystallization and the average temperature just before crystallization is plotted against the amount *C-C** that can maximally form. Saturated solution of PIL (157.7mg/ml) without template (anatase) cooled to 21°C (blue ○), 22°C (orange Δ), 23°C (grey ◊) and 24°C (yellow □)

6.3.2 Comparing light transmission based induction time measurement with probe based induction time measurements

The presence of templates in solution can affect the reliability of transmission based measurements so there is a need to select template concentration C_T carefully. It was established that concentration below 3mgL^{-1} does not significantly obstruct the transmission of light through the sample.[4] It was determined in this work that the concentration of anatase below 0.29 mgmL^{-1} does not interfere with the transmission of light. This was assumed for rutile concentration as well. It is noted that since the particle size of the template used is < 25 nm and

therefore small, other types of particles with different density and size range will have a different behaviour. Based on this rutile concentration C_T 0.02mgmL^{-1} was selected to compare induction time measurements in transmission based and probe based measurements for the induction time of glycine in deionized water. The light transmission is thought to decrease only when crystals have nucleated and grown to an appreciable size and the volume fraction of crystals is large enough to block the light. At the same time as the light transmission measurement, also the temperature in the solution is tracked through the temperature probe.

Figure 46 shows changes in the induction time indicators – light transmission and temperature changes signal over a period of time. The vertical axis ΔT is the temperature difference between temperature probes and arbitrary temperature. This arbitrary temperature was determined from average of constant temperature for a range of time period. The secondary axis represent the percentage transmission of light (τ) through the samples. The transmission of light changes from 100% for an initially clear solution to below 100%. The time at which this occurs for a crystallising solution is (t_{99}). By definition the induction time for transmission based measurements is $t_x = t_{99} - t_0$. The peak formed from temperature change detected by the probe can be divided into three areas. The first is the onset time t_{start}, at which the temperature just begins to change from constant temperature. The time of maximum temperature t_{max} is the time when the temperature reaches it maximum at 14657s and the last is t_{end}, which is the time point when temperature dissipates back to constant temperature and it is estimated to occur at 15200s. These temperature changes event from t_{start} to t_{end} took approximately 11 minutes. These typical takes 5 - 16 minutes. More in some cases. Once T_{max} is reached, the temperature dissipates relatively slowly with time resulting in an asymmetric peak. However in a few cases, the measured temperature only very slowly returns to the constant temperature after crystallization occurred. It was decided that the time t_{max} at which maximum temperature is reached is easy to

determine and may capture the induction time well. The induction time using the temperature probe therefore is $t_x = t_{max} - t_0$.

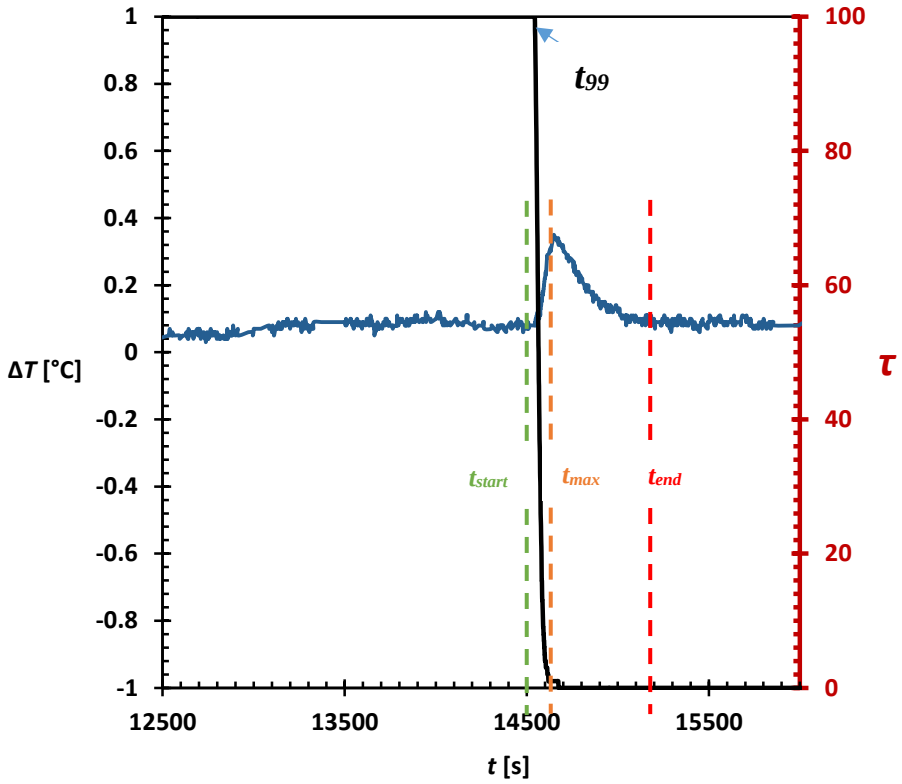

Figure 46. Light transmission and temperature of the same vial sample in an induction time measurement at constant temperature for a supersaturated glycine solution using 0.02 mgmL^{-1} rutile template in water. The light transmission axis τ shows the changes in transmission from 100% in clear solution to zero. Changes in light transmission in a supersaturated solution is represented by a black line. The time t_{99} at which the first crystals are detected is taken as the time when light transmission just dropped from 100%. The temperature difference ΔT (blue line) indicates the temperature difference between temperature probe and an arbitrary temperature. Onset t_{start}, maximum t_{max}, and end time t_{end} of the temperature jump are indicated. The decrease in light transmission coincides with the increase in temperature indicating that both probes and transmission can be used to determine induction time.

Now that the induction time for probe and the light transmission can be analysed. The two induction time for the same samples can be compared. Figure 47 shows the plot of induction time for light transmission and probes. The correlation between measurements indicate that the induction time measurement is comparable and can both be used simultaneously to obtain induction time distribution in the same vial at high enough supersaturations.

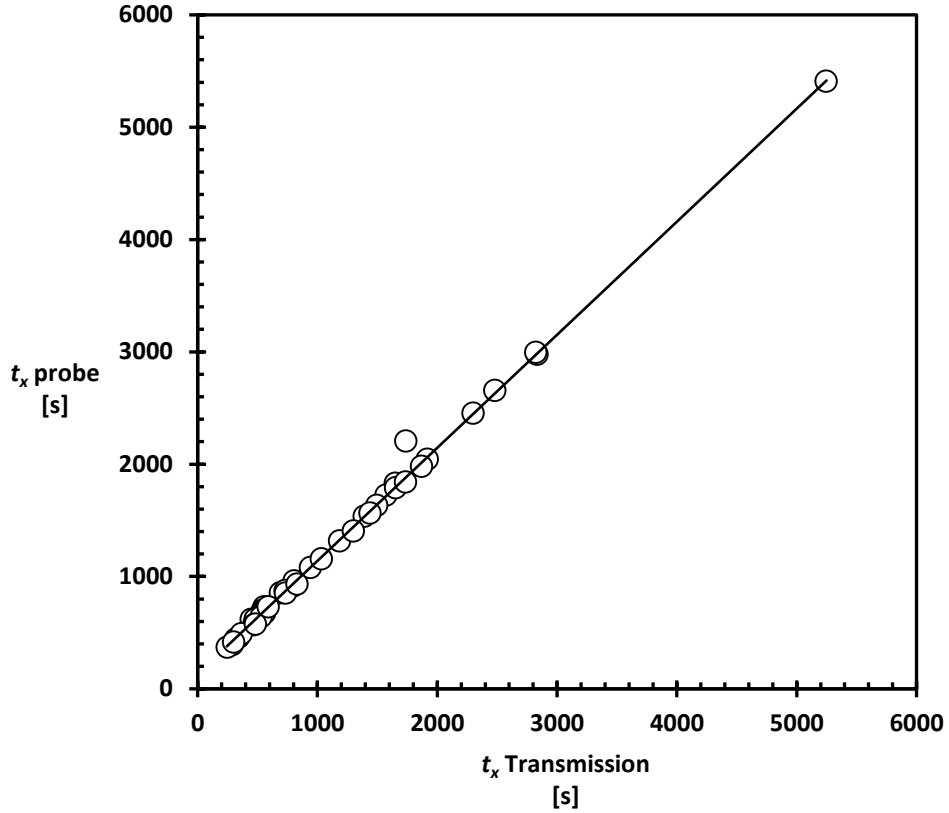

Figure 47 Induction time of temperature probes and transmission in the same set of measurements. The intercept on the t_i probe axis shows the delay before T_{max} is reached. Transmission-based and temperature-based induction time distributions give comparable results. The outlier indicates that the duration for attaining t_{max} may vary in some samples.

6.3.3 Template particle induced induction time distributions measured through temperature changes

The induction time measured from temperature changes using probe for both glycine and PIL was analysed. The induction time distribution measurements harness the stochastic nature of nucleation to determine nucleation rate J and growth time t_g which can be determined by fitting equation 40 to the cumulative probability distribution calculated using equation 41 in both glycine and pilcolinamide systems.

$$P(t) = 1 - \exp(-JV(t - t_g)). \quad 40$$

Where V is the volume of the crystallizing material. P(t) is the probability that a vial would nucleate over a period M_t out of the total number of sample vials used in the experiment M.

$$P(t) = \frac{M_t}{M} \quad 41$$

Figure 48 shows the direct fitting of the induction time probability distribution of glycine in deionized water and PIL in EtOH at various conditions. The induction time probability distribution for glycine and PIL was determined at S = 1.38 and S = 1.28 respectively to estimate the nucleation rates J and growth rate t_g at different template concentrations C_T. Figure 48c shows the fitted induction time probability distribution at 1.09mgmL^{-1} anatase, 1.08mgmL^{-1} rutile and without templates. It took 500s for 50% of PIL in EtOH to nucleate in the presence of anatase, 6300s in the presence of rutile and 9765s for the same percentage of vials to nucleate without templates. This indicates the effectiveness of anatase as a nucleating agent over rutile for PIL. Only one template concentration was investigated in PIL because the templates were directly weighed into the vail rather than suspended in the solution. It can be observed that the direct fitting on equation 40 does not account for all the measured induction time when compared to measurement without templates and measurements in glycine. This could be because the error in weighing is indicated in the induction time measurements. It also suggests that solution method of templates transfer may be ideal method of handling templates for induction time measurements.

Figure 48a and Figure 48b shows three investigated templates concentration of anatase and rutile for glycine at S = 1.38. The direct fitting aligns well to capture the induction time probability distributions. The use of templates decreased induction time in glycine for both anatase and rutile when compared with no templates. Induction time decreases in both anatase and rutile as the template concentration C_T increases. For example a 1000s passed before 50% of the sample nucleate at C_T 0.8mgmL^{-1}. When compared to 1600s for 0.0295mgmL^{-1} and 6000s without templates. Similar trend was observed when rutile was used.

The determined nucleation rate J and t_g from the curve fitting using equation 40 is summarized in Table 13. The nucleation rate of glycine in the presence of 0.0059mgmL^{-1} anatase is 521s^{-1}m^{-3} ± 14. This increased to 890 s^{-1}m^{-3} ± 56 in the presence of 0.8 mgmL^{-1} anatase. For the same concentration of rutile the nucleation rate was lower than anatase at 732 s^{-1}m^{-3} ± 75 indicating that anatase is more effective at increasing the nucleation rate than rutile. The nucleation rate of glycine in the presence of 0.0059mgmL^{-1} rutile is 328 s^{-1}m^{-3} which increased to 746 ± 38 when rutile concentration increased to 0.0290 mgmL^{-1}.However the nucleation rate of 0.0295mgmL^{-1} seems to be higher than 0.8mgmL^{-1} but within the error margin of the nucleation rate estimation. It was also observed that the nucleation rate does not increase by the same factor as the concentration of templates increases. In general, templates particles increases nucleation rate. Anatase seems to be more effective in increasing the nucleation rates in filtered and unfiltered systems. The use of probes may have effect on the nucleation rates. For example the effect of probes in glycine system is within error while that of the PIL is larger than the error difference.

The growth time t_g in glycine decreases as the concentration of templates increases. The growth time decrease from 388s ± 33 for 0.0059mgmL^{-1} of rutile to 79s ± 59 for 0.8mgmL^{-1} of rutile. A similar trend was observed for other template where growth time t_g decrease for 0.0059mgmL^{-1} anatase from 291 ± 25 to 217 ± 33 for 0.8mgmL^{-1}. Despite the general

effectiveness of anatase in increasing the nucleation rate than rutile, the growth time of glycine at the highest template concentration 0.8 mgmL^{-1} is lower in rutile than anatase but t_g is similar for anatase and rutile at C_T = 0.02 mgmL^{-1}.

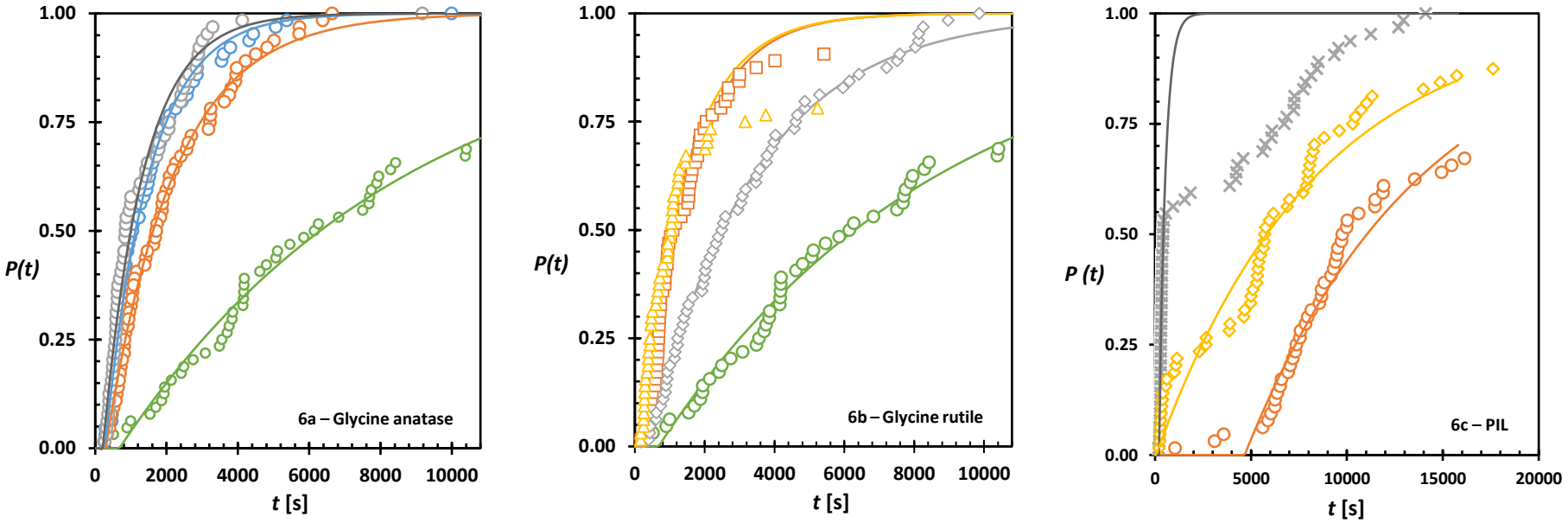

Figure 48. Probability distribution *P*(t) of induction times for glycine in deionized water at *S* = 1.38 for 6a anatase and 6b rutile and 6c PIL in ETOH at *S* = 1.28 6a. No template (green circles). 0.00592mg/ml (blue circle) 0.0295mg/ml (orange circle), 0.8mg.ml (grey circle). 6b. 0.0059mg/ml rutile (grey ◊), 0.029mg/ml rutile (orange □), 0.8mg/ml (yellow Δ). 6C no templates (orange ○), 1.08mg/ml rutile (Yellow ◊) 1.09mg/ml anatase (grey x)

Table 13. Template assisted nucleation rate J and growth time t_g of PIL in EtOH and glycine in water at S = 1.28 and 1.38 respectively. [-] signifies no templates was used in the experiments.

Compound	Template type	Template concentration [mg/ml]	J [$s^{-1}m^{-3}$]	t_g [s]
Picolinamide	without probes	[-]	700 ± 5	35.6 ± 22
Picolinamide	with probes	[-]	109 ± 3	46.68 ± 10
Picolinamide	Anatase	1.09 ± 0.09	906 ± 212	0.00±
Picolinamide	Rutile	1.08 ± 0.10	114 ± 8	0.00±
Glycine	with Probes	[-]	123 ± 6	677 ± 162
Glycine	without probes	[-]	138 ± 6	288 ± 131
Glycine	Rutile	0.0059	328 ± 7	388 ± 33
Glycine	Rutile	0.0290	746 ± 38	270± 32
Glycine	Rutile	0.8000	732 ± 75	79 ± 59
Glycine	Anatase	0.0059	521 ± 14	291 ± 25
Glycine	Anatase	0.0290	807 ± 32	271 ± 23
Glycine	Anatase	0.8000	890 ± 56	217 ± 33

6.4 Discussion

Harnessing the exothermic nature of crystallization by direct measurement of temperature change in a crystallising solution has added one other property that can be monitored in a system in addition to transmission of light for induction time measurements. This alternative method can be complimentary to light transmission based method. It is identified that supersaturation and the volume of crystallised material are the two main prerequisite to use this methods. Since this method is based on the exothermic nature of crystallisation, it is envisaged that the sensitivity of the probe and attenuated effect of the probe on the induction time measurements are other factors to consider.

The attenuated effect of the temperature probe on the induction time measurement is observed in this work. It is imagined that this may not be so in other systems so a preliminary work might be required to test the effect of the probe on the induction time measurements. However it would be best if the temperature changes can be monitored in a non-invasive way.

The aim of this work is to develop an alternative method for induction time measurements. We develop a tool to gain insights into the nucleation kinetics using the model compounds PIL and Glycine. A deliberate addition of well-defined templates into a crystallising supersaturated solution is expected to reduce the nucleation barrier to favour heterogeneous nucleation [10]. This is confirmed by an increase in nucleation rate with increase in templates concentration a trend that would not be expected to occur for homogenous nucleation. The effectiveness of anatase over rutile as a nucleating agent can be attributed to different interfacial energy and nucleating sites C_0 of the templates particles according to the classical nucleation theory, crystal nucleation from solution can be described as

$$J_{HEN} = zf^{*}C_{o}\exp\left(-\frac{16\pi v^{2}c\gamma^{3}}{3k^{2}T^{2}ln^{2}S}\right) \qquad 42$$

Where z is the zeldovich factor, f^* is the attachment frequency of the building unit of the nucleus, C_o of the nucleation sites due to heterogeneous particles, γ is the interfacial energy between crystalline phase and solution, the shape factor c, and the molecular volume v in the crystalline phase. In the case of template-induced heterogeneous nucleation, the effective interfacial energy reduces the nucleation work by so doing increases the nucleation rate.

It is proposed that this method might be ideal for slow nucleating compounds. Especially where the presence of the probes has a significant effect on the nucleation rate. It was observed in this work and other work[2] that a 2 minute equilibration time is required when the solution is cooled to a constant temperature during a fast cooling profile. Early nucleation within this region complicates the defined supersaturation of the system. In addition, there is potential for this method for investigating polymorph transitions based on the heat of solution since the heat of solution studies relied on measuring temperature changes in solution when a solid is dissolved in a known volume of solvent as demonstrated by Souillac et al[11] using Cimetidine.

6.5 Conclusion

An alternative method for induction time measurement in solution with high template concentrations is developed thereby minimising the limitations on the study of heterogeneous nucleation through induction time measurements. This method is based on monitoring temperature change in the solution detected by probes. Supersaturation and the volume of the crystallising crystals are the main influential factors to measure a detectable temperature change in the solution. Using a cooling crystallisation pathway, the temperature dependent solubility of PIL and Glycine in ethanol and deionized water respectively makes it ideal model to control supersaturation by controlling temperature. Template particles reduces induction time and increase the nucleation rate. Anatase and rutile are both efficient in increasing the nucleation rate. Anatase is more efficient than Rutile.

The measurement of induction time using temperature probes has been successfully demonstrated and would lead to further opportunities to investigate heterogeneous nucleation in multicomponent systems. Use of functionalised particles and different particle sizes and

types to gain a better understanding of heterogeneous nucleation and insight into molecular behaviour by using functionalised particles.

6.6 References

1. Jiang, S., Ter Horst, J.H. Crystal nucleation rates from probability distributions of induction times. Cryst Growth Des. 2011;11(1):256–61.
2. Kulkarni, S.A., Kadam, S.S., Meekes, H., Stankiewicz, A.I., Ter Horst, J.H. Crystal nucleation kinetics from induction times and metastable zone widths. Cryst Growth Des. 2013;13(6):2435–40.
3. Brandel, C., Ter Horst, J.H. Measuring induction times and crystal nucleation rates. Faraday Discuss. 2015;44(179):199–214.
4. Caridi, A., Kulkarni, S.A., Di Profio, G., Curcio, E., Ter Horst, J.H. Template-induced nucleation of isonicotinamide polymorphs. Cryst Growth Des. 2014;14(3):1135–41.
5. Davey, R.J., Schroeder, S.L.M., ter Horst, J.H. Nucleation of Organic Crystals-A Molecular Perspective. Angew Chemie Int Ed. 2013;52(8):2166–79.
6. Urbanus, J., Laven, J., Roelands, C.P.M., Horst, J.H.T., Verdoes, D., Jansens, P.J. Template induced crystallization: A relation between template properties and template performance. Cryst Growth Des. 2009;9(6):2762–9.
7. Lakatos, B.G., Szilágyi, B. Modeling Crystallization from Solution with Heat Effects. Cryst Growth Des. 2015;15(12):5726–37.
8. Davey, R., Garside, J. From molecules to crystallizers. In: From molecules to crystallizers. 2000. p. 1–52.
9. Mullin, J.W. Crystallization. 4th ed. Boston: Butter-Worth-Heinemann; 2001.
10. Yang, X., Wang, X., Ching, C.B. Solubility of Form r and Form γ of Glycine in Aqueous Solutions. J chem Eng Data. 2008;(53):1133–7.

11. Souillac, P.O., Dave, P., Rytting, J.H. The use of solution calorimetry with micellar solvent systems for the detection of polymorphism. Int J Pharm. 2002;231(2):185–96.

Chapter 7

Conclusion

The drive towards gaining insights into nucleation as a key step in a crystallisation process requires a new approach and development of tools that are applicable to resolve challenges in both pharmaceutical industry and in academia. This thesis addresses key challenges in multi-component systems and reports experimental tools applicable in phase equilibria, co-crystal screening and induction time measurements.

In chapter 3, a systematic approach for co-crystal phase diagram construction is presented as a workflow. This workflow is the result of the study of the phase diagram of the CBZ-INA co-crystal in three solvents. It requires a limited number of clear point measurements of pure components and co-crystal that lead to a predicted phase diagram. The phase diagram constructed in this way assumes that the presence of one component does not influence the solubility of the other one and it ignores stoichiometric effects on the co-crystal solubility. These assumptions were investigated through further screening of the co-crystal phase diagram which shows that stoichiometric effects can influence the co-crystal region and solubility product. This leads to the construction of a more accurate co-crystal phase diagram that considered the stoichiometric effect but still assumes that the solubility of the pure component is not affected by the presence of the other. Finally, it is shown that the solubility of one component is affected by the presence of the other. In all solvent systems, solubility also affects the symmetry (or the skewed-ness) of the co-crystal region. This workflow provides a fast and efficient method to co-crystal phase diagram construction that is applicable in the design of co-crystallization processes as well as in nucleation studies (such as in chapter 5).

In chapter 4, two mostly used co-crystal screening methods, LAG (liquid-assisted grinding) and solution co-crystallization, were compared. In this work, LAG method resulted in 2 hits with methyl gallate and Acesulfame K and 3 hits for solution co-crystal screening after co-former selection through *In-silico* screening. The solution co-crystal screening method is based on solubility determination, this ties in well with the phase diagram workflow demonstrated in

chapter 3. In this way, co-crystal screening can be integrated with phase diagram construction. The new co-crystal materials obtained from the screening were not used for the phase diagram construction. However, a preformed and characterised co-crystal was used instead but this requires a change in approach from phase diagram construction to co-crystallisation process design. The combination of all LAG and solution co-crystal screening method increase the chances of forming a co-crystal that said, further work is needed to ascertain or validate the use of *in-silico* screening for increasing the chances of forming a co-crystal in addition to ordering the co-formers.

The determination of the co-crystallisation kinetics for a polymorphic multicomponent crystal introduces another level of complexity that is not generally encountered in single component systems In Chapter 5, the co-crystallisation kinetics study of a CBZ-INA co-crystal material shows that the nucleation rate is not strongly influenced by the solution stoichiometry in ethanol and nitromethane. However, there is an indication that kinetic parameter *A* from Classical Nucleation Theory in dioxane (DIO) may have a stoichiometry dependence. A similar observation is made for the MSZW in DIO which decreases with an increase in stoichiometric excess of CBZ suggesting that crystallization is less inhibited at higher stoichiometry excess of CBZ. Three analytical approaches applied to the same data lead to different estimations of the kinetic and thermodynamic parameters for CBZ-INA co-crystals and sample size is a great contributor.

In Chapter 6 a new method is proposed based on the temperature change upon crystallization for the measurement of induction time distributions. Light transmission-based and temperature-based induction time distributions are shown to be comparable, also in the presence of templates up to around 0.29 $mgmL^{-1}$. Beyond such a template concentration only the temperature-based induction time can be determined. Thus, induction time measurement through thermal response can be used for measuring nucleation in the presence of template particles. The temperature

change detected is limited by the probes sensitivity and the crystallizing amount. The measurement of induction time using temperature probes has been successfully demonstrated and will lead to further opportunities to investigate heterogeneous nucleation in multicomponent systems.

This thesis has successfully set out solutions to some important challenges that was hitherto a limitation to gaining insight into nucleation in co-crystals as tools. These tools can then be used to study nucleation behaviour in other multicomponent systems to further probe the fundamentals of nucleation. One area could be understanding nucleation in a less complex co-crystals that is non-polymorphic co-crystal and ultimately continuous nucleation for better product attributes. This would set the platform for the eventual manufacturing of co-crystals as a pharmaceutical product.

7.1 Recommendations

(i) The tools demonstrated in this work set the stage for further investigations into nucleation in multicomponent systems; particularly heterogeneous nucleation in multicomponent systems. It is proposed that the workflow (Chapter 3 and 4) can be used to understand the thermodynamics of a selected system and a systematic nucleation studies (chapter 5) can follow using the methods demonstrated in chapter 6 with or without using functionalised templates. Solution association studies can be combined with template-assisted nucleation so that there is better control and information over all parameters of heterogeneous nucleation.

(ii) Another area of interest could be to develop and design templates that are separable from formed crystals. or develop ways of separating templates from the formed crystals to make this process applicable in pharmaceutical manufacturing especially when the use of templates lead to desirable polymorphs

(iii) The study of solution stoichiometry, stoichiometric excess or compositional effect on nucleation allows for more degrees of freedom for continuous co-crystallization and continuous co-crystallization configuration. It is recommended that the stoichiometric effect is first studied in less complex systems when possible that is systems that are non- polymorphic to isolate stoichiometric effect. The objective should be to monitor the series of events that occurred before the induction time is determined using process analytical tools e.g. rate of co-crystal component consumption before nucleation, solution transformation in terms of self-association in solution rather than a focus of the solid form outcome from the measurements alone

(iv) Also the work in chapter 4 on co-crystal indicates the benefit of understanding the phase diagram: choosing the proper stoichiometry during co-crystallization allows for increase yield and productivity.

7.2 Acknowledgments

I would like to thank my first supervisor Prof Joop Ter Horst for his consistent guidance, attention to details and critical appraisals demonstrated throughout this project which made all other students in my cohort envious. I will also like to thank my second supervisor Prof Jan Sefcik for his comments and probing questions during our meetings. I would like to thank the Doctoral Training Centre in continuous Manufacturing and Crystallisation for the training at the beginning of PhD and the EPSRC Centre for Innovation Manufacturing in Continuous Manufacturing and Crystallisation for financing this project. Special thanks to Helen Wheatcroft for her invitation to work on AstraZeneca drug compound, Anna Jawor-Baczynska and Jim McCabe. Thanks for your support, discussion and advice to produce chapter 5 of this thesis. A very warm thank you to my brother Olakunle Olalere without whom I would not have come to Scotland from England. Thank you for your support and making the move less stressful.

Appendix A

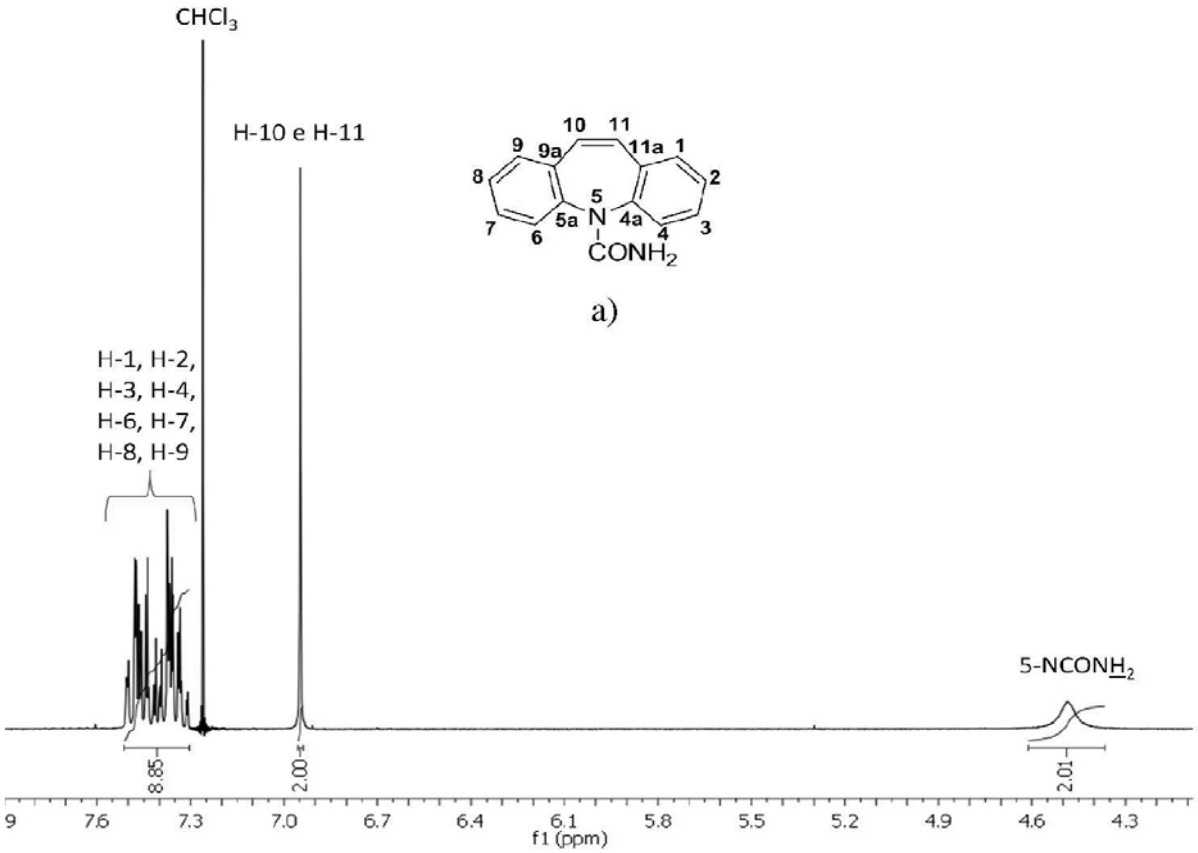

Figure **1.** ^{1}H NMR of carbamazepine used for comparison. Adapted from Neves. C et al biomimetic oxidation of carbamazepine with hydrogen peroxide catalyzed manganese porphyrinnmr 2012, Vol. 35, No. 7, 1477-1481.

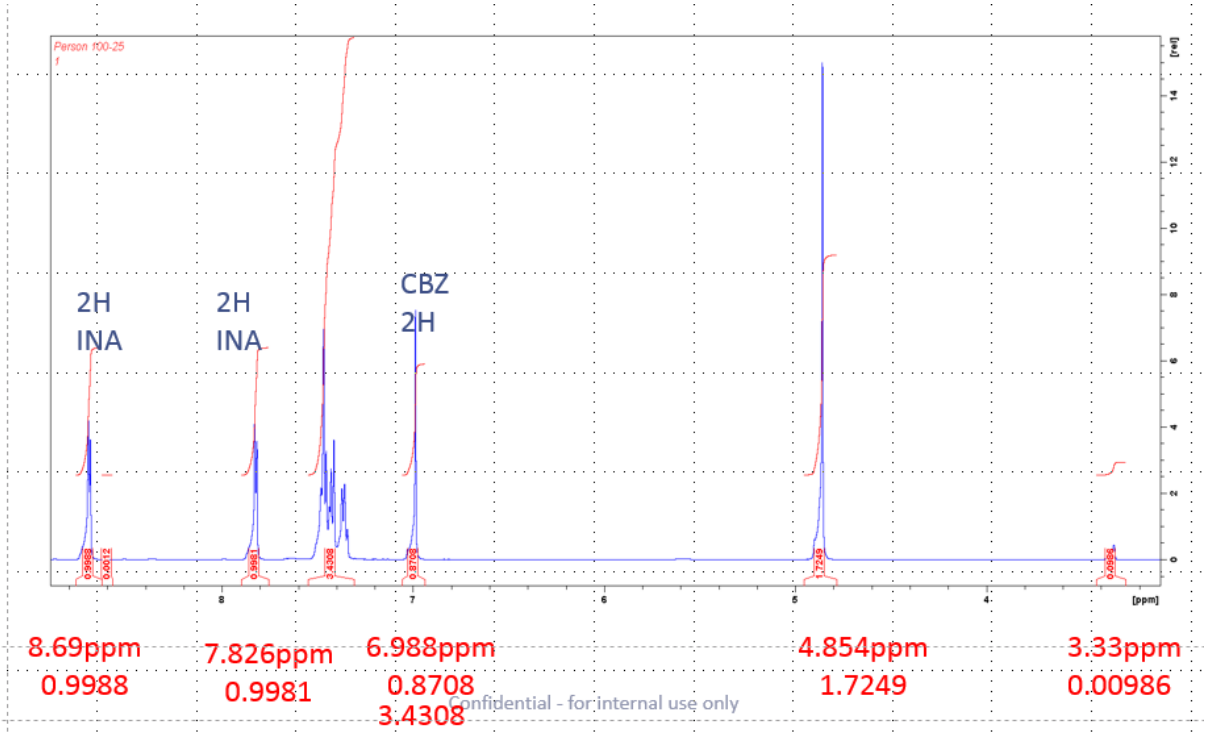

Figure 2. [1]H NMR spectrum integration of CBZ and INA mixture used for calibration. 1.5mg CBZ to 1mg INA mass ratio

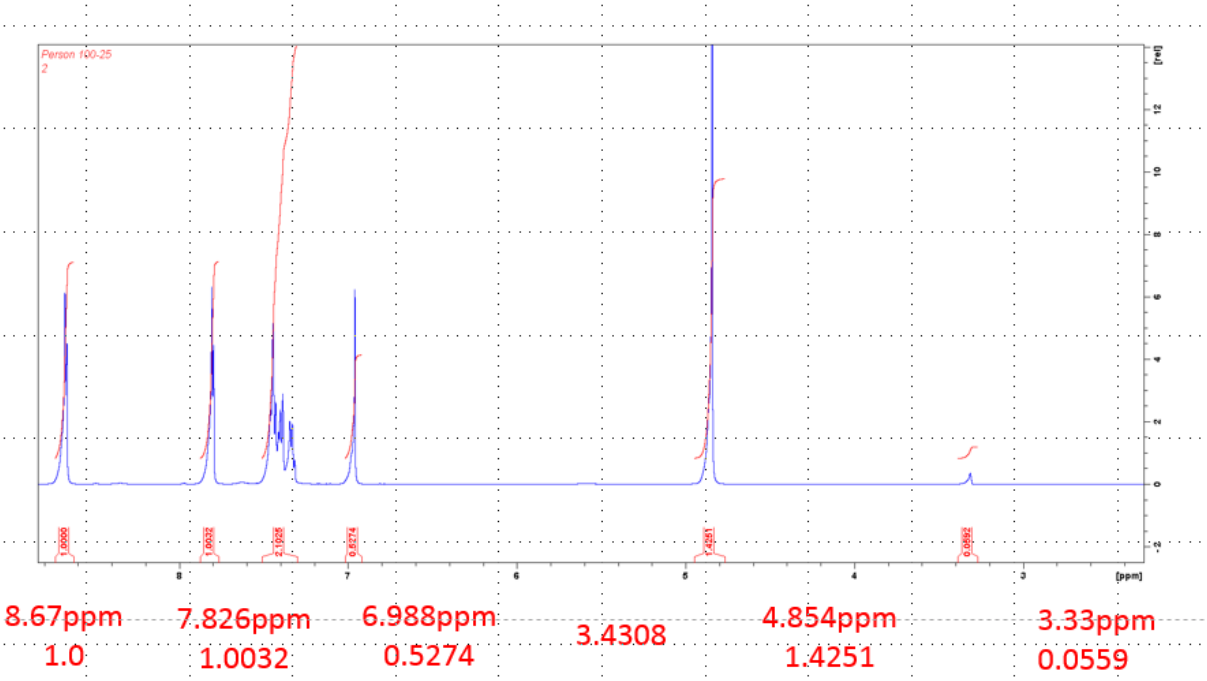

Figure 3. [1]H NMR spectrum integration of CBZ and INA mixture used for calibration.

1mg CBZ and mg of 1mg INA mass ratio

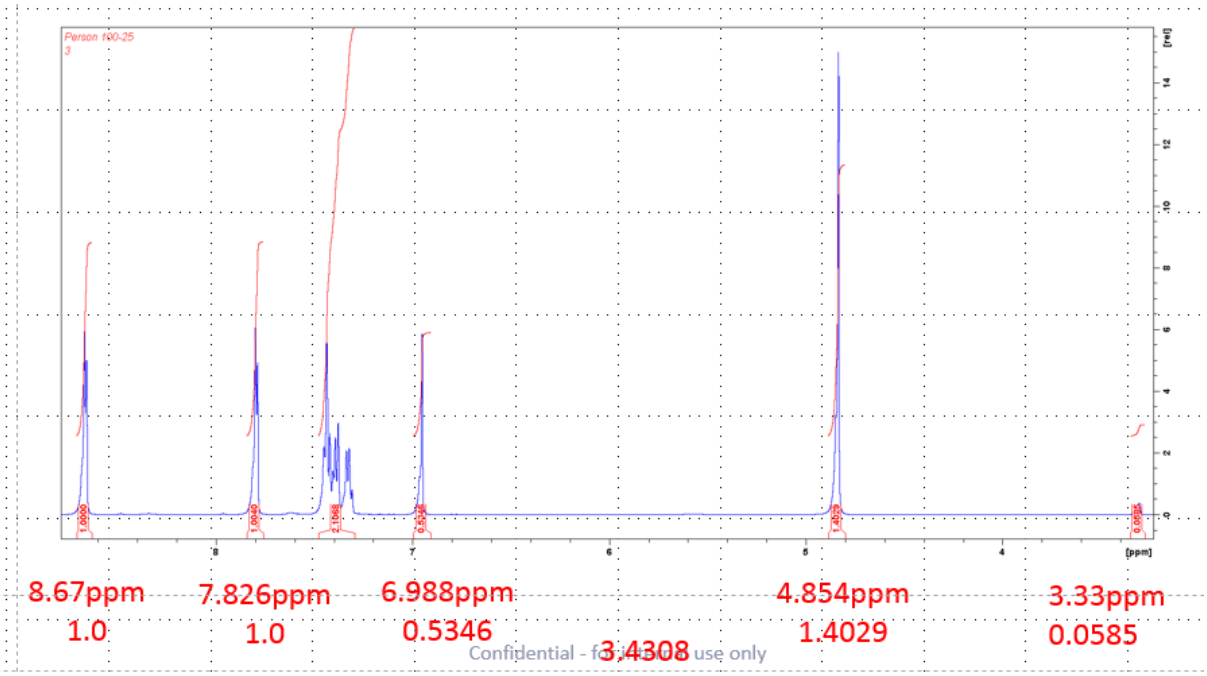

Figure 4. ^{1}H NMR spectrum integration of CBZ and INA mixture used for calibration.1mg CBZ and mg of 1mg INA mass ratio

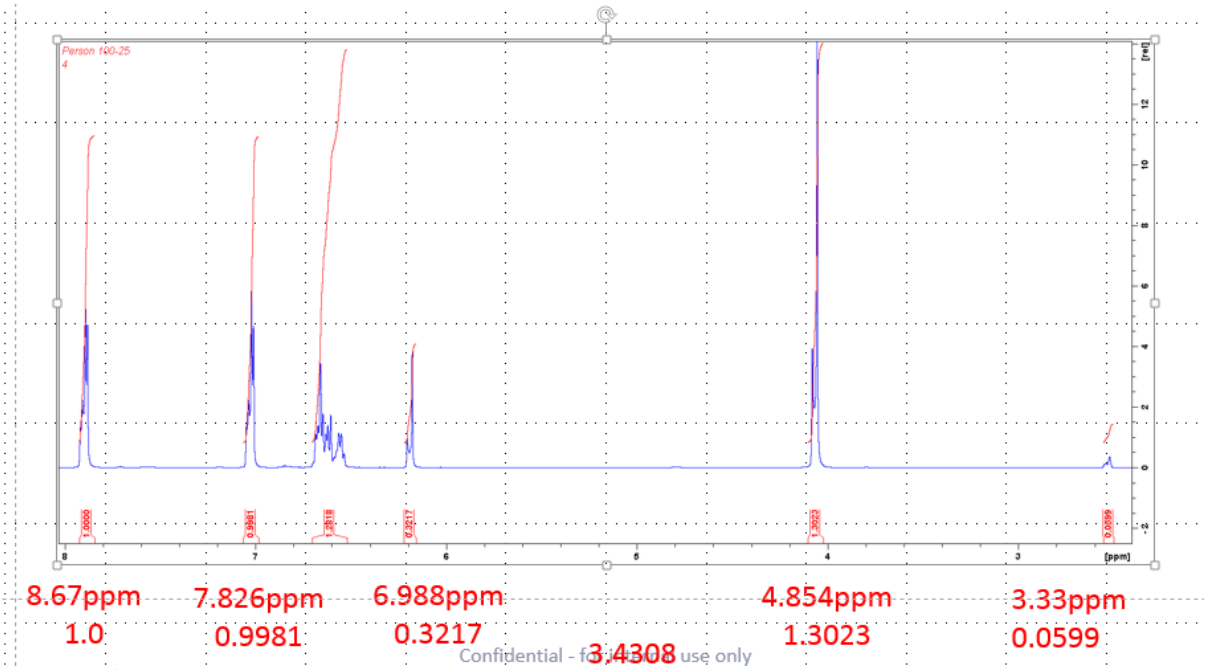

Figure 5. ^{1}H NMR spectrum integration of CBZ and INA mixture used for calibration.1mg CBZ and mg of 1.5mg INA mass ratio

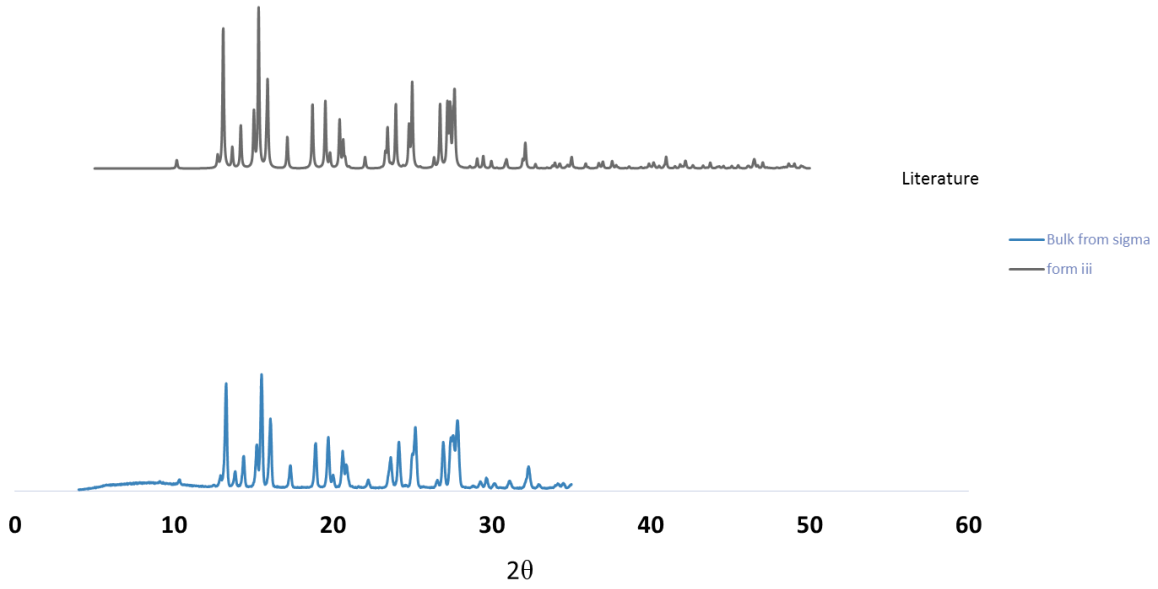

Figure 6. Powder pattern of CBZ form III from experimental (blue) compared with literature (black)

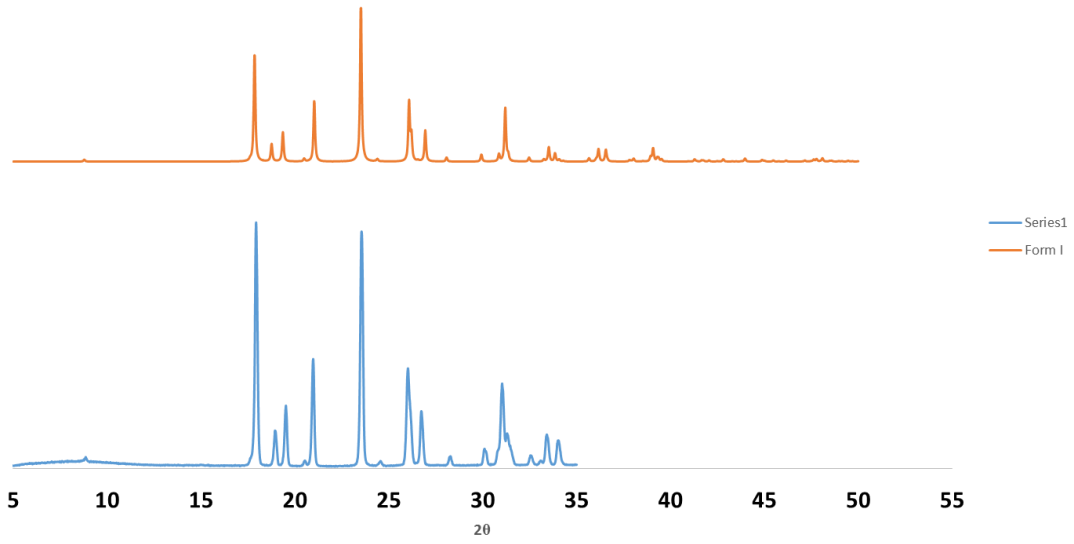

Figure 7. Powder pattern of INA form I (blue) from experimental compared with literature (orange)

Appendix B

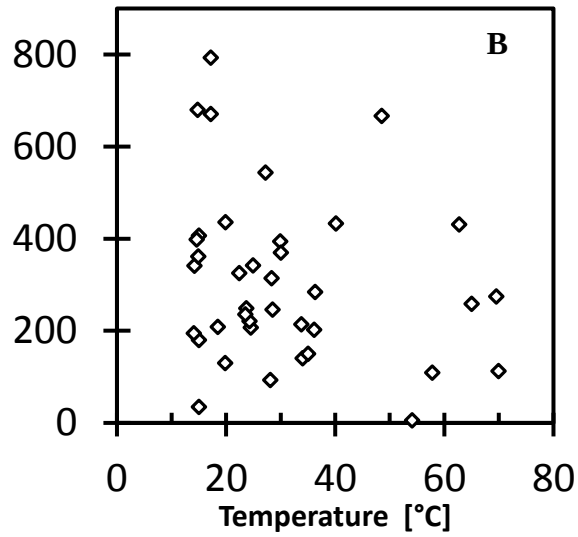

Figure 8. The complete pure component solubility of the co-formers. One point solubility measurements of the co-former in 70:30 IPA and water.

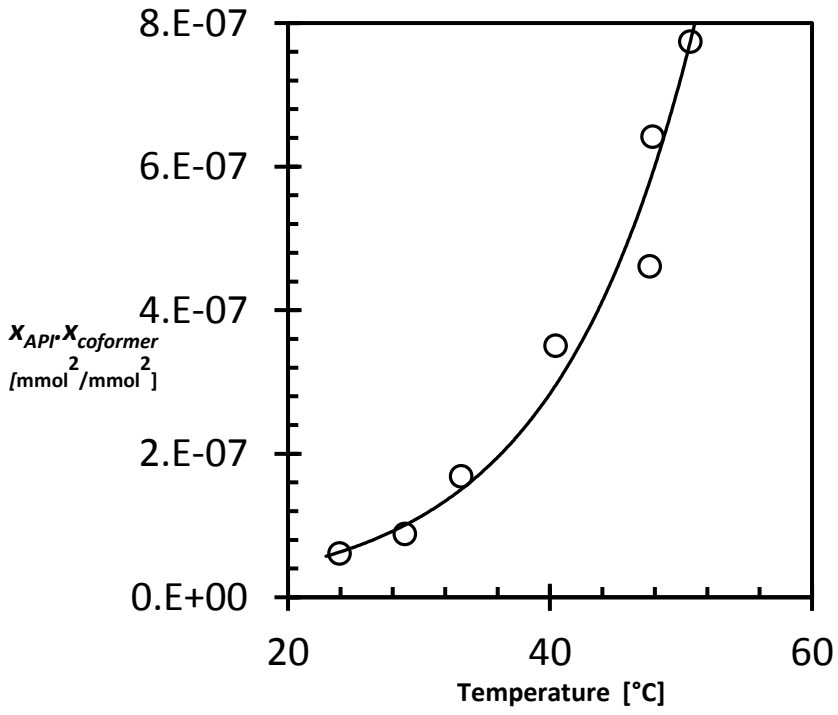

Figure 9. The solubility product of the co-crystal compound A

Appendix C

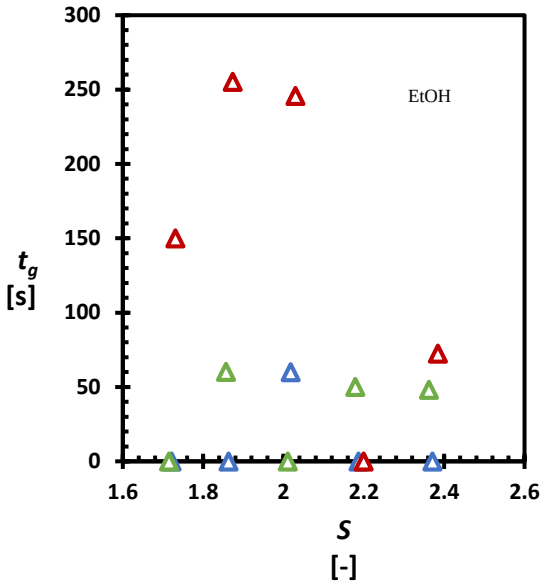

Figure 10

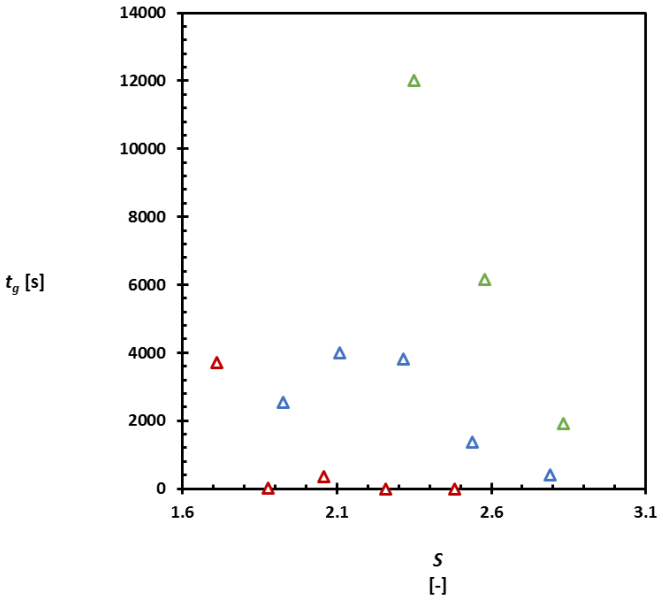

Figure 11. The growth rate t_g is not supersaturation dependent as the t_g in most cases for the best fit is zero for NM system approach I

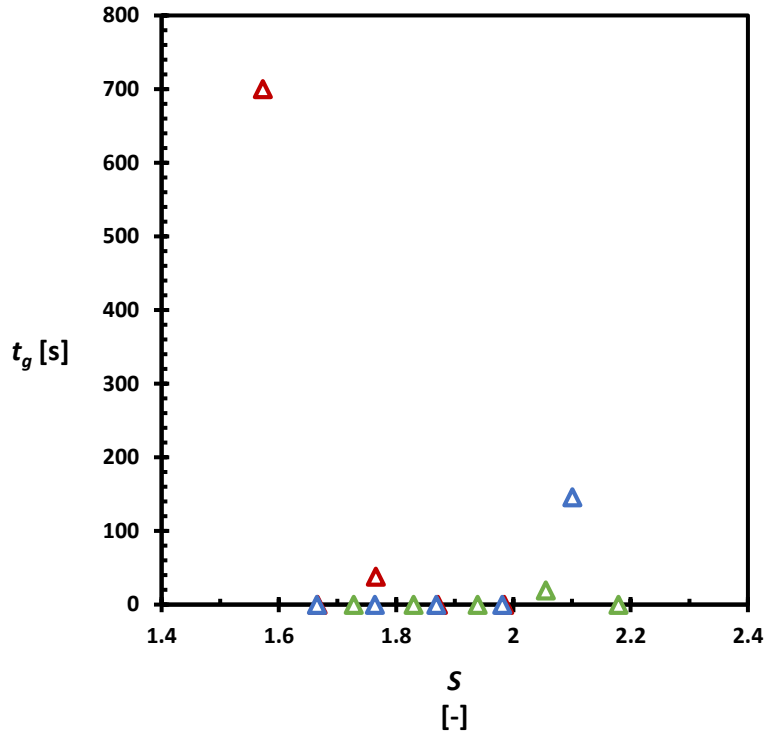

Figure 12. The growth rate t_g is not supersaturation dependent as the t_g in most cases for the best fit is zero for DIO system approach I

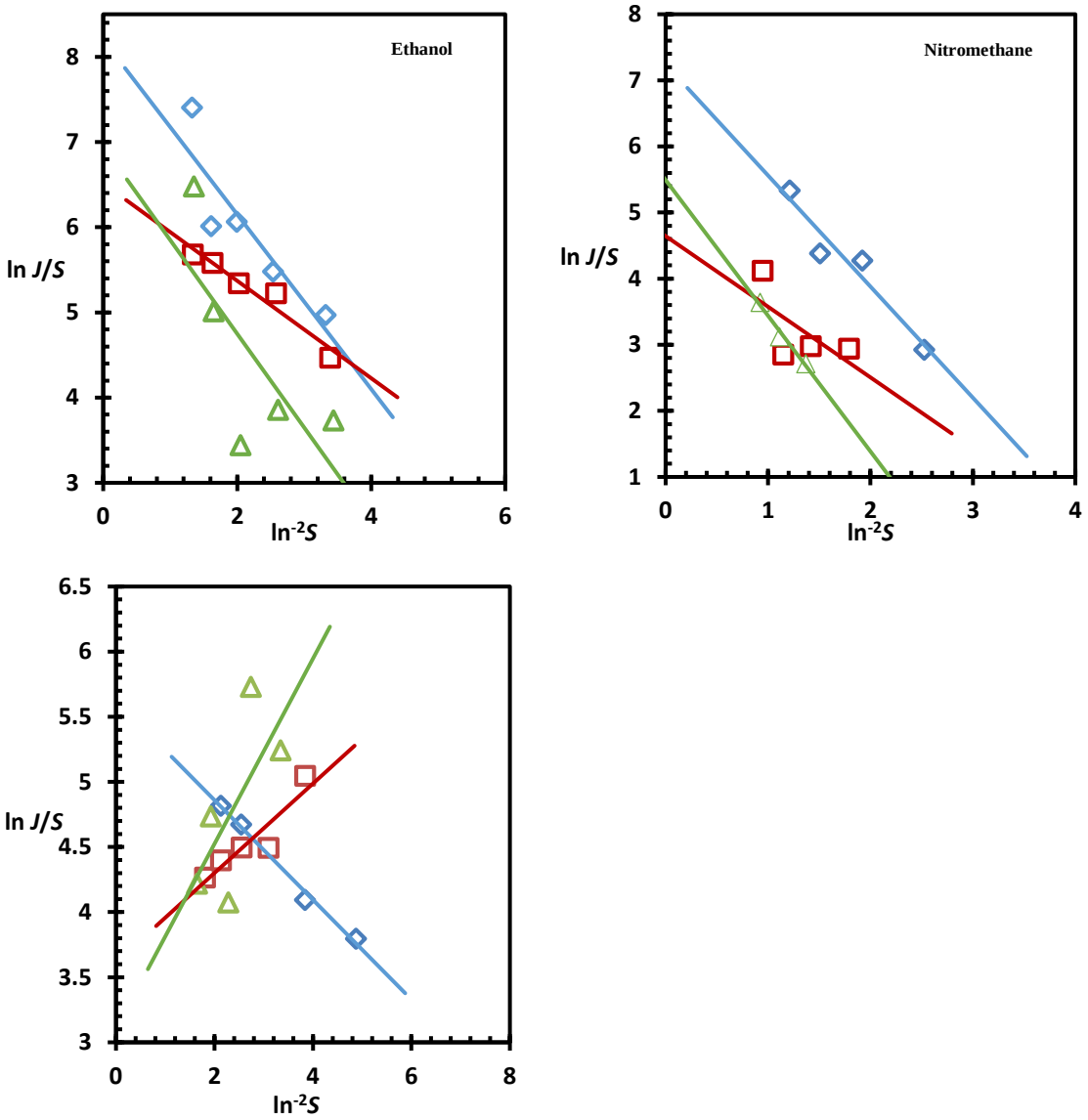

Figure 49. ln (J/S) against $ln^{-2}S$ for the induction time measurements in EtOH, NM and DIO which enables the determination of the nucleation parameters A and B from equation 5. EtOH (y_{CBZ} 0.129(blue ◊) , 0.204 (red □) , and 0.2948(green Δ)), NM (y_{CBZ} 0.498(blue ◊), 0.752 (red □), and 0.833(green Δ)) and DIO y_{CBZ} 0.393 (blue ◊) , 0.505 (red □) , and 0.615 (green Δ) . Determined parameter are shown in table 1.

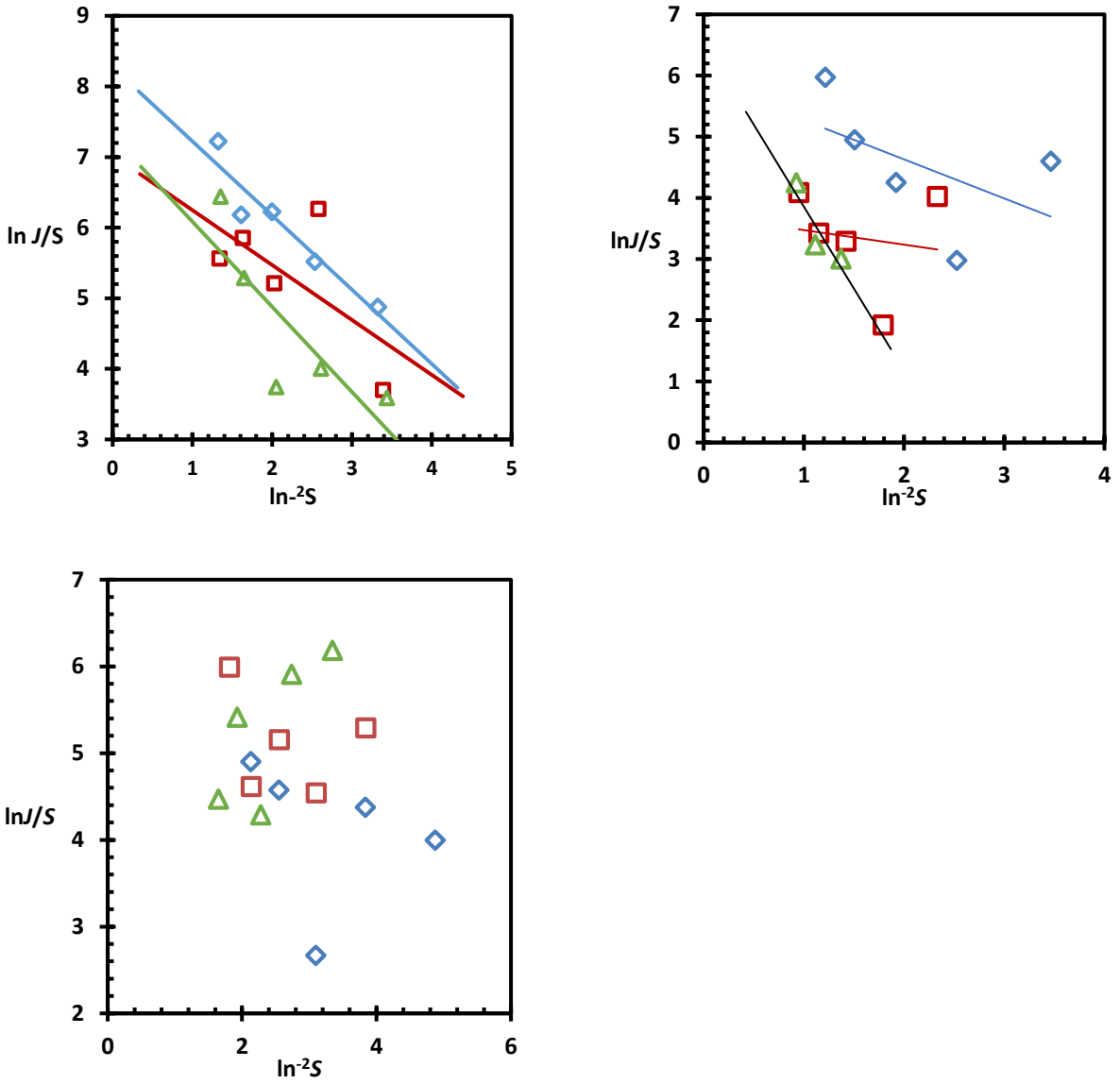

Figure 50. ln (J/S) against ln-^{2}S for the induction time measurements in EtOH, NM and DIO which enables the determination of the nucleation parameters A and B from equation 5. EtOH (y_{CBZ} 0.129(blue ◊), 0.204 (red □), and 0.2948 (green Δ), NM (y_{CBZ} 0.498(blue ◊), 0.752 (red □), and 0.833(green Δ)) and DIO y_{CBZ} 0.393 (blue ◊), 0.505 (red □), and 0.615 (green Δ). This is the data set with all the data present.

Approach III

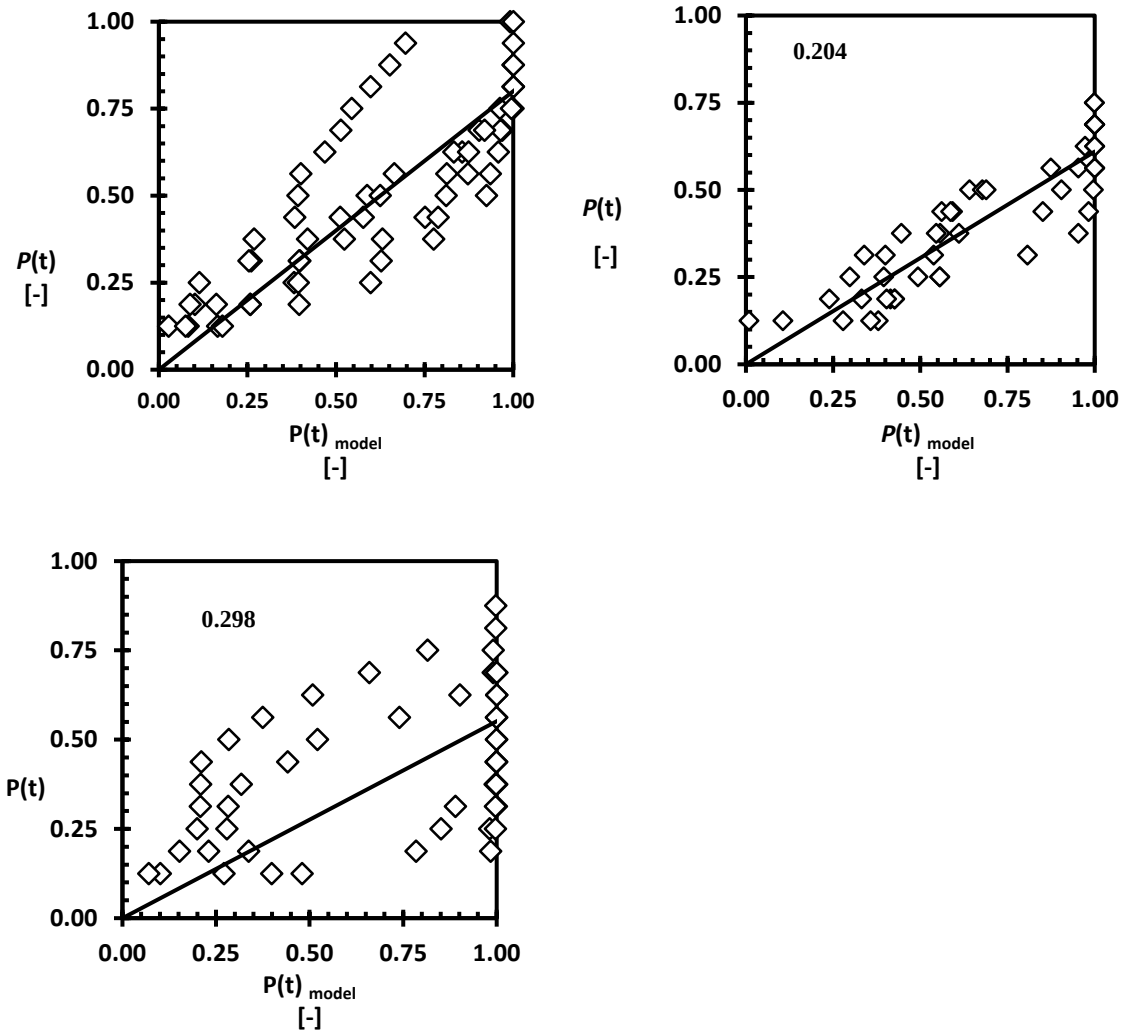

Figure 51. Plot of $P(t)$ expt vs $P(t)_{model}$ at solution stoichiometry y_{CBZ} 0.129, 0.204 and 0.298 in EtOH to determine parameter *A* and *B*.

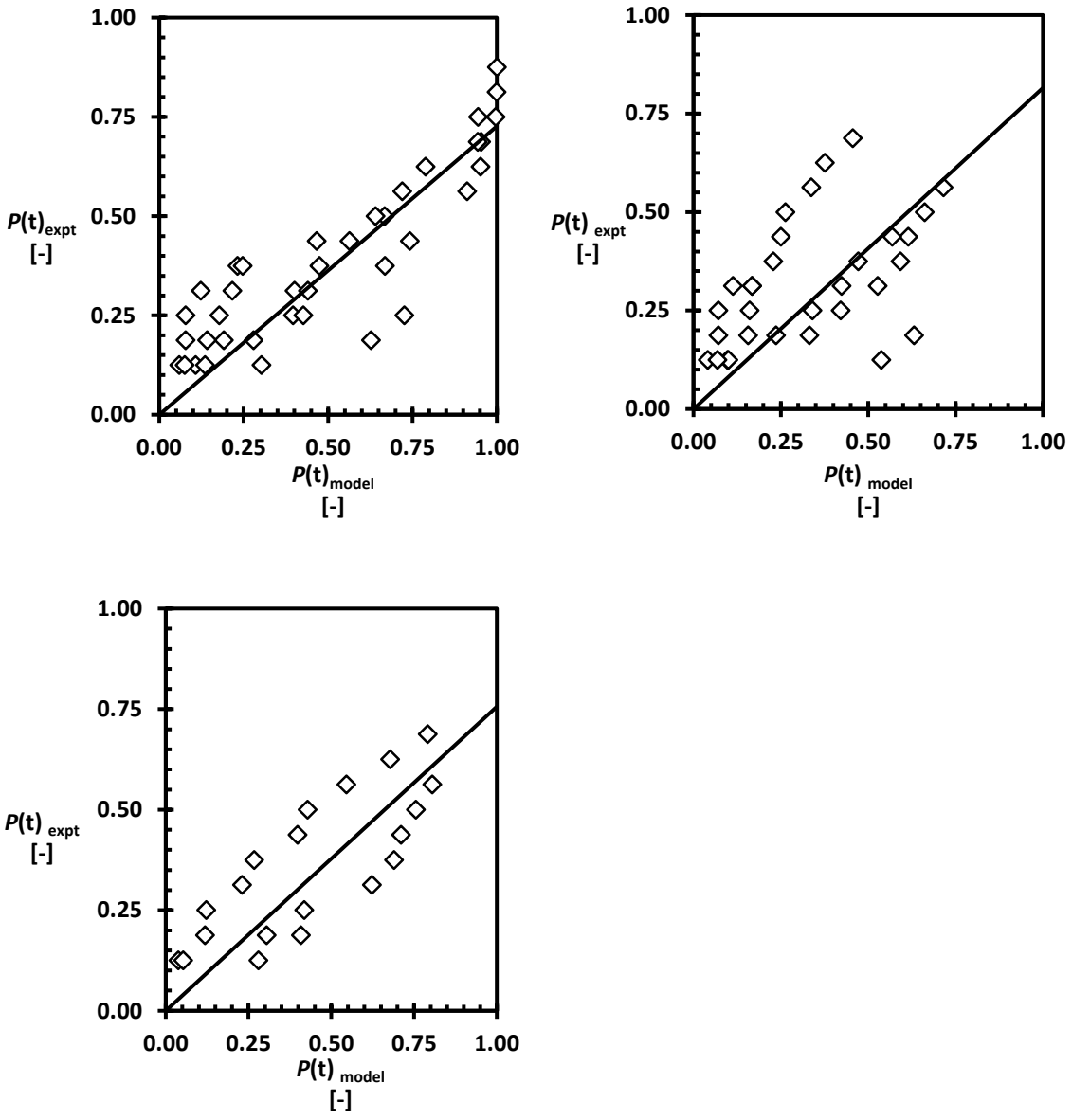

Figure 52. Plot of $P(t)$ expt vs $P(t)_{model}$ at solution stoichiometry y_{CBZ} 0.498, 0.752 and 0.833 in NM to determine parameter *A* and *B*.

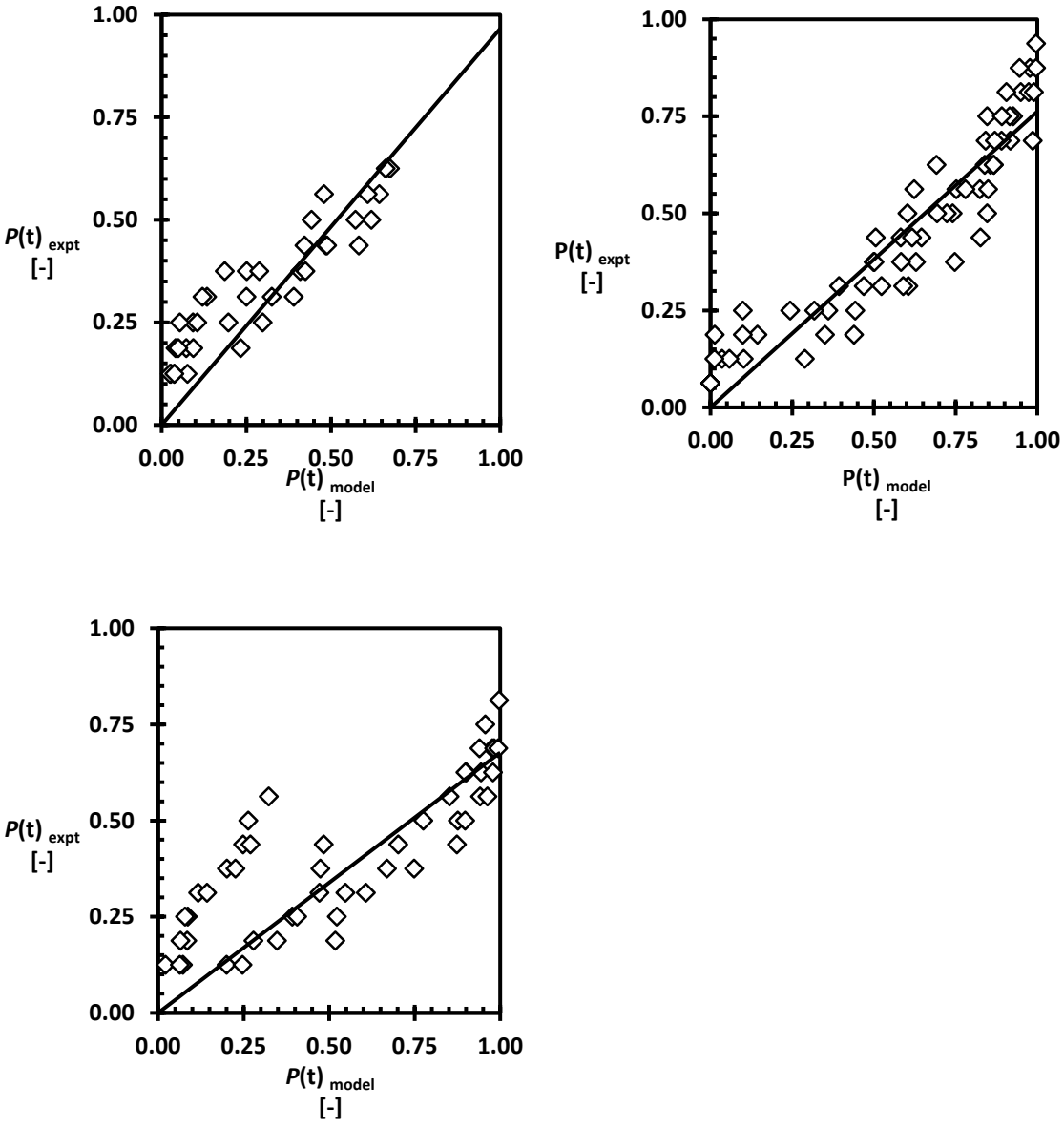

Figure 53. Plot of *P*t $_{expt}$ vs *P*t $_{model}$ at solution stoichiometry y_{CBZ} 0.393, 0.505 and 0.615 in dioxane to determine parameter *A* and *B*.